

For Reference

NOT TO BE TAKEN FROM THIS ROOM

For Reference

NOT TO BE TAKEN FROM THIS ROOM

Ex LIBRIS
UNIVERSITATIS
ALBERTAENSIS





Digitized by the Internet Archive
in 2019 with funding from
University of Alberta Libraries

<https://archive.org/details/Olsen1964>







Thesis
1964
#17D

THE UNIVERSITY OF ALBERTA

THE ALPHA-PARTICLE BREAKUP

OF THE

12.71 AND THE 11.83 MEV LEVELS IN C^{12}

by

William Charles Olsen

A THESIS

SUBMITTED TO THE FACULTY OF GRADUATE STUDIES

IN PARTIAL FULFILMENT OF THE REQUIREMENTS FOR THE DEGREE

OF DOCTOR OF PHILOSOPHY

DEPARTMENT OF PHYSICS

EDMONTON, ALBERTA

~~DECEMBER, 1963~~
1964

2:00 PM
1964
4-17-64

THE UNIVERSITY OF ALBERTA

THE ALPHA-PARTICLE BREAKUP

OF THE

^{12}C AND THE 11.83 MEV LEVELS IN ^{12}C

by

William Charles Olsen

A THESIS

SUBMITTED TO THE FACULTY OF GRADUATE STUDIES

IN PARTIAL FULFILLMENT OF THE REQUIREMENTS FOR THE DEGREE

OF DOCTOR OF PHILOSOPHY

DEPARTMENT OF PHYSICS

EDMONTON, ALBERTA

1964
1964

UNIVERSITY OF ALBERTA

FACULTY OF GRADUATE STUDIES

The undersigned certify that they have read, and recommend to the Faculty of Graduate Studies for acceptance, a thesis entitled THE ALPHA-PARTICLE BREAKUP OF THE 12.71 AND THE 11.83 MEV LEVELS IN C^{12} , submitted by William Charles Olsen in partial fulfilment of the requirements for the degree of Doctor of Philosophy.

ABSTRACT

The alpha-particle decay of states in C^{12} , with special emphasis on those at 11.83 and 12.71 MeV excitation, has been studied using the $B^{11}(d,n)C^{12}$ reaction. Neutron time-of-flight spectra and solid state detector charged-particle spectra were analyzed by a two-parameter pulse height analyzer. Angular distributions and spectrum shapes of the alpha particles from the 12.71 and 11.83 MeV states indicate that these states decay sequentially through Be^8 . The 1^+ spin-parity assignment for the 12.71 MeV state is supported by the fact that no transitions to the ground state of Be^8 were observed. Approximately 90 percent of the transitions from the 11.83 MeV state proceed via $Be^8(2.9)$ while the remaining 10 percent feed the ground state. There is some evidence to indicate that the 10.84 MeV state of C^{12} decays exclusively to $Be^8(0)$. The 3^- assignment for the 9.64 MeV state in C^{12} is favored over 1^- on the basis of the angular distribution of the alpha particles from this state to the Be^8 ground state. The spectrum shape for this group confirms this well established transition.

This work, together with other work reported in the literature, justifies the representation of C^{12} as a $Be^8-\alpha$ two-body cluster from the alpha particle threshold to 16 MeV excitation. Such a representation is in accordance with

(Abstract continued)

the Two-Body Cluster Model of Phillips and Tombrello.

Appendix II describes a frequency-modulated proton magnetic resonance system for the measurement and control of magnetic fields from 1 to 12 kilogauss. This system was designed for use with the combined broad range spectrograph and spectrometer facility of the University of Alberta Nuclear Research Center.

ACKNOWLEDGMENTS

I should like to express my gratitude to Doctors W.K. Dawson, G.C. Neilson, and J.T. Sample for suggesting this project, for many discussions pertaining thereto, and for much encouragement during the course of the research.

Special thanks are also due to T.K. Alexander for many valuable discussions pertaining to both the research and the electronics described herein.

I should also like to thank Messrs. E. Cairns, J.B. Elliott, C. Green and L. Holm, the technical staff of the University of Alberta Nuclear Research Center, for much help during the course of this work.

I am very grateful to my wife not only for typing this thesis but also for her encouragement during the past three years.

Finally, I thank the National Research Council for financial support in the form of three studentships awarded to me during the course of this work.

TABLE OF CONTENTS

CHAPTER I.	INTRODUCTION	1
I.	Motivation	1
II.	Survey of the Literature on the Disintegration of C^{12}	4
CHAPTER II.	EXPERIMENTAL APPARATUS	14
I.	Introduction	14
II.	General Experimental Arrangement	15
III.	The Target Chamber	16
IV.	The Preparation of Self-Supporting Boron Targets	18
V.	The Fast Neutron Time-of-Flight Spectrometer	25
VI.	The Charged-Particle Spectrometer	30
CHAPTER III.	EXPERIMENTAL MEASUREMENTS	33
I.	Introduction	33
II.	Pulsed Beam Neutron Time-of-Flight Spectra	34
III.	Measurements Using One Solid State Detector	36
IV.	Measurements Using Two Solid State Detectors	57
V.	Conclusions	59
APPENDIX I.	THE KINEMATICS OF NUCLEAR REACTIONS	61
I.	Introduction	61
II.	Programs	62
A.	Nuclear Reactions I	62
B.	Nuclear Reactions II	78
C.	Nuclear Reactions III	90

Table of Contents (continued)

APPENDIX II.	A TRANSISTORIZED, FREQUENCY MODULATED PROTON MAGNETIC RESONANCE SYSTEM FOR THE MEASURE- MENT AND CONTROL OF MAGNETIC FIELDS	98
I.	Introduction	98
II.	Background and Design Considerations	99
III.	A General Description of the System	108
IV.	Circuits	111
	A. The RF Oscillator	111
	B. The Probes	113
	C. The Preamplifier	114
	D. The Twin Tee Oscillator	115
	E. The Twin Tee Amplifier	116
	F. Modulation Amplitude Control Amplifier	117
	G. 200 cps Compensation Circuit	117
	H. Vertical Amplifier for Indicator Oscilloscope	118
	I. Horizontal Amplifier for Indicator Oscilloscope	118
	J. Phase Sensitive Detector (or Chopper) Driver	119
	K. Phase Sensitive Detector	119
	L. Time Constant Circuit	121
	M. The Power Input Circuit	121
V.	Operation	122
	A. Lining-up Procedures	122
	B. Magnetic Field Measurements	124
	C. Magnetic Field Control	126

FIGURES

		Following Page
1-1	Energy level diagram of C^{12} (Aj 62). Solid arrows indicate reported transitions; broken arrows indicate unestablished transitions.	3
2-1	Accelerator drift tube arrangement.	15
2-2	Target chamber (a) plan view, (b) elevation.	16
2-3	Electron bombardment apparatus.	19
2-4	Design details of electron bombardment apparatus.	19
(a & b)		
2-5	Electronics used in the neutron time-of-flight spectrometer and in the charged-particle spectrometer.	28
3-1	A pulsed-beam neutron time-of-flight spectrum of neutrons produced in the $B^{11}(d,n)C^{12*}$ reaction: $E_d = 1$ MeV, $\theta_n = 25^\circ$, $S_n = 2.8$ meters. Target = 1.2 mg/cm^2 isotopic B^{11} .	34
3-2	A pulsed-beam neutron time-of-flight spectrum produced in the $B^{11}(d,n)C^{12}$ reaction: $E_d = 1$ MeV, $\theta_n = 25^\circ$, $S_n = 2.8$ meters. Target = $15 \text{ } \mu\text{g/cm}^2$ self-supporting, natural boron.	35
3-3	Gamma-ray yield curves showing generating volt-meter calibration and self-supporting, boron target thickness measurement (see text). (courtesy of T.K. Alexander)	35
3-4	Detector geometries for experiments employing (a) one solid state detector, (b) two solid state detectors.	36
3-5	Charged-particle-gated neutron time-of-flight spectrum showing neutron groups leading to the 4.43, 7.65, 9.64, 10.84, 11.83, and 12.71 MeV levels of C^{12} . $\theta_n = 45^\circ$, $S_n = 1.15$ meters, $\gamma = 90^\circ$, $E_d = 1.5$ MeV.	37

(Figures continued)

Following
Page

3-6	Neutron time-of-flight spectra taken with the timing detector in and out of view of the C^{12} (4.43) recoiling nuclei.	38
3-7	Charged-particle-gated neutron time-of-flight spectrum taken with 10 μ in. nickel foil in front of the 'timing' detector. $\theta_n = 45^\circ$, $S_n = 1.42$ meters, $\gamma = 90^\circ$, $E_d = 1.5$ MeV.	39
3-8	(a) Neutron-gated and direct charged-particle spectra	40
	(b) Charged-particle-gated neutron time-of-flight spectrum. $\theta_n = 45^\circ$, $S_n = 1.15$ meters, $\gamma = 90^\circ$, $E_d = 1.5$ MeV.	40
3-9	(a) Neutron-gated and direct charged-particle spectra	40
	(b) Neutron time-of-flight spectrum. $\theta_n = 45^\circ$, $S_n = 1.15$ meters, $\gamma = 130^\circ$, $E_d = 1.5$ MeV.	40
3-10	(a) Neutron-gated and direct charged-particle spectra	40
	(b) Neutron time-of-flight spectrum. $\theta_n = 45^\circ$, $S_n = 1.15$ meters, $\gamma = 240^\circ$, $E_d = 1.5$ MeV.	40
3-11	(a) Neutron-gated and direct charged-particle spectra	40
	(b) Neutron time-of-flight spectrum. $\theta_n = 45^\circ$, $S_n = 1.15$ meters, $\gamma = 265^\circ$, $E_d = 1.5$ MeV.	40
3-12	(a) Angular distributions of alpha particles from C^{12} (12.71) to Be^8 (2.9)	44
	(b) Experimental angular distribution of alpha particles from C^{12} (11.83) to Be^8 (2.9).	44

(Figures continued)

	Following Page
3-13 Angular distributions for alpha particles from $C^{12}(9.64)$ to $Be^8(0)$.	46
3-14 Isometric display of two-parameter data obtained for $\theta_n = 45^\circ$, $S_n = 1.15$ meters, $\gamma = 90^\circ$, $E_d = 1.5$ MeV.	48
3-15 Expanded drawing of charged-particle spectrum no. 3 of Figure 3-14 with three-body breakup distributions.	49
3-16 (a) Neutron-gated and direct charged-particle spectra	53
(b) Neutron time-of-flight spectrum. $\theta_n = 0^\circ$, $S_n = 1.15$ meters, $\gamma = 140^\circ$, $E_d = 1.5$ MeV.	53
3-17 Isometric display of two-parameter data obtained for $\theta_n = 0^\circ$, $S_n = 1.15$ meters, $\gamma = 140^\circ$, $E_d = 1.5$ MeV.	54
3-18 Expanded drawing of charged-particle spectrum no. 5 of Figure 3-17, together with three-body breakup distributions.	55
3-19 Isometric display of two-parameter data obtained for $\theta_n = 0^\circ$, $S_n = 1$ meter, $\theta_{\alpha_T} = 90^\circ$, $\theta_{\alpha_E} = 90^\circ$, $E_d = 1.5$ MeV.	58
3-20 Isometric display of two-parameter data obtained for $\theta_n = 45^\circ$, $S_n = 1$ meter, $\theta_{\alpha_T} = 90^\circ$, $\theta_{\alpha_E} = 85^\circ$.	58

Appendix I

1 Kinematics of the reaction $B^{11}(d,n)C^{12}(12.71)$ for $E_d = 1.5$ MeV.	65
2 Velocity diagrams for Nuclear Reactions I	68
3 Velocity diagrams for Nuclear Reactions I	68

(Figures continued)

	Following Page
4 Velocity diagrams for Nuclear Reactions I	68
5 Wave vector diagram	74
6 Velocity diagram for Nuclear Reactions II	77
7 Nuclear Reactions II output for the alpha- particle decay of the 9.64, 11.83 and 12.71 MeV states of C^{12} to the ground and 2.9 MeV states of Be^8	78
8 Velocity diagram for Nuclear Reactions III	89
9 Typical Nuclear Reactions III output for the reaction $B^{11}(d,n)C^{12*}(12.71)$; $C^{12*}(12.71) \rightarrow$ $\alpha_1(\gamma) + Be^{8*}(2.9) \rightarrow \alpha_1(\gamma) + \alpha_2(\beta_1) + \alpha_3(\beta_2)$.	90

Appendix II

1 Generalized block diagram of transistorized nuclear magnetic resonance system	127
2 (a) Rf oscillator	"
(b) Preamplifier	"
3 Probes	"
4 Twin-tee 200 cps oscillator	"
5 Twin-tee amplifier	"
6 Modulation amplitude-central amplifier	"
7 200 cps compensation circuit	"
8 Vertical amplifier for indicator oscilloscope	"
9 Horizontal amplifier for indicator oscilloscope	"
10 Phase-sensitive detector driver	"
11 Phase-sensitive detector	"
12 Time constant circuit	"

Figures (continued)

		Following Page
13	Power input circuit	127
14	(a) Front view of NMR control panel	"
	(b) Back view of NMR control system showing positions of the various circuits	"
15	(a) NMR head and probe	"
	(b) Rf oscillator and preamplifier modules	"
16	Typical proton signals obtained at one kilogauss for modulation frequencies of (a) 200 cps; (b) 30 cps.	"

CHAPTER I

INTRODUCTION

I. Motivation

It is well known that clusters of nucleons such as deuterons, tritons, helium-3, alpha particles, and other nuclei in their ground and excited states play an important role in the structure of light and medium weight nuclei (Wi 58, Sh 60). In particular, there is considerable evidence to support the Two-Body Cluster Model of Phillips and Tombrello (Ph 60, To 60) in which the wave function of a particular state is expanded in terms of a set of two-body cluster wave functions, the possibility of three or more-body clusters taking part being neglected. This set represents all the possible two-body arrangements, λ , of the clusters that can be formed by the nucleons of a given nucleus, and is considered complete and orthogonal for cluster separations greater than the range of the strong interactions between clusters. For separations less than this range, this set is far from being complete and hence the two-body cluster model is not valid. The expansion coefficients, or the fractional parentage coefficients ($\theta_{2,\lambda}$; where $\sum_{\lambda} |\theta_{2,\lambda}|^2 = 1$ under the two-body assumption), are energy dependent and are directly related to the probability

that the state will decay by the emission of the corresponding cluster or, in other words, they are related to the decay widths. Explicitly,

$$|\theta_{2,\lambda}|^2 \simeq \gamma_\lambda^2 / (3\hbar^2 / 2\mu_\lambda a_\lambda^2)$$

where γ_λ^2 is the reduced width and the denominator is the Wigner limit (Wi 47). μ_λ is the reduced mass of the two-body cluster, and a_λ is the range of the strong inter-cluster forces. The reduced width is related to the observed decay width Γ_λ in the usual way by the penetrability factor P_λ ,

$$\gamma_\lambda^2 = \Gamma_\lambda / 2P_\lambda$$

Thus, if for a given two-body channel λ' , the reduced width $\gamma_{\lambda'}^2$ of a state is near the Wigner limit (i.e., if $|\theta_{2,\lambda'}|^2 \simeq 1$), it may be inferred that the state is well described by the λ' two-body cluster. The measurement of decay widths for particles emitted from excited states of nuclei should therefore lead to information regarding the two-body cluster parentage of the state.

Whether or not the C^{12} nucleus fits into the framework of the Two-Body Cluster Model is uncertain. Many of the states predicted for C^{12} by the more general Cluster Model of Wildermuth and Kallenopoulus (Wi 58) using a Be^8 - α representation and average oscillator potentials (Sh 60) have not been observed.

However, many of the states that have been observed do fit this model quite well. Knowledge of the alpha-particle decay modes of the states in C^{12} , as implied from the energy spectra of the emitted alpha particles, would indicate whether a Be^8 (or Be^{8*}) cluster exists within C^{12} . For, if a given level decays predominantly to the states of Be^8 , then $\sum_s |\langle \theta_{2, Be_s^8 - \alpha} | \rangle|^2 \simeq 1$ (where s denotes the states of Be^8 involved), and that state of C^{12} may be considered as being primarily of $Be^8 - \alpha$ parentage. On the other hand, if the level disintegrates by a direct three-body process, the $Be^8 - \alpha$ two-body cluster is not a good representation of the state.

It is well established that the 7.65 and the 9.64 MeV levels of C^{12} (see Figure 1-1 for an energy level diagram of C^{12}) emit alpha particles exclusively to the ground state of Be^8 , and that the 16.11 MeV level, when it decays by particle emission, primarily feeds the 2.9 MeV level of Be^8 although transitions to the Be^8 ground state and some three-body emission have also been observed. The levels between 13 and 16 MeV excitation have been observed to decay predominantly to $Be^8(2.9)$. It would seem then that these levels do fit into the two-cluster picture of C^{12} , and indeed the spins and parities of the 7.65, 9.64 and the 16.11 MeV states can be explained in terms of the cluster model of Wildermuth and Kallenopoulus (loc. cit.) using the $Be^8 - \alpha$ representation (see reference Sh 60).

Very little or no work has been reported on the alpha-

particle decay of the levels between 9.64 and 13 MeV; namely, the 10.1, 10.84, 11.83, and the 12.71 MeV levels. Since there is speculation (see Chapter III) that the 12.71 and the 11.83 MeV levels might decay by a direct three-body process, in contrast to the sequential process through Be^8 predicted by the Two-Body Cluster Model, an experimental program was initiated to investigate the alpha-particle decay mechanism of these states. That program constitutes the subject matter of this thesis.

II. Survey of the Literature on the Disintegration of C^{12}

The disintegration of C^{12} has been the subject of experimental and theoretical research since 1934 when Chadwick, Feather, and Davies (Ch 34) observed, in a cloud chamber containing methane, a three-pronged star among tracks of protons projected forward by radium-beryllium neutrons. They attributed this event to the reaction, $\text{C}^{12}(\text{n}, \text{n}')3\alpha$.

Dee and Gilbert (De 36) in 1936 provided the first successful analysis of a nuclear reaction in which more than two reaction products were involved, explaining the energy distribution of the alpha particles from the reaction $\text{B}^{11}(\text{p}, \alpha)\text{Be}^8$. In this case, C^{12} at about 16 MeV excitation was involved, the proton bombarding energy being 200 keV. The alpha-particle spectrum was divided into three groups: (a) a homogeneous group at 5.7 MeV, containing about one percent of the alpha particles, and attributed to the $\text{B}^{11}(\text{p}, \alpha)\text{Be}^8(\text{gnd})$ reaction; (b) a broad group at 3.85 MeV, of

width 0.77 MeV, attributed to the $B^{11}(p,\alpha)Be^8(2.9 \text{ MeV})$ reaction;
(c) a continuous group extending from low energies to about 5 MeV, containing twice as many particles as group (b) and attributed to the alpha-particle breakup of the first excited state of Be^8 .

In 1949, Hanni, Telegdi, and Zunti (Ha 48) discovered the photodisintegration of carbon in nuclear emulsions when they observed three-pronged stars in plates which had been exposed to gamma rays obtained from the bombardment of lithium with protons. The analysis of these stars led to the result, similar to that of Dee and Gilbert (De 36), that the breakup of C^{12} proceeded predominantly through the first excited state of Be^8 . There was no evidence in this work for any direct three-body decay of C^{12} .

Since this work, many experimenters have investigated the $C^{12}(\gamma,3\alpha)$ reaction (Te 50, Go 50, Te 51, Wi 53, El 52, Go 53, Li 53, Mi 53, So 55, Ha 55, Ma 58, To 60a, Se 61) using nuclear emulsion techniques at gamma-ray energies up to 300 MeV. The cross section shows two broad peaks at gamma-ray energies of 19 and 29 MeV, and a pronounced minimum at 21 MeV, the region of the (γ,n) giant resonance. It is zero above 42 MeV. For gamma-ray energies below 19 MeV, the decay of C^{12} proceeds predominantly through the first excited state of $Be^8(2.9 \text{ MeV})$, and for energies above 26 MeV the reaction goes via the ground state of Be^8 (12 percent) or through the states in Be^8 in the

region of 17 MeV excitation. In the region between 19 and 26 MeV in gamma-ray energy, the number of events which go through the ground state of Be^8 increases with energy from 5 to 18 percent. Decay to the 2.9 MeV state can account for at most one-third of the events in this region. It is uncertain whether higher states in Be^8 or direct three-body decays are involved in the remainder of the events.

Many other reactions and experimental techniques have been employed to investigate the mechanism of the breakup of C^{12} into three alpha particles. These will be mentioned and discussed in the following summary of the information available on this process for each level of C^{12} from the breakup threshold (7.281 MeV) to the 16.11 level.

(a) The 7.656 State

1. Miller, Rasmussen, and Sampson (Mi 55) investigating the $\text{C}^{12}(\alpha, \alpha')\text{C}^{12*}$ reaction with 22 MeV alpha particles failed to observe the C^{12} recoil corresponding to the alpha group leaving C^{12} excited to this level. They estimated that the probability of the decay proceeding through Be^8 as greater than 80 percent.

2. Bent, Bonner, McCrary, and Ranken (Be 55) using the $\text{Be}^9(\alpha, n)\text{C}^{12*}$ reaction to feed the 7.65 state and a magnetic lens pair spectrometer to study the subsequent radiations, concluded from the relative intensities of the 4.4 MeV gamma radiation and the internal pair line that the 7.65 state breaks up into

$\text{Be}^8 + \alpha$ with a probability greater than 96 percent.

3. Cook, Fowler, Lauritsen and Lauritsen (Co 57) were the first to observe the alpha-particle decay of the 7.65 level. They measured the alpha-particle spectrum associated with the β^- decay of B^{12} formed by the deuteron bombardment of B^{11} , and concluded that the 7.65 MeV state breaks up into alpha particles via Be^8 and that the results are inconsistent with a direct three-body decay process.

(b) The 9.64 State

1. Livesey and Smith (Li 53) reexamined photographic plates exposed to neutrons from deuterons on lithium by Green and Gibson (Gr 49). The energy spectrum of the inelastically scattered neutrons showed two peaks corresponding to energy levels in C^{12} at 9.6 and 11.8 MeV. The events which were attributed to the 9.6 level were consistent with the assumption that they involved the ground state of Be^8 . The events attributed to the 11.8 level went through the first excited state at 2.9 MeV.

2. Jackson and Wanklyn (Ja 53) investigated the disintegration of C^{12} using fast neutrons (E_n up to 45 MeV) from the proton bombardment of Be^9 , and cloud chamber techniques. For E_n less than 20 MeV, most of the events proceed to the ground state of Be^8 through a level in C^{12} at $10 \pm .8$ Mev.

3. Frye, Rosen, and Stewart (Fr 55) irradiated C-2 emulsions with neutrons of fifteen discrete energies in the range 12-20

MeV (obtained from the $T(d,n)He^4$ reaction), and found evidence for the excitation of the 9.6 level in C^{12} and the ground and 2.9 states in Be^8 . Six events appeared to have gone through the 7.65 state in C^{12} .

4. Perkins (Pe 51) also investigated the disintegration of C^{12} by neutrons. He irradiated nuclear emulsions with neutrons (E_n up to 24 MeV) obtained from the $Li^7 + d$ reaction. All 485 stars examined indicated that the disintegration proceeded through Be^8 . No particular levels of C^{12} were specified.

5. Vasil'ev, Komarov, and Popova (Va 58) exposed nuclear emulsions to neutrons of energy up to 19 MeV obtained from the $Li^7(d,n)$ reaction. In contrast to other work on the inelastic scattering of neutrons from C^{12} (Pe 51, Ja 53, Fr 55), the research of these experimenters indicates that a large fraction of the disintegrations occur without the formation of any intermediate nuclei. For example, in the neutron energy range from 9 to 11 MeV only 10 percent of the events involve the C^{12} nucleus (below 9.6 MeV), and only 40 percent of these events involve Be^8 . These values are typical for the entire neutron energy range studied. The energy distribution of the reaction products follows a statistical (phase space) distribution.

6. Need (Ne 55) bombarded methane in a cloud chamber with 29 MeV protons to investigate the mechanism of the $C^{12}(p,p')3\alpha$ reaction. He excited levels in C^{12} near 9.6, 12, 16, 20, and 25

MeV and found that the 9.6 level decayed entirely to the ground state of Be^8 . The level in the vicinity of 12 MeV went to either the ground state or the first excited state of Be^8 with about equal probability. The levels between 13 and 16 MeV were found to decay to the ground state of Be^8 in less than five percent of the cases, with the rest going to the 2.9 state of Be^8 . For the levels at 20 and 25 MeV, it was estimated that 16 ± 9 percent and 27 ± 10 percent respectively of the events involved Be^8 in its ground state, and that between one-third and one-half of the remaining events proceeded through the 2.9 level in Be^8 . The mechanism for the remaining events was uncertain. There was no evidence of direct four-body decay of N^{13*} . In similar experiments, Vasil'ev, Komarov, and Popova (Va 63) using protons in the energy range from 15 to 29 MeV found that the primary mode of decay is through the N^{13*} compound system to Li^5 and Be^8 in the ground, 2.9, and 11.3 MeV states. Another group of Russian experimenters, Vasil'ev, Komarov, Koshelyaev, and Popova (Va 60), observed direct interactions of the p- α type in their measurements on the angular distribution of alpha particles from the reaction $\text{C}^{12}(\text{p}, \text{p}')3\alpha$, for a proton energy of 29 MeV.

7. LaSalle, Bent, and Cramer (La 63), using two solid state detectors and two-parameter pulse-height analysis to look at fast coincidence events between inelastically scattered alpha particles (bombarding energy of 22.5 MeV) and those resulting from the breakup of unbound levels in C^{12} , concluded that the

disintegration of the 9.64 level goes primarily by a two-body process through Be^8 . LaSalle, Cramer, and Eidson (La 63a) measured the angular correlation of the alpha particles from the breakup of the 9.64 state to the ground state of Be^8 and confirmed the spin assignment of 3^- for this state in C^{12} .

8. Vasil'ev, Komarov, and Popova (Va 62) also initiated the disintegration of C^{12} using alpha particles at 23 MeV. They conclude that the decay of C^{12} into three alpha particles proceeds with high probability through the direct decay of the compound system O^{16*} . The intermediate nucleus, Be^8 , appears as the result of the resonance interaction of the final state alpha particles.

9. Bogatin, Novak, and Ostroumov (Bo 63) used nuclear emulsions to study the breakup of C^{12} induced by the inelastic scattering of 80 MeV π^+ mesons. The excitation of the 9.6 MeV level was found to contribute about 20 percent to the reaction cross section. The energy distribution of the alpha particles from this state was explained on the basis of the assumption of a resonance interaction between the final state alpha particles.

10. Work on the photodisintegration of oxygen (Da 56, Aj 59) indicates that for gamma-ray energies below 22 MeV, the reaction takes place mainly through the 9.64 and the 10.8 MeV states of C^{12} to the ground state of Be^8 .

11. Brown and Knowles (Br 62) from work on the alpha-particle bombardment of C^{12} using 25 MeV projectiles confirmed that the 9.64 MeV state decays exclusively to Be^8 .

(c) 10.1 State

1. See item (b)2.

2. Cook, Fowler, Lauritsen, and Lauritsen (Co 58) observed the formation of the 10.1 state in C^{12} in the β^- decay of B^{12} . More than 96 percent of the events corresponding to this level decayed to the ground state of Be^8 , with Be^8 (2.9 MeV) involved in the remaining events. Direct three-body disintegration was ruled out on the basis of the shape of the alpha-particle energy distribution.

3. Wilkinson, Alburger, Gallmann, and Donovan (Wi 63) more recently confirmed the work of Cook et al (Co 58) in their investigations into the alpha-particle emission following the beta decays of B^{12} and N^{12} .

(d) The 10.84 State

No work has been reported on the alpha-particle breakup of this level other than that cited in item (b)2 and item (b)10.

(e) The 11.84 State

1. See item (b)1.

(f) The 12.71 State

1. See item (b)6.

2. Vasil'ev et al (Va 63) found evidence for the formation of a level near 12.7 MeV in C^{12} in their work on the proton bombardment of carbon, for proton energies in the range 15 to 20 MeV. There was also evidence for the 0, 2.9, and the 11.8 MeV states in Be^8 .

(g) States Between 13 and 16 MeV

1. See item (b)6.

(h) The 16.11 MeV State

1. The $B^{11}(p,\alpha)Be^{8*}$ (2.9 MeV) is a very well established reaction and was in fact one of the first of all nuclear reactions to be investigated. Dee and Gilbert (De 36) were the first to explain the breakup of this level on the basis of the existence of an unstable Be^8 nucleus of very short life, as mentioned earlier.

2. Geer, Nelson and Wolicki (Ge 55) assigned spin-parity values of 2^+ for both the 16.11 MeV state of C^{12} and 2.9 MeV state of Be^8 on the basis of angular correlations between the alpha particle leading to $Be^8(2.9)$ and one of the alpha particles from the breakup of this level.

3. Beckner, Jones, and Phillips (Be 61) employed a magnetic spectrometer to resolve the reaction products produced in the $B^{11}(p,\alpha)Be^8$ reaction, and compared the alpha-particle continuum with the shape predicted by the generalized density-

of-states function of Phillips, Griffy, and Biedenharn (Ph 60a) which is based on the assumption that the three-body decay proceeds sequentially through Be^8 . The comparison is good and therefore seems to confirm this mode of decay.

4. Dehnhard, Kamke, and Kramer (De 61) suggest a simultaneous breakup of this level within the resonance ($E_p = 163$ keV), and confirm the sequential process through Be^8 for proton energies immediately above and below this resonance.

5. Bronson, Simpson, and Phillips (Br 63) investigated this reaction using two solid state detectors and two-parameter analysis techniques. Dalitz plots of the energy distribution showed peaks corresponding to known levels in Be^8 , in particular, the ground and 2.9 levels.

CHAPTER II

EXPERIMENTAL APPARATUS

I. Introduction

The alpha-particle breakup of the 12.71 and the 11.83 MeV levels in C^{12} , fed by the $B^{11}(d,n)C^{12}$ reaction, was studied using neutron time-of-flight techniques and charged particle spectrometry. A self-supporting, natural boron target of thickness $15 \mu\text{gms/cm}^2$ was bombarded with 1.5 MeV deuterons obtained from the University of Alberta 2 MeV Van de Graaff accelerator. The states of C^{12} were selected by a neutron time-of-flight spectrometer designed by Neilson et al (Ne 59), and the alpha particles from the decay of these states were detected by solid state surface barrier detectors located in the primary reaction plane. Zero-time reference pulses for the neutron spectrometer were generated from the detected associated alpha particles by means of a fast electronic system developed by Alexander and Neilson (Al 63).

Two experiments were performed in this investigation. In the first, one solid state detector was employed, and the charged particle and the neutron time-of-flight spectra were analyzed by a two-parameter, 1024 channel, TMC* pulse-height analyzer operating in the 32 x 32 mode, and a single-parameter 256 channel, TMC* unit.

* Technical Measurements Corporation, 441 Washington Avenue, North Haven, Connecticut

In the second experiment, two solid state detectors viewed the target. One of these provided the timing pulses while the other, gated by the "timing" detector, provided coincidence particle spectra which were also analyzed with the neutron time-of-flight spectrum by the two-parameter analyzer.

II. General Experimental Arrangement

The deuterons for this experiment were obtained from the University of Alberta 2 MeV Van de Graaff accelerator manufactured by High Voltage Engineering Corporation. This machine provides an energy stability of about ± 3 kev. It is located, together with a beam deflecting system and the analyzing magnet, in a room with 24 inch thick concrete walls to keep gamma and neutron background to a minimum. The accelerator drift tube arrangement is shown in Figure 2-1. To provide additional background reduction, the drift tube is encased in a one inch thick lead sheath from the point where it enters the target room to approximately one meter from the target chamber. Additional lead and 4 inches of a paraffin-lithium carbonate mixture surround the carbon trap, the energy stabilizing slits, and a retractable beam viewer (not shown). Because the target room is of light construction and has a fifteen foot square and seven foot deep excavation under the floor at the target position, neutron scattering is kept to a minimum.

The neutron detector carriage was mounted on a boom which pivoted about a point directly below the center of the target chamber.

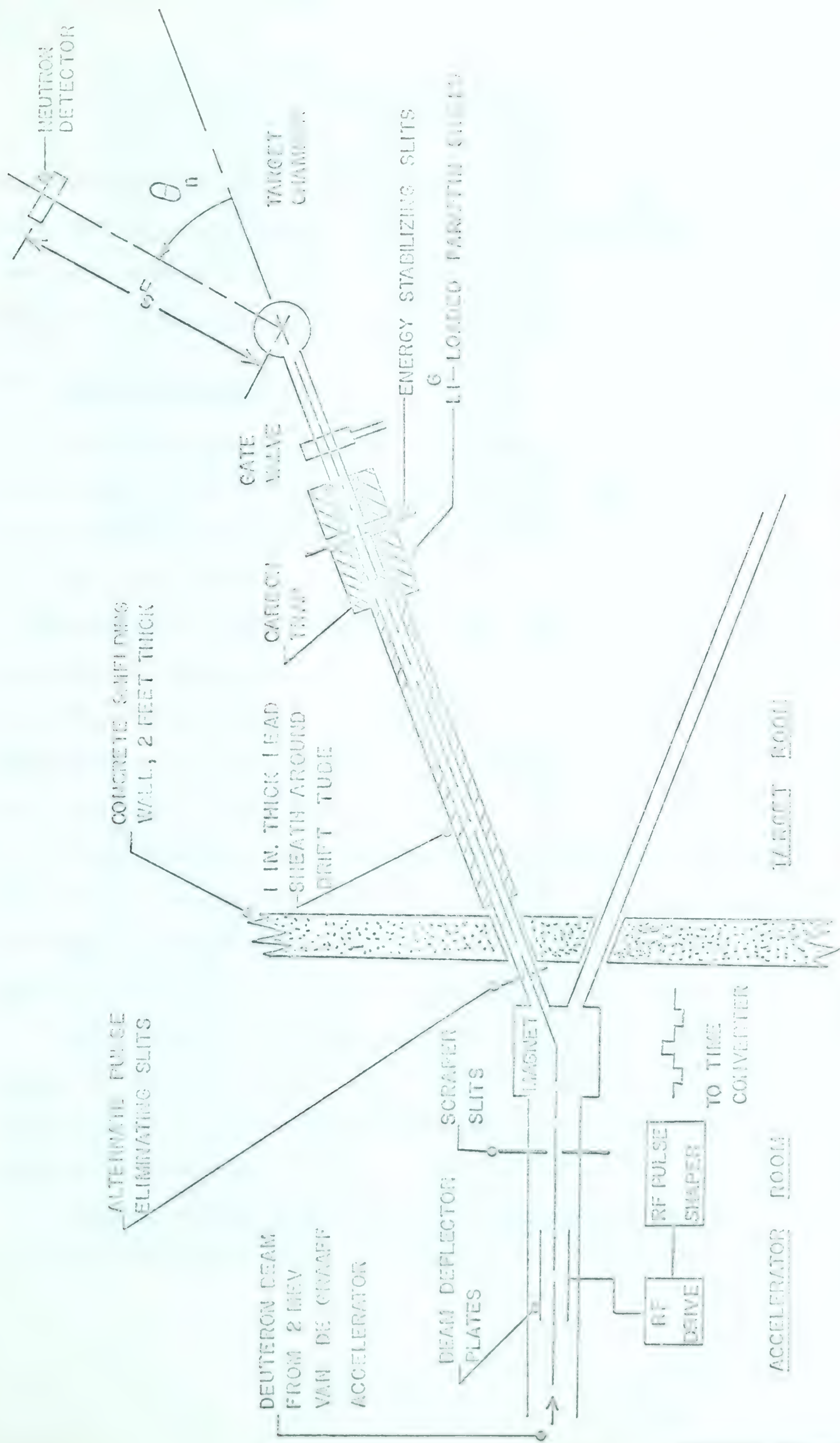


Figure 2-1. Accelerator drift tube arrangement.

The neutron flight path was adjusted by sliding the carriage along the boom, and the angular position of the detector was read from a protractor. The solid state detectors were mounted inside the target chamber which will be described in the following section.

III. The Target Chamber

The target chamber used in these experiments is shown in plan and elevation views in Figure 2-2. Its design was conceived by the chief technician of our laboratory, Mr. J.B. Elliott.

The target was held in position at the center of the chamber in a stainless steel frame A, whose vertical and lateral position as well as angular position in the reaction plane (the horizontal plane) could be externally adjusted. The mechanism providing this adjustment was mounted on the half inch thick teflon base plate of the chamber, thus insulating the target from ground.

A brass Faraday cup, B, mounted on a brass rod which passed through the base plate was used to collect the beam after it had passed through the target. Actually, the target holder and the Faraday cup were connected together so that a true current reading would be obtained.

Beam alignment on the target was facilitated by the quartz viewer, C, also mounted on a brass rod passing through the teflon base plate. It could be positioned directly in front of the beam entrance to the chamber.

Provision was made to allow two solid state detectors to view the target. One of the detectors was mounted in a transistor socket

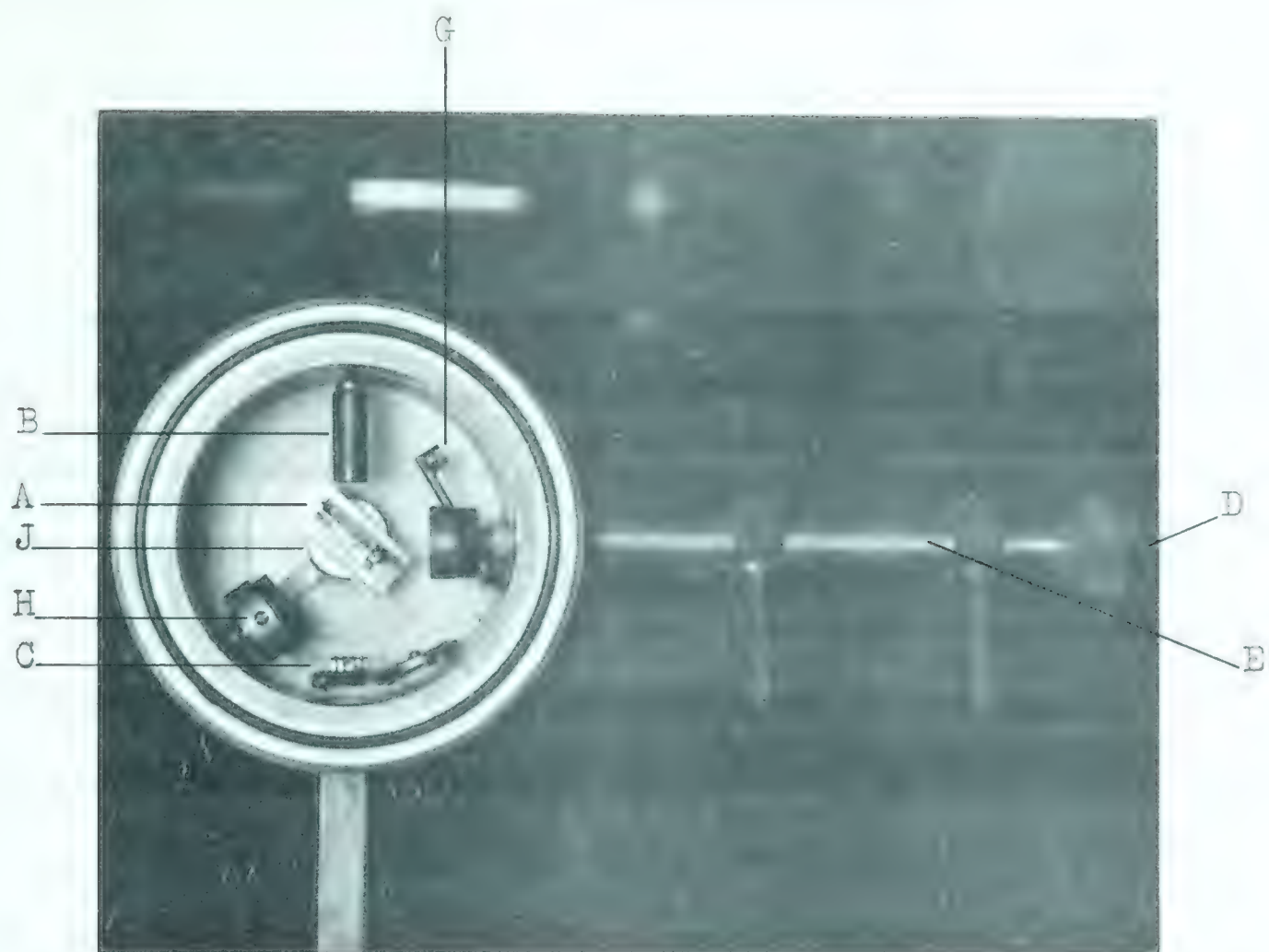


Figure 2-2. Target chamber (a) plan view



(b) elevation.

on the end of the stainless steel tube D, which slips inside the brass tube E. An O-ring was used to effect the vacuum seal between these two tubes. The brass tube was welded to a stainless steel strap F, 1.25 in. wide and .010 in. thick, which provided a sliding vacuum seal over a .5 in. wide slot cut in the wall of the chamber. This arrangement permitted the continuous adjustment of the angular position of the detector from zero to $\pm 140^\circ$ with respect to the beam direction. The signals from this detector were brought to a BNC connector mounted on the end of the stainless steel tube D.

The other detector was mounted in a holder, H, fastened to but insulated from a rotatable brass sleeve J which was part of the target-holding assembly. Thus, continuous adjustment of its angular position was also available. The signals from this detector were brought out of the chamber by means of a brass rod that passed through the teflon base plate. Both detectors could be set to approximately $\pm 1/4$ degree, and electrical grounding was made to the body of the chamber.

During the course of an experiment, both the top and the bottom of the chamber were electrically shielded by aluminum covers.

In order to facilitate the calibration of the solid state detectors at any time during the course of an experiment, a Pu^{239} alpha-particle source was mounted inside the chamber on the end of another brass rod, G, whose position could be adjusted from outside the chamber.

IV. The Preparation of Self-Supporting Boron Targets

(a) Introduction

The use of solid state counters to detect nuclear reaction products necessitates the use of targets which have little or no backing material. The elastic scattering of the incident beam into the counter by a thick, or thickly backed, target would cause serious electronic pile-up and would unduly shorten the lifetime of the detector. Thin self-supporting targets are also desirable from the point of view of keeping the energy degradation of the reaction products to a minimum, thus facilitating the identification of the various reactions taking place.

Self-supporting boron (natural B^{11} and separated B^{10}) targets, 3/8 in. to 1/2 in. in diameter and ranging from 10 to 25 $\mu\text{gms}/\text{cm}^2$ were prepared by vacuum evaporation techniques using electron bombardment heating.

In electron bombardment heating, a focussed beam of electrons impinges directly on the surface of the material to be evaporated. This is a very efficient method of vapour source heating, and is superior to most other methods because the highest temperature region is the surface of the evaporant itself rather than the crucible supporting the evaporant. Thus by maintaining the temperature of the crucible-evaporant interface at a low level, it is possible to reduce the degree to which an active evaporant attacks the support material, prolonging crucible life, and keeping to negligible proportions target contamination by the support material.



Figure 2-3. Electron bombardment apparatus

Resistance heating of the boron using crucible-filaments made of refractory metals such as tantalum, tungsten, or molybdenum proved to be impossible because of the reactivity of the boron with these metals at the temperatures required for the volatilization of the boron (2300°C). The use of carbon crucibles was ruled out because of the carbon contamination of the boron targets which would have resulted.

(b) The Electron Bombardment Apparatus

The electron bombardment apparatus was a modified version of a design given by Muggleton and Howe (Mu 61), and is shown in Figure 2-3. Figures 2-4a and 2-4b contain the design details of the parts involved. The apparatus was mounted on a Veeco^{*} vacuum system, model VS-9, which is equipped with a two inch oil diffusion pump and a rotary forepump. The pumping speed provided by this system is satisfactory for resistance heating evaporation, but is just barely adequate for electron bombardment evaporation. Because of this fact, the material in the pumping path from the crucible to the vacuum system was kept to the absolute minimum.

With reference to Figure 2-4a, it can be seen that this type of heating device is basically a simple diode. It was mounted on a 14 in. diameter, 1 in. thick, stainless steel base plate and contained in a 12 in. diameter bell jar. The anode was formed by the tantalum crucible A and its tungsten support rod B which was insulated from the base plate by the Kovar^{**} insulator C. The

* Vacuum Electronic Engineering Co.

** Available from Stupakoff Ceramic & Manufacturing Co., Latrobe, Penn

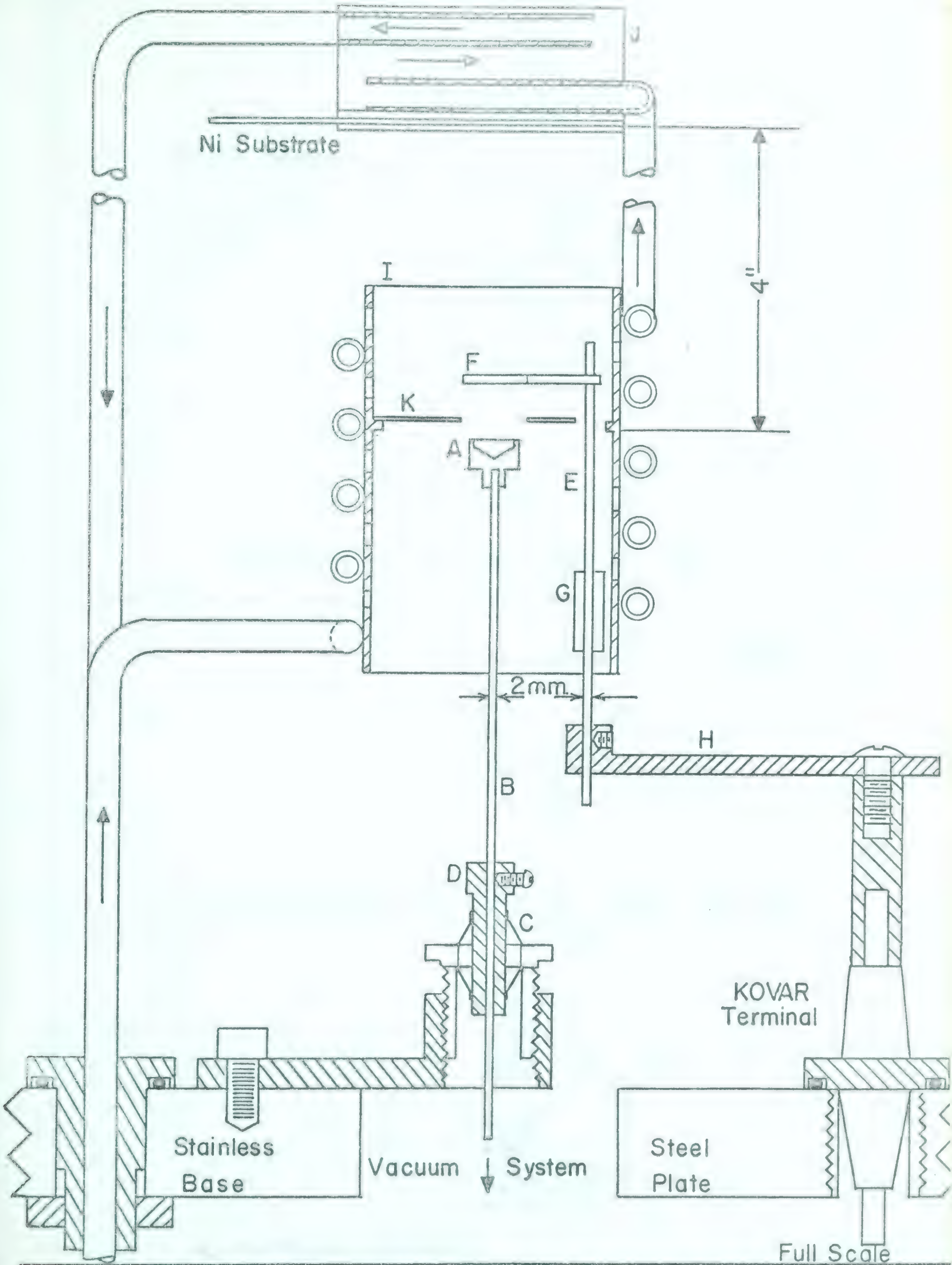
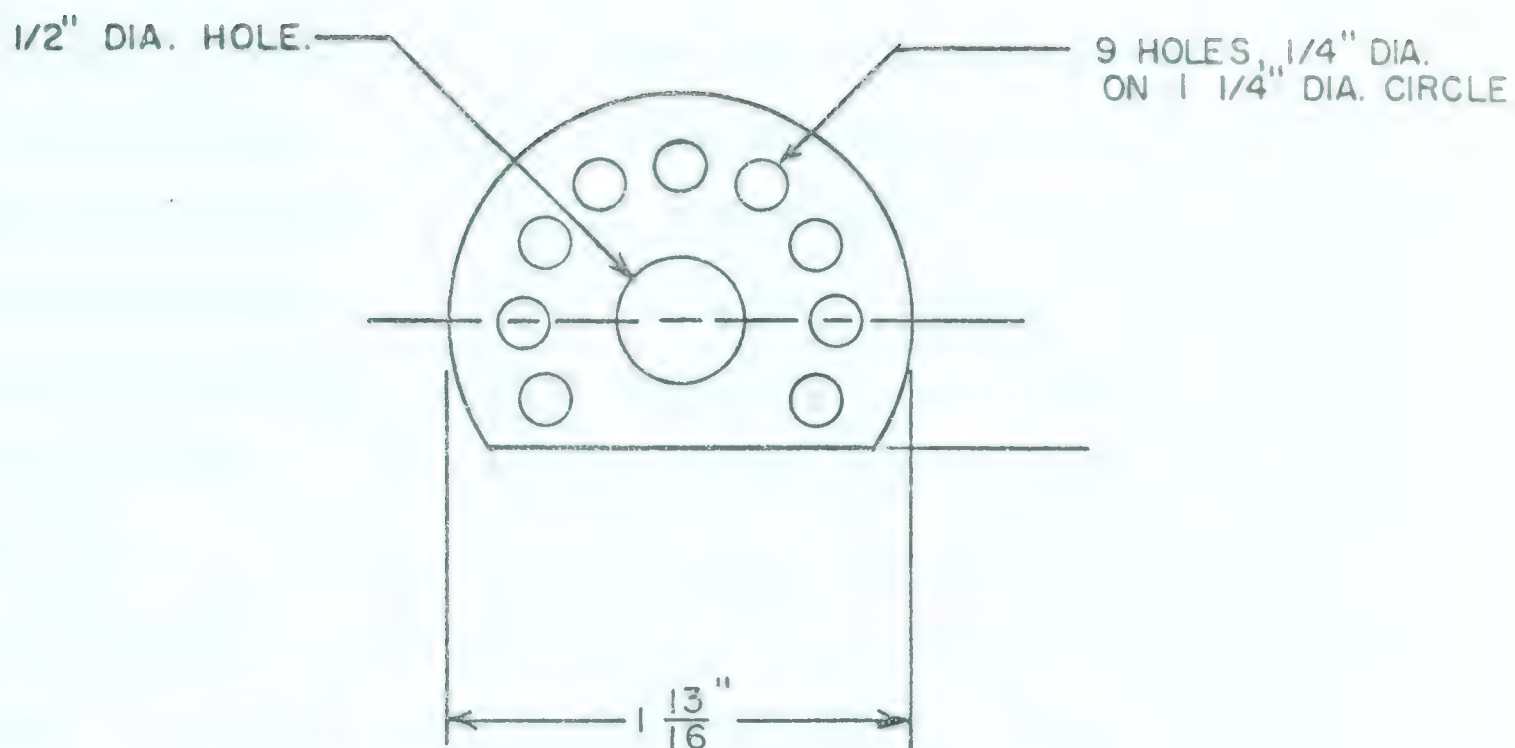
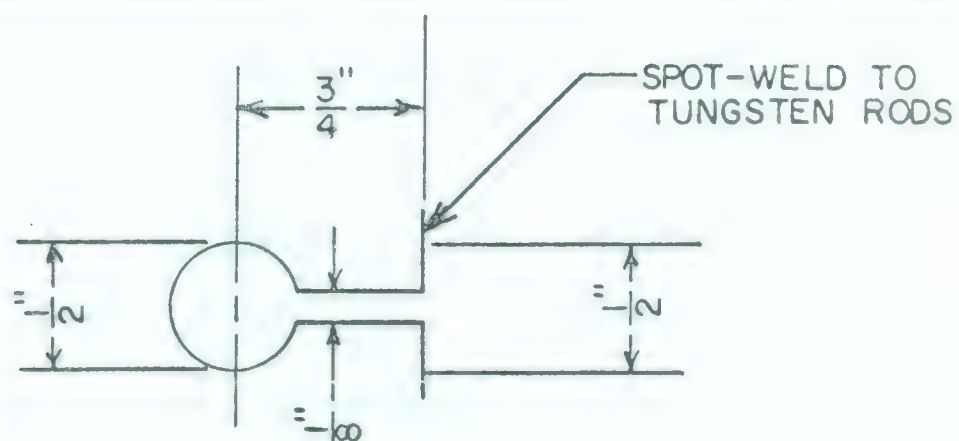


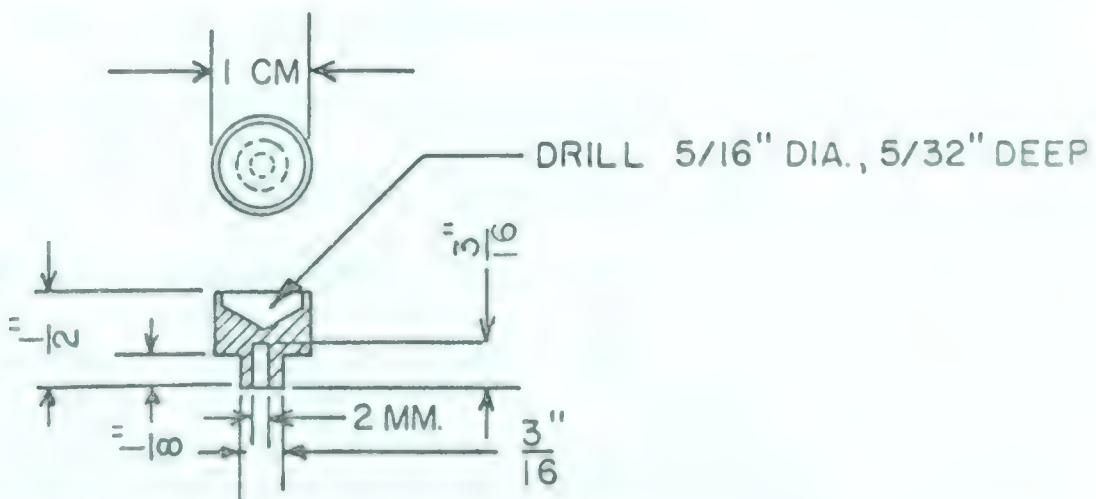
Figure 2-4(a). Assembly drawing of electron bombardment apparatus.



K. FOCUSING ELECTRODE, 0.010" MOLYBDENUM



F. FILAMENT, 1/16" WIDE STRIP OF 0.005" TANTALUM



A. TANTALUM CRUCIBLE

Figure 2-4(b). Electron bombardment apparatus; electrodes.

support rod was a sliding fit in the brass boss D to provide easy height adjustment of the crucible. A glass insulated lead was used to connect the anode to one of the type 95.0056 Kovar terminals mounted on the base plate. An NJE^{*} 5 kv, 0-500 milliampere, dc power supply was used as the high voltage source for this system. The filament (cathode), F, consisted of a 3 in. x 1/16 in. strip of .005 in. thick tantalum, spot welded to two tungsten rods E, and shaped as shown in Figure 2-4b with a 1/2 in. diameter loop in the center. The two filament support rods were held rigidly 3/4 in. apart by the ceramic spacer, G, and were connected to two of the Kovar terminals on the base plate through the bars H. The filament current supply was rated at 12 KVA, or 50 amperes at 24 volts.

A water cooled heat shield, I, was necessary to protect the bell jar from the intense heat generated during the evaporation process. It was also found essential to provide water cooling, J, to the substrate onto which the boron was to be evaporated to prevent the deposited film from rupturing.

Electrons emitted from the filament were focussed onto the surface of the boron in the crucible by the molybdenum focussing electrode K which rested on a ledge machined into the heat shield. The size of the aperture in this electrode, the diameter of the filament, and the geometry of the anode-focussing electrode-filament system determined the electron spot size and the dc voltage and current required to achieve the evaporation temperature.

* NJE Corporation, Kenilworth, N.J.

(c) Procedure

A nickel slide, 3 in. x 1 in. x .020 in., cleaned in a concentrated sulphuric acid-chromic acid cleaning solution and rinsed in distilled water, was used as the substrate for the evaporated boron. To facilitate the subsequent stripping of the film, the slide was coated on one side with a thin layer of a liquid detergent, Teepol*, and polished vigorously with grease free tissues. The treated slide was then placed into the water cooled holder, Teepol side down, and copper shims were inserted behind the slide to ensure good thermal contact with the cooling jacket. All handling of the substrate was done with tweezers.

Prior to the positioning of the substrate, the tantalum crucible was cleaned in the same manner as the slide, and filled with boron. The diode geometry was then set. Best results were obtained with the diameters of the aperture of the focussing electrode and the filament fixed at 1/2 in. The (top of the) crucible and the filament were positioned 1/8 in. below and 1/4 in. above the focussing electrode respectively. The spot size corresponding to this geometry at the evaporating conditions of voltage and current was approximately 1/8 in. in diameter. To ensure reasonable uniformity of the boron deposit over the slide, the distance from the vapor source to the substrate was permanently fixed at 4 inches.

The evaporation chamber was then pumped down to a pressure of approximately 1×10^{-5} mm of mercury. Before turning on the filament current, a 3 in. diameter shadow shield was placed between

* Teepol Liquid Detergent -- Available from Shell Oil Co.

the substrate and the crucible to minimize the deposition of contaminants on and to avoid undue heating of the substrate during the outgassing process.

The filament temperature was then raised to approximately 1500°C, as determined by an optical pyrometer, by setting the filament current to approximately 20 amperes. After allowing about 15 minutes for the outgassing of the filament, the positive voltage was applied to the anode and gradually increased to 500 volts. A condition of space charge limited emission from the filament was established by adjusting the filament current to a value above which there was no further increase in the anode current. These conditions were maintained until the boron and the crucible were outgassed which, for a fresh boron charge, took the order of twenty minutes. The high voltage was then very slowly increased, maintaining space charge limited emission and never allowing the pressure rise above 2×10^{-5} mm of Hg, until the boron started to evaporate. With the geometry used, a satisfactory rate of evaporation took place at a voltage setting of 3000 volts and an anode current of 100 milliamperes. Overheating was avoided as it caused spitting of the boron which resulted in pinholed films and undue loss of boron from the crucible.

When the above evaporation conditions were reached, the nickel substrate was exposed to the vapor source. Exposure times for films between 10 and 25 $\mu\text{gms}/\text{cm}^2$ thick ranged from 5 to 10 minutes. Thicker targets could be made by increasing the exposure time, of

course; however, films thicker than about $25 \mu\text{gms}/\text{cm}^2$ were very difficult to strip as they tended to curl up when released from the substrate.

The pressure of the system during the evaporation period should be kept below 1×10^{-5} mm of Hg to avoid discharges from the anode to ground.

At the end of the evaporation, the high voltage and the filament current were turned off, and the system was allowed to cool for about ten minutes before being vented to the atmosphere.

The boron film was released from the substrate by slowly sliding it into a solution of aqua-regia (one part water, one part concentrated HCl, and three parts concentrated HNO_3) at a very small angle with respect to the surface of the solution. This solution etches the nickel at the boron-nickel interface without attacking the boron film. Prior to this releasing procedure, the film was scored into 1 in. squares, and the edges of the substrate were rubbed with a wooden pencil in order to loosen the film at its edges. When the first section of the film was released, the substrate was removed from the acid solution and dipped into distilled water at an angle of about 30 degrees with respect to the water surface. The surface tension of the water lifted the film cleanly from the substrate. Care was taken to prevent water from creeping over the top of the film so that it would not curl up or sink when it became free of the substrate.

Before releasing the other sections of the film, the first

one was mounted on a target frame. The frame, which was a $1\frac{1}{4}$ in. x $\frac{3}{4}$ in. x $\frac{1}{32}$ in. piece of brass or nickel plate with a $\frac{3}{8}$ in. or $\frac{1}{2}$ in. diameter hole in the center, was placed under the floating film and raised vertically, allowing a small strip of the film to wrap around the edge of the frame. The edges of the aperture in the frame were highly polished to prevent the film from tearing on sharp corners. Excess water was carefully blotted from the frame before it was placed in a draught-free atmosphere to dry. The finished target was then stored in a vertical position in a tightly closed plastic box. Mechanically, the targets were extremely fragile when wet but became more rugged with drying. However, extreme caution was always required when they were handled.

These targets, because boron is practically a refractory material itself, were able to withstand a considerable amount of bombardment by the beam of the Van de Graaff accelerator. For example, one target withstood a 0.2 μ amp beam of 1.5 MeV deuterons for the equivalent of about one week's continuous running before it had to be replaced.

In general, the purity of the targets was very good. Carbon and oxygen were the chief contaminants, and even these were just barely detectable in some targets. The degree of oxygen contamination depended on the length of time the film was exposed to the aqua-regia stripping solution. This time was therefore kept to a minimum.

The thickness of the target used in most of the experiments

was measured by T.K. Alexander of this laboratory using the 873 keV resonance in the $F^{19}(p,\alpha,\gamma)O^{16}$ reaction. The gamma-ray yield was measured with and without the boron target in front of a thick fluorine target as a function of the proton bombarding energy. Figure 3-3 shows the two yield curves obtained. The thickness of the boron target in keV was taken as the shift in the position of the low energy side of the yield curve, which was in this case 5 keV for the 873 keV protons. This corresponds to approximately $15 \mu\text{gms}/\text{cm}^2$ of boron.

V. The Fast Neutron Time-of-Flight Spectrometer

The neutron time-of-flight spectrometer used in the experiments to be described in this thesis was designed by Neilson et al (Ne 59, Ne 60, Ne 62). Because its "start" pulses were obtained in a manner not treated in detail in these references, and for the sake of completeness, a brief discussion of the instrument will be given here.

This spectrometer was designed to determine the energy of neutrons in the MeV range where the flight times are of the order of tens of nanoseconds. To this end, it detects and measures the times of flight of neutrons produced in nuclear reactions, the flight path being defined by the distance between the target and the neutron detector. For each time measurement there are two pulses required; a "start" or zero-time reference pulse which is linearly related to the time at which the neutron generating reaction

takes place, and a "stop" pulse which indicates the arrival of the neutron at the detector. A time-to-amplitude converter is used to produce an output whose amplitude is proportional to the extent of the overlap of these two pulses. In other words, the output is proportional to $(1 - t/T)$, where T is the length of the "start" and "stop" pulses, and t is the delay between the front edges of these pulses and, of course, is a direct measure of the neutron flight-time. The neutron energy (nonrelativistic) is simply related to the flight time by the formula, $t_n = 72.3/E_n^{1/2}$ nanoseconds/meter, where E_n is the neutron energy in MeV.

There are three methods by which the "start" pulses can be derived for this instrument. Two of these involve detecting the associated gamma-rays and charged particles resulting from the decay of states, bound and unbound respectively, formed in stripping reactions. The third method employs beam pulsing techniques and can be used independent of the type of reaction producing the neutrons. Here the bombarding beam of particles is pulsed onto the target for very short periods of time, typically one nanosecond, at a rate of 1.67 mc/s. The method used to pulse the beam is described in detail in the above references but will be mentioned here briefly because this technique was employed in some preliminary measurements of this work.

The zero-time reference pulses are derived from a signal induced in a pick-up loop by the sinusoidal voltage used in sweeping the dc beam of the Van de Graaff accelerator across the "scraper" slits

(see Figure 2-1). This signal is shaped and squared to produce one positive, 150 nanosecond wide, "start" pulse for each rf cycle. There are two current bursts produced by the pulsing system per rf cycle, only one of which can be used (providing two timing pulses per rf cycle would be unsatisfactory because the two beam pulses form separate spots on the target, have different flight times to the target, resulting in increased time dispersion, and probably contain different amounts of current). The unwanted pulse can be eliminated electronically by the Alternate Pulse Eliminator, or mechanically by means of an adjustable slit system in the drift tube immediately following the analyzing magnet (utilizing the fact that the two pulses are physically separated in space). A 300 nanosecond delay line (Telcon^{*} AS-48) is used to obtain the correct phasing between the "start" pulse and the beam pulse.

Another method of obtaining the "start" pulse using the pulsed beam is to sense the beam pulses at the target, or at the Faraday cup, and convert them into the zero-time reference by means of the electronics described by Alexander (A1 63). This method has the particular advantage of eliminating the variation in the flight time of the beam burst in its travel down the drift tube from the point of formation approximately 6 meters distant from the target. This dispersion results from the variation in the incident beam energy, which is approximately ± 3 keV.

In the method of obtaining the "timing" pulses by detecting the associated charged particles from the decay of unbound states

* Telcon Works, Greenwich, S.E. 10, England

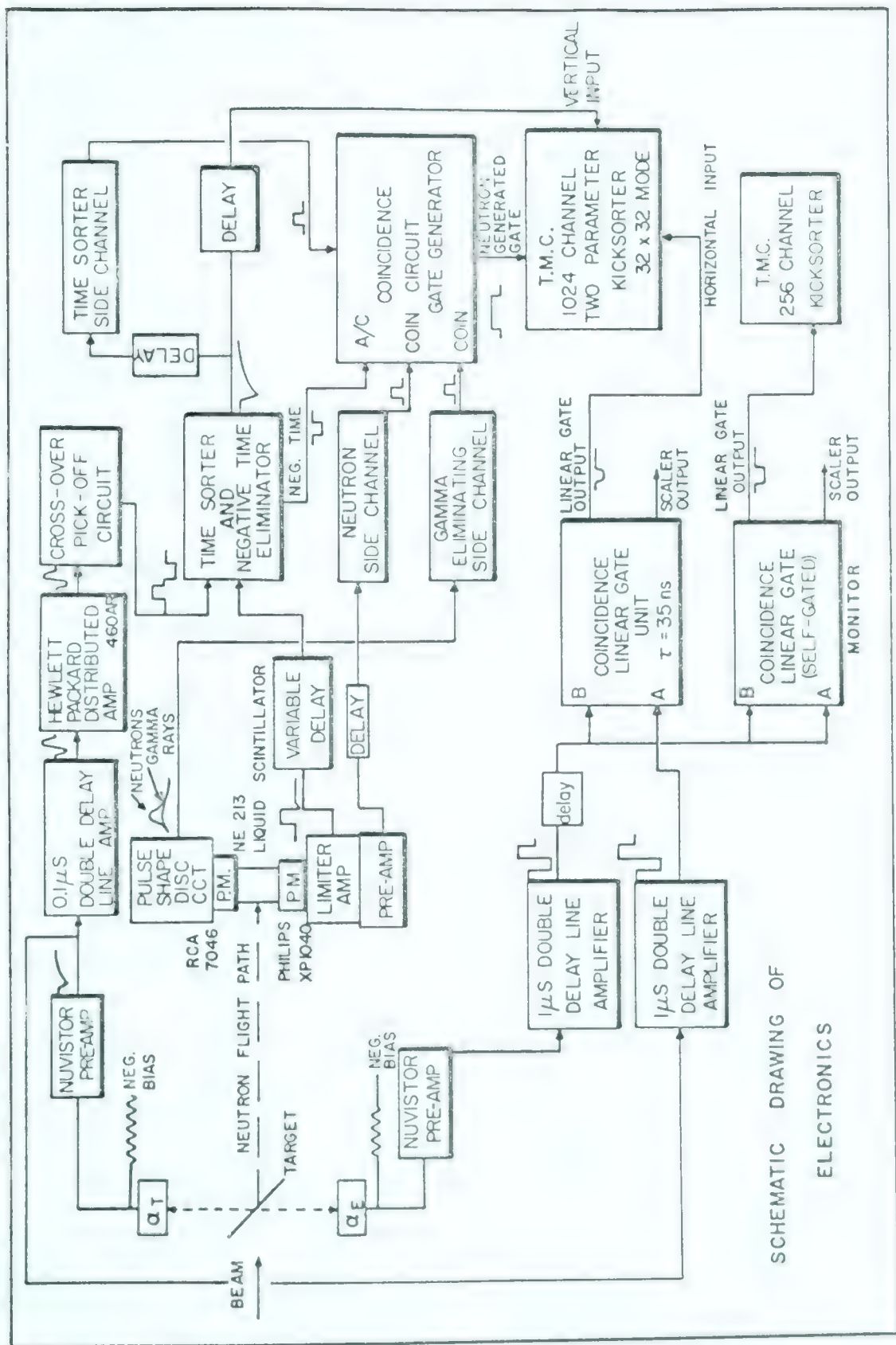


Figure 2-5. The electronics used in the neutron time-of-flight and charged particle spectrometers.

formed in stripping reactions, a solid state detector, located close to the target, is employed, advantage being taken of the precise timing (A1 63) that one can achieve with this type of detector. This is the method used in the present studies of the alpha particle decay of C^{12*} , formed by the $B^{11}(d,n)C^{12*}$ reaction. The fast electronic circuitry required for fast timing with solid state counters is described in detail by Alexander (A1 63) and will be mentioned only briefly in the following discussion of the electronics involved in the neutron spectrometer.

Figure 2-5 shows a block diagram of the complete neutron spectrometer as used in the present experiments, as well as the charged particle spectrometer employing two solid state detectors. The time converter "start" pulses are initiated by the particles detected by the solid state counter labelled α_T , which is a Nuclear Diodes* low resistance, surface barrier device, type PL-2-50-10, operated at a bias of -180 volts. The charge sensitive preamplifier, which employs two 8056 nuvistor triodes in the input stage, integrates the detector pulses, preparing them for double delay line clipping in the following amplifier. The bi-phased output of the amplifier (each phase having a width of 100 nanoseconds) is further amplified by a Hewlett Packard wide band distributed amplifier, model 460AR, before being fed into the cross-over-pick-off circuit. This circuit generates the reference pulses for the time converter, and their shape is shown in the figure. The front edge of the positive portion of the pulse is timed from the

* Nuclear Diodes, Inc., 1640 Deerfield Road, Highland Park, Illinois

"point" (in time) when the input pulse crosses the zero axis. Its width is determined by a 150 nanosecond shorted delay line. The negative going portion of the pulse is retained to keep to a minimum base line shifts which would result from high counting rates. With the exception of the nuvistor tubes used in the preamplifier, and the distributed amplifier, transistors were used throughout in the foregoing circuitry.

The neutrons were detected by NE 213 liquid scintillator^{*} contained in a quartz cell (6 in. x 3 in. x 1 in.) which is viewed by two photomultiplier tubes. The XP 1040 feeds a limiting amplifier with delay line clipping that produces the 150 nanosecond "stop" pulses for the 6BN6 type time-to-amplitude converter. It also drives a linear preamplifier which feeds the neutron side channel formed by a fast amplifier and a single channel pulse height selector. Thus, crude pulse height selection on the neutron spectrum is provided. This side channel is usually set to eliminate those pulses which are too small to produce properly limited pulses for the time converter.

The RCA 7046 photomultiplier feeds a pulse shape discriminating circuit which distinguishes events in the scintillator initiated by neutrons (recoil protons) from those initiated by gamma-rays. The output from this circuit is illustrated in Figure 2-5. The gamma-ray eliminating side channel, consisting of an amplifier (two x5 general purpose, transistorized amplifiers each having a delay of 0.25 microseconds) and a single channel pulse height selector, can be set

* Nuclear Enterprises, Ltd., Winnipeg, Manitoba

to almost completely eliminate random counts resulting from gamma-ray detection in the liquid scintillator.

In addition to requiring the simultaneous occurrence of the positive pulses from the two above mentioned side channels, the kicksorter gate generator requires the absence of pulses from the negative-time-eliminator. This circuit produces a negative pulse whenever, by chance, the "stop" pulse precedes the "start" pulse into the time-to-amplitude converter.

The Resolution of the Neutron Spectrometer

The factors which influence the timing resolution of the spectrometer are listed and discussed by Neilson et al (loc. cit.) and Riley (Ri 62), and need not be repeated here. Suffice it to say that for alpha particles detected in coincidence with gamma radiation, Alexander (Al 63) found the timing resolution to be 2 nanoseconds. He used the $F^{19}(p;\alpha,\gamma)O^{16}$ reaction to produce 2 MeV alpha particles in coincidence with 6.13 MeV gamma radiation.

The energy resolution is related to the timing resolution by the expression $\Delta E/E = 2\Delta t/t$, where E and t are the energy and the flight time of the neutron respectively, and Δt is the time resolution ($\Delta t = 2$ nanoseconds). In the present experiment, the maximum energy resolution could not be realized because the low counting rates limited the flight path to one meter.

VI. The Charged Particle Spectrometer

As mentioned in the introduction to this chapter, two types of

experiment were performed in this investigation of the alpha decay of C^{12} ; one using a single solid state counter and the other using two solid state counters. The complete electronic arrangement for the latter type is shown in Figure 2-5. The detector α_E is used to detect one or two of the alpha particles from the decay of a given state in C^{12} while α_T is used to detect the other remaining particle. α_E is another Nuclear Diodes surface barrier detector, similar to α_T and operated at the same bias. It feeds a nuvistor preamplifier, identical to the one already mentioned, which in turn drives a 1 micro-second double delay line linear amplifier (Go 60a). The signals from this amplifier are gated through a linear gating unit (Go 60b) by pulses obtained from α_T which were amplified in the same way as those from α_E . This unit also uses the zero cross-over technique to determine the delay between the two input pulses A and B. Thus, a resolving time of 35 nanoseconds is realized with this instrument. The linear gate output, which then corresponds to charged particles in coincidence with those detected by the "timing" detector, is fed to the horizontal input of a TMC, 1024 channel, two parameter kick-sorter operating in the 32 x 32 mode. The vertical input of the pulse height analyzer takes its input from the time-to-amplitude converter so that the coincident particle spectra of the horizontal input are sorted out according to neutron groups to which they belong or, in other words, according to the level of excitation of C^{12} from which they originate.

The α_E pulses are self-gated through a second linear gate unit

and fed to a 256 channel TMC kicksorter so that the operation of this detector could be monitored continuously.

When performing the experiments requiring only one solid state detector, α_E and its associated electronics were removed. Pulses from the "timing" detector were self-gated through the linear gate unit and fed to the horizontal input of the two-parameter analyzer. The neutron time spectrum again provided the vertical input. The kicksorter was, of course, as in the former case, gated by the side channels already discussed.

The 256 channel pulse-height analyzer was used to obtain neutron-gated particle spectra, and neutron time-of-flight spectra to compare with that obtained when using the beam pulsing system and isotopically separated B^{11} targets*.

* Obtained from A.E.R.E., Harwell, England

CHAPTER III

EXPERIMENTAL MEASUREMENTS

I. Introduction

This chapter deals with the measurements made in the investigation of the alpha-particle decay of the 12.71 and the 11.83 MeV states in C^{12} formed by the $B^{11}(d,n)C^{12*}$ reaction.

Section II describes preliminary measurements of the neutron time-of-flight spectra obtained using the pulsed beam technique, and an isotopically separated B^{11} target as well as the self-supporting, natural boron target used in the subsequent experiments.

The measurements made using a single solid state detector, from which were obtained the "timing" pulses and the charged particle spectra, are described in section III. One and two parameter data are presented and discussed.

Section IV is concerned with the experiments in which two solid state counters are employed in an effort to detect simultaneously two or all three of the alpha particles from the decay of a given level of C^{12} . Two parameter data which accentuate the 12.71 and the 11.83 MeV levels in C^{12} are presented.

The conclusions that can be drawn from the experimental data are summarized in the final section, V.

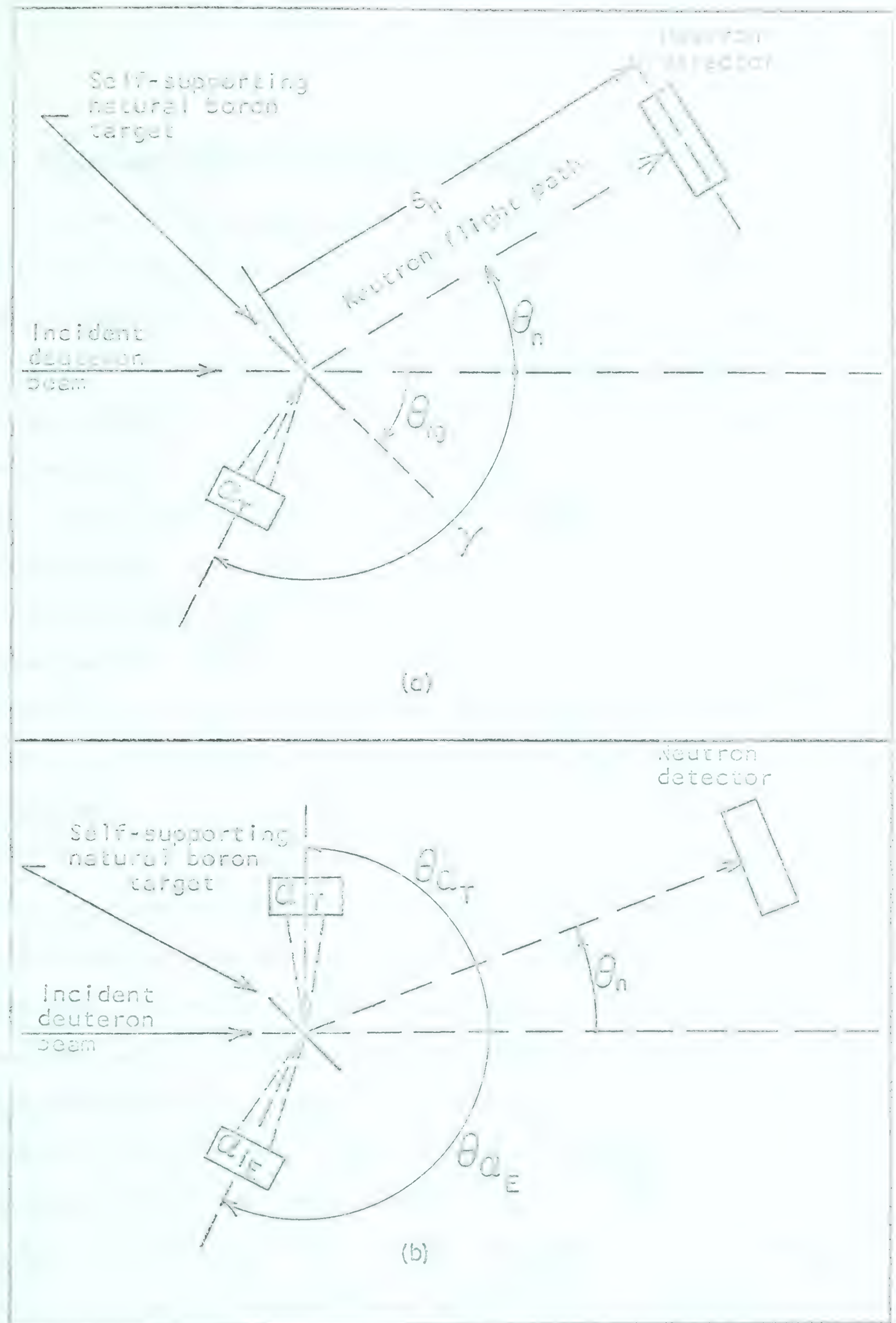


Figure 3-4. Plan view of detector geometries. α_T and α_E are 'Nuclear Diodes' surface barrier detectors.

II. Pulsed Beam Neutron Time-of-Flight Spectra

A time-of-flight spectrum for the neutrons produced in the $B^{11}(d,n)C^{12}$ reaction was obtained using the pulsed beam technique and an isotopically pure B^{11} target*, 1.2 mg/cm^2 thick, to provide a "standard" with which to compare the neutron spectra obtained in the experiments using the self-supporting, natural boron targets, and associated particle timing. Such a spectrum is shown in Figure 3-1. It was taken at a deuteron bombarding energy of 1 MeV with the neutron detector at an angle of 25° with respect to the beam, and 2.8 meters distant from the target. The gamma-ray-eliminating side channel and the neutron side channel were set to cut off pulses produced in the liquid scintillator by a $RdTh$ gamma-ray source. In the case of the neutron side channel, this is equivalent to setting the neutron threshold at about 600 keV. All the levels in C^{12} up to 12.71 MeV excitation, with the exception of the sometimes postulated 10.1 MeV state, are evident in this spectrum. It is also apparent that the levels above the alpha-particle breakup threshold, 7.28 MeV, are riding on what could be a neutron continuum produced, perhaps, by the simultaneous three-body breakup of C^{12} . The three-body breakup (a neutron and two alpha particles) of Be^9 produced by the $B^{11}(d,\alpha)Be^{9*}$ reaction may also contribute to this continuum. On the other hand, the hump in the time spectrum may not be due to a continuum at all, but may be the result of the overlapping

* Separated B^{11} target obtained from A.E.R.E., Harwell, England

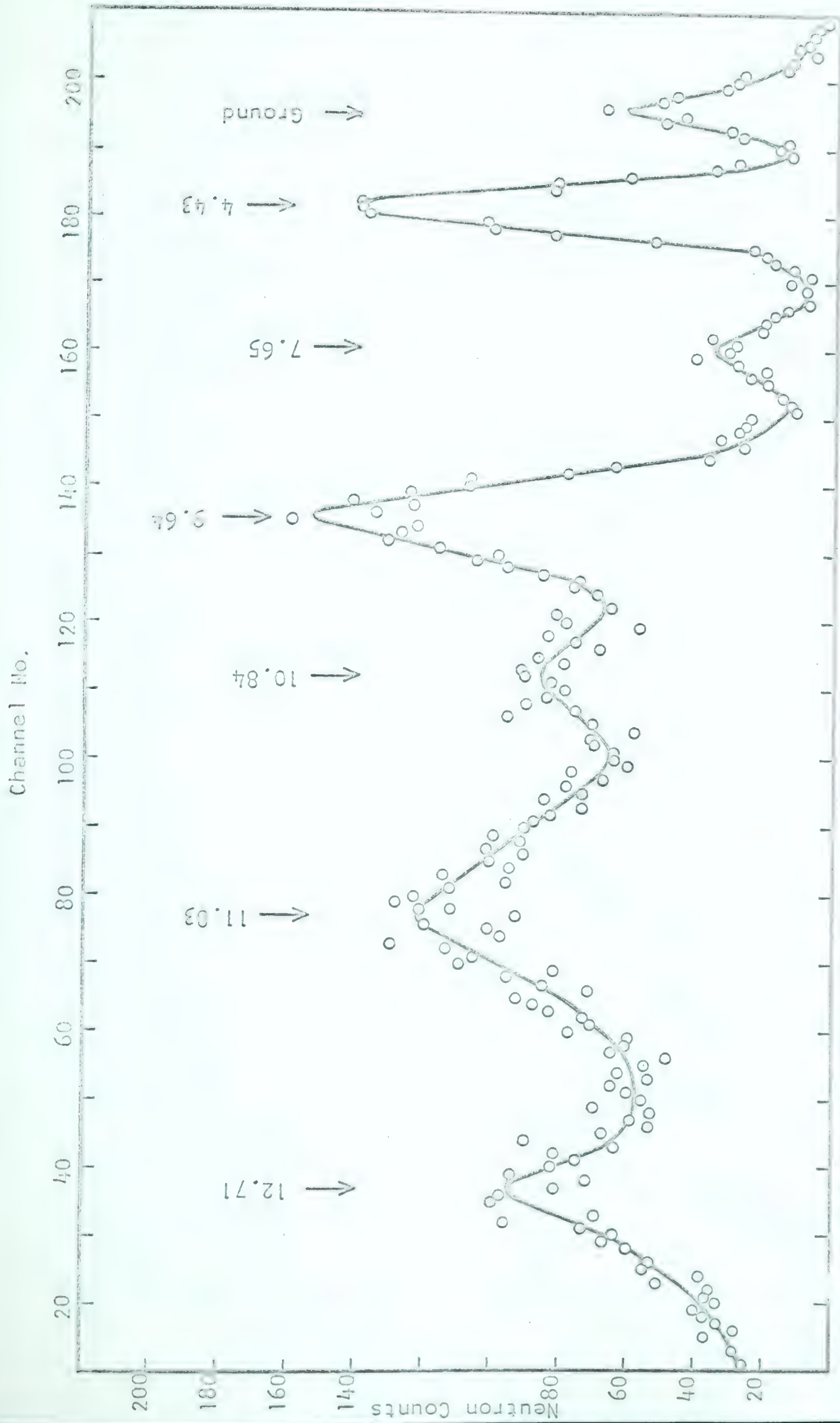


Figure 3-1. A pulsed-beam neutron time-of-flight spectrum of neutrons produced in the $B^{11}(d,n)Cl$ reaction: $E_d = 1$ MeV, $Q_n = 250$, $S_n = 2.8$ meters. Target ≈ 1.2 mg/cm² isotopic B^{11} . Charge ≈ 40 microcoulombs.

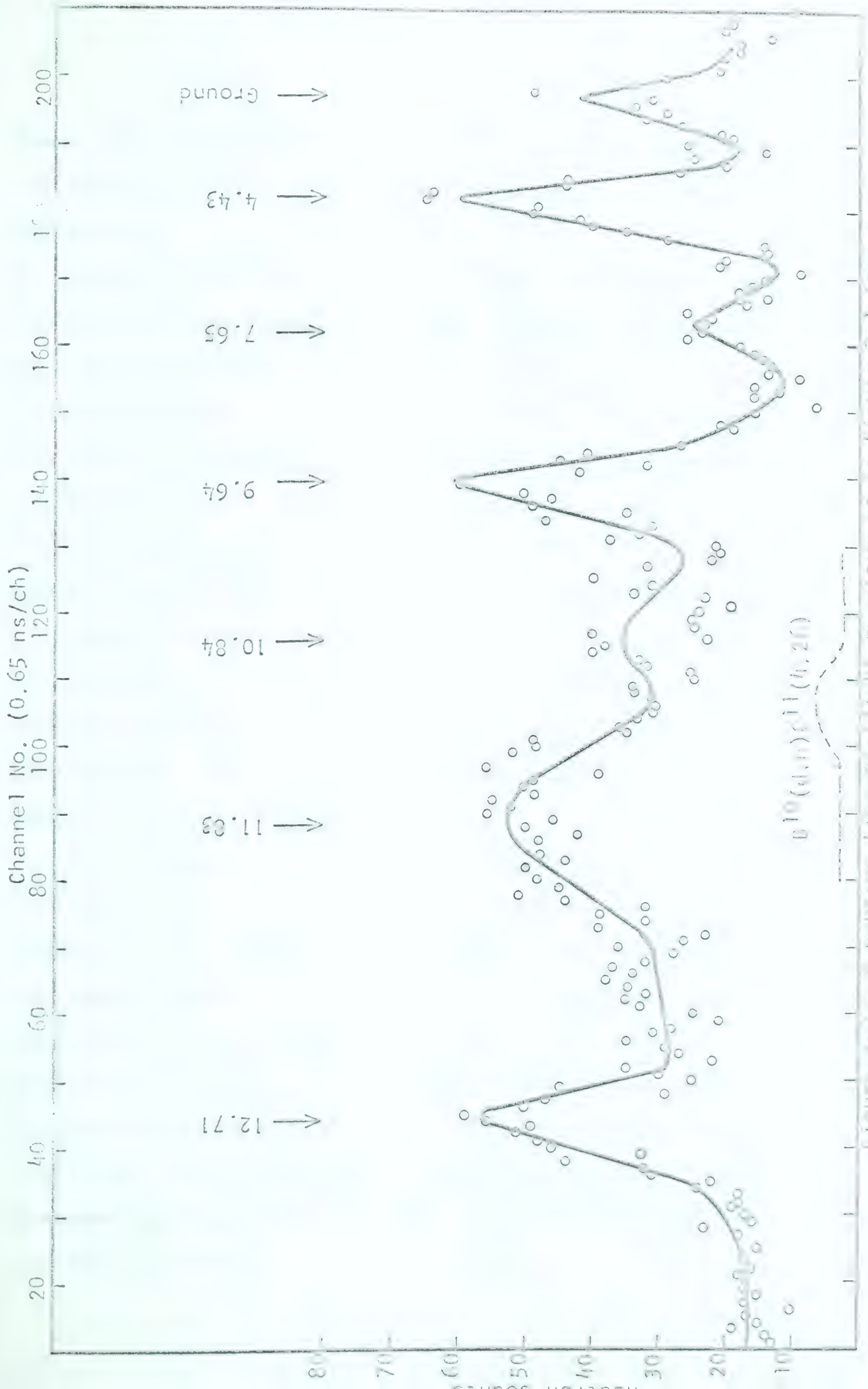


Figure 3: $d^2\sigma/d\Omega dE$ vs Channel No. for various scattering angles. Charge = 300 μC .

levels and a very broad level at 10.1 MeV (Ni 62). It is one of the aims of this research to help establish the origin of the hump in the time spectrum.

Figure 3-2 shows the neutron time-of-flight spectrum taken using the self-supporting, natural boron target. Running conditions were the same as those mentioned above for the separated target except for a slight difference in the gain of the kicksorter. The dashed curve near channel 100 indicates the contribution of the B^{10} in this target to the time spectrum. It was obtained by using a self-supporting B^{10} target, and by applying the appropriate normalizing factors. The effect of the B^{10} on the time spectrum from the natural boron target is completely eliminated when the associated charged particles are used to generate the zero-time reference for the time-to-amplitude converter, unless the solid state detector is able to "see" the C^{11} recoil nucleus. This possibility was removed by using a 10 μ in. nickel foil in front of the detector.

The calibration of the generating voltmeter of the Van de Graaff accelerator was obtained from the measurements made by T.K. Alexander of this laboratory on the thickness of the boron target as described in Chapter II, section IV. The thick target gamma-ray yield from the 873 keV resonance in the $F^{19}(p;\alpha,\gamma)O^{16}$ reaction was measured as a function of the generating voltmeter reading. Curve A of Figure 3-3 shows the yield curve obtained. The resonance energy of 873 keV is seen to correspond to a meter reading of 858 keV. This discrepancy was taken into account when setting the bombarding energy of further experiments.

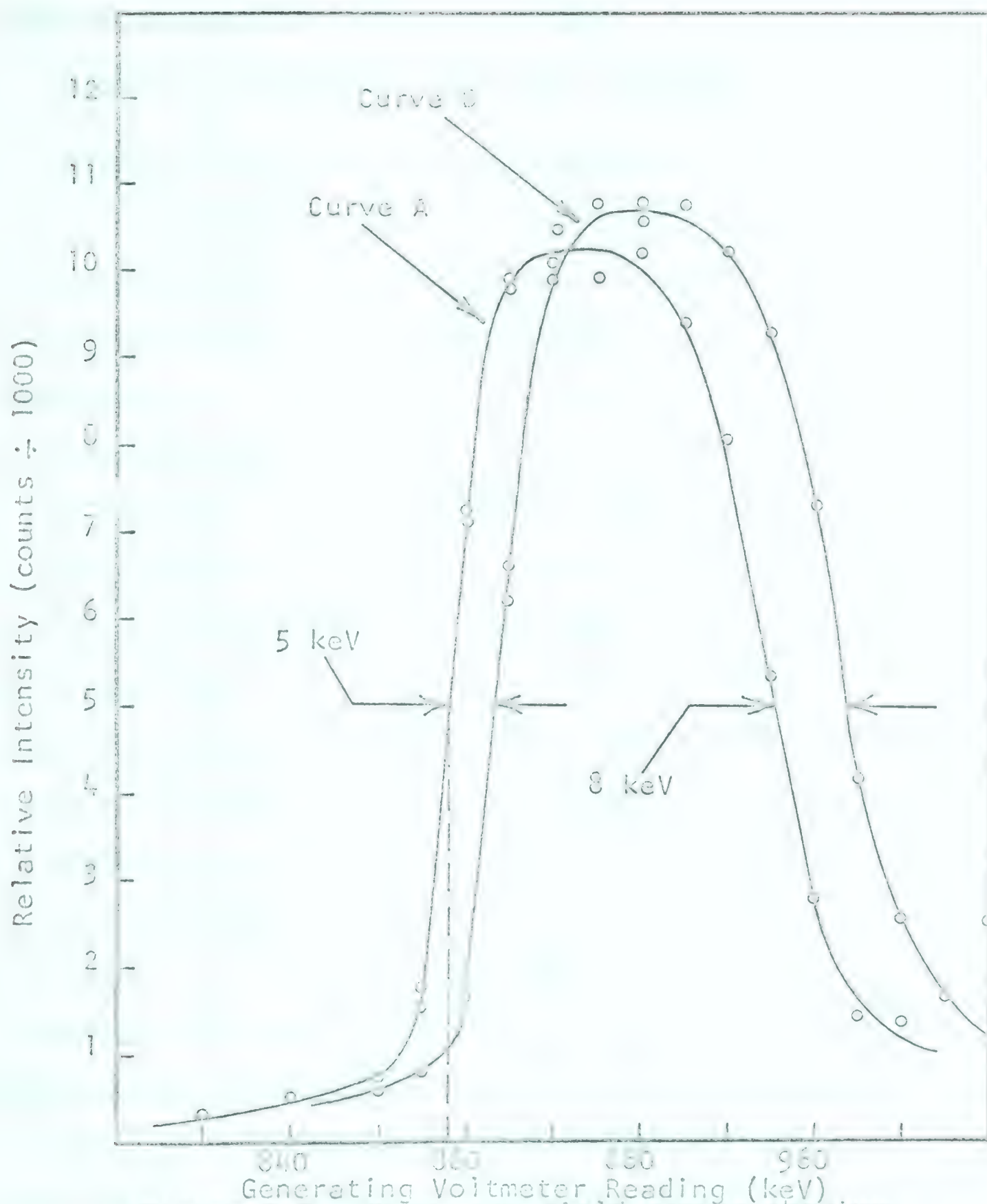


Figure 3-3. Gamma-ray yield curves showing generating voltmeter calibration and self-supporting, Baron target thickness measurement (see text).
(Courtesy of T.K. Alexander)

III. Measurements Using One Solid State Detector

(a) Experimental Arrangement and Running Conditions

The detector geometry used in the experiments employing a single solid state detector to provide both the timing pulses and the charged particle spectra is shown in Figure 3-4a. The angles of the detectors and the target are measured from the direction of the incident beam, and are positive as indicated by the arrows. Because these experiments did not require the best possible resolution from the solid state detector, which was less than one percent with good geometry and an Ortec^{*} low noise amplifying system, a large solid angle was used in an effort to achieve a reasonable (n, α) coincidence rate with a neutron flight path of one meter. The detector, α_T , was shielded by a brass collimator with a 5/16 in. diameter hole in the center, and was positioned 31/32 in. from the beam spot on the target. This corresponds to a solid angle subtended by the detector at the target of 8.2×10^{-2} steradians, or a half angle of 9.1 degrees.

The neutron flight path for most of the runs was 1.15 meters although one time spectrum was taken at 1.42 meters. The counting rate at this distance however was almost intolerably low. The energy resolution at 1.15 meters and a bombarding energy of 1.5 MeV for the lowest energy neutron group of interest (that is, those leading to the 12.71 MeV state in C^{12}) was 8.5 percent.

* Oak Ridge Technical Enterprises, Oak Ridge, Tenn. Model 101-201 low noise preamplifier-amplifier system.

Since the 12.71 and the 11.83 MeV states in C^{12} are of particular interest in this work, the neutron detector was set at angles corresponding to the stripping peaks of these levels. For the 12.71 MeV level, the dueteron stripping peak occurs at approximately 45 degrees in the laboratory system (the angular momentum of the captured proton being almost certainly $\ell_p = 1$), and for the 11.83 MeV level it occurs at an angle of zero degrees, ℓ_p being zero for this case (Sa 62). A series of runs was carried out with the neutron detector at each of these angles.

A deuteron bombarding energy of 1.5 MeV was used throughout in the following experiments, and the beam current was kept below 0.1 μ amp. at which the total counting rate in the solid state detector was of the order of 20,000 per second.

The beam was collected from the target holder and a Faraday cup, both biased at +300 volts to suppress secondary electron emission, and measured by an Elcor^{*} current integrator, model A309A.

(b) Setting-Up Experiments

In order to check that the system was operating properly, some preliminary, particle-gated neutron time-of-flight spectra were obtained. Figure 3-5 shows the spectrum recorded by a 256 channel, TMC pulse-height analyzer for $\gamma = 90^\circ$, $\theta_n = 45^\circ$, and $\theta_{tg} = 45^\circ$; $S_n = 1.15$ meters. The peaks were identified by comparing their separation in time with that calculated from the energies of the

* Elcor Inc., Falls Church, Virginia

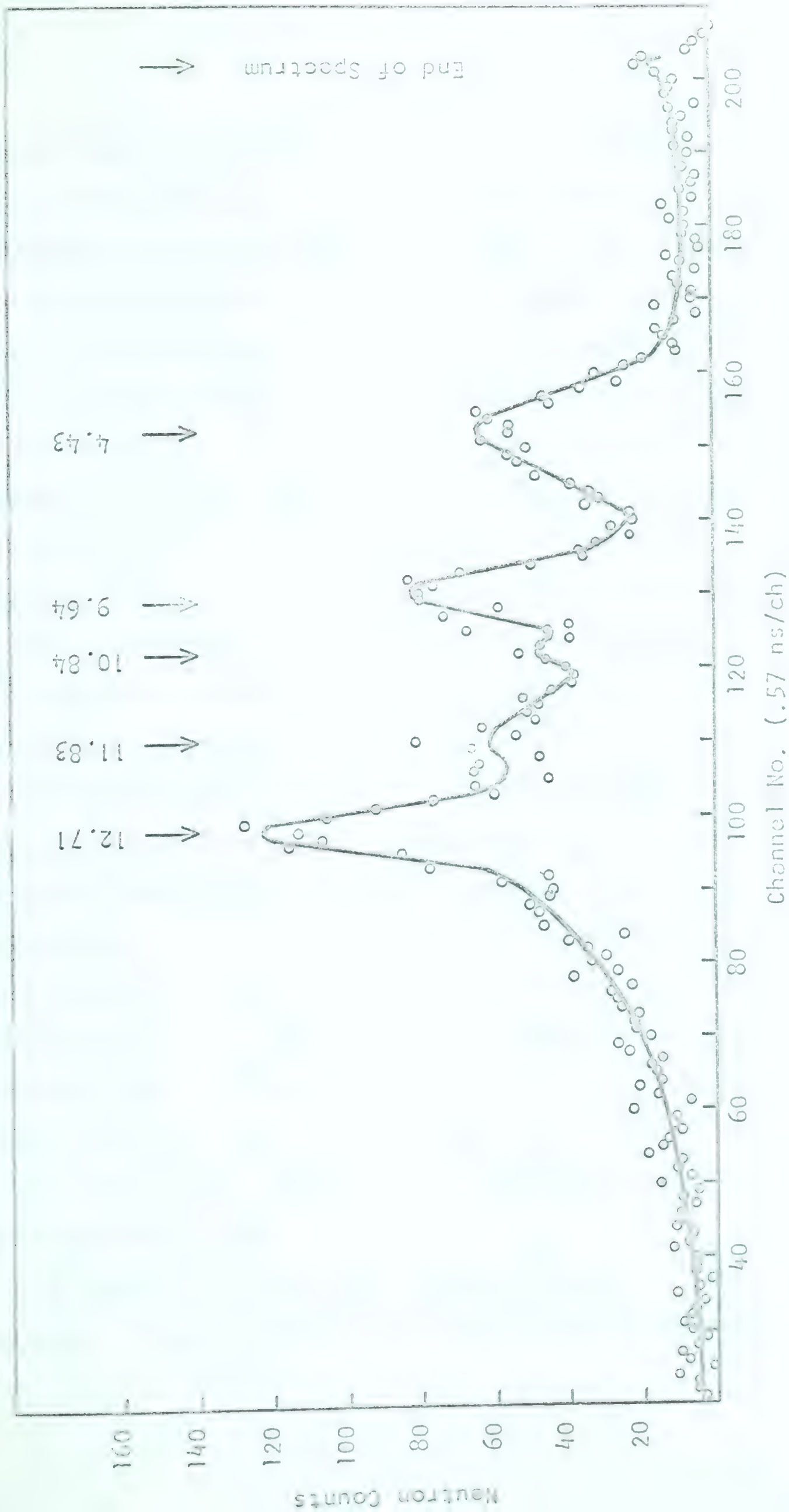


Figure 3-5. Neutron time-of-flight spectrum showing neutron groups leading to the 4.43 , 7.65 , 9.64 , 10.84 , 11.83 , and 12.71 MeV levels of Cl_2 . $S_n = 1.15$ meters, $\gamma = 900$, $E_d = 1.5$ MeV. Charge = 200 microcoulombs.

neutrons leading to the indicated states in C^{12} . The effects of the alpha-particle flight times to the solid state detector on the time separation of the neutron peaks were negligible. The kinematics were calculated using the IBM 1620 computer program Nuclear Reactions I, fully described in Appendix I. The four states in C^{12} above the alpha-particle breakup threshold which appeared in the pulsed beam spectra, Figures 3-1 and 3-2, are also apparent in this spectrum. In addition, however, there is a peak which corresponds to the 4.43 MeV state of C^{12} which is well below the breakup threshold. That this peak was in fact due to the neutrons leading to the 4.43 MeV state, having been "timed" by the recoiling $C^{12}(4.43)$ nuclei was shown in the following way. Time-of-flight spectra were recorded with the solid state detector (1) in line with these recoiling nuclei ($\gamma = 105^\circ$) and (2) at an angle ($\gamma = 80^\circ$) such that they were not within the solid angle of the detector. Figure 3-6 shows the results of this experiment. Curve (1) was obtained with 35 μ c of charge and shows a very prominent peak at the 4.43 position. Curve (2) on the other hand required 110 μ c of charge and there is no evidence at all of a peak at the 4.43 position. That the C^{12} recoil nuclei have little difficulty in getting out of the target was further substantiated by T.K. Alexander of this laboratory who detected them in coincidence with 4.43 MeV gamma radiation (A1 63a).

To eliminate this added complication to the neutron time spectrum, a 10 μ in. nickel foil was placed in front of the solid

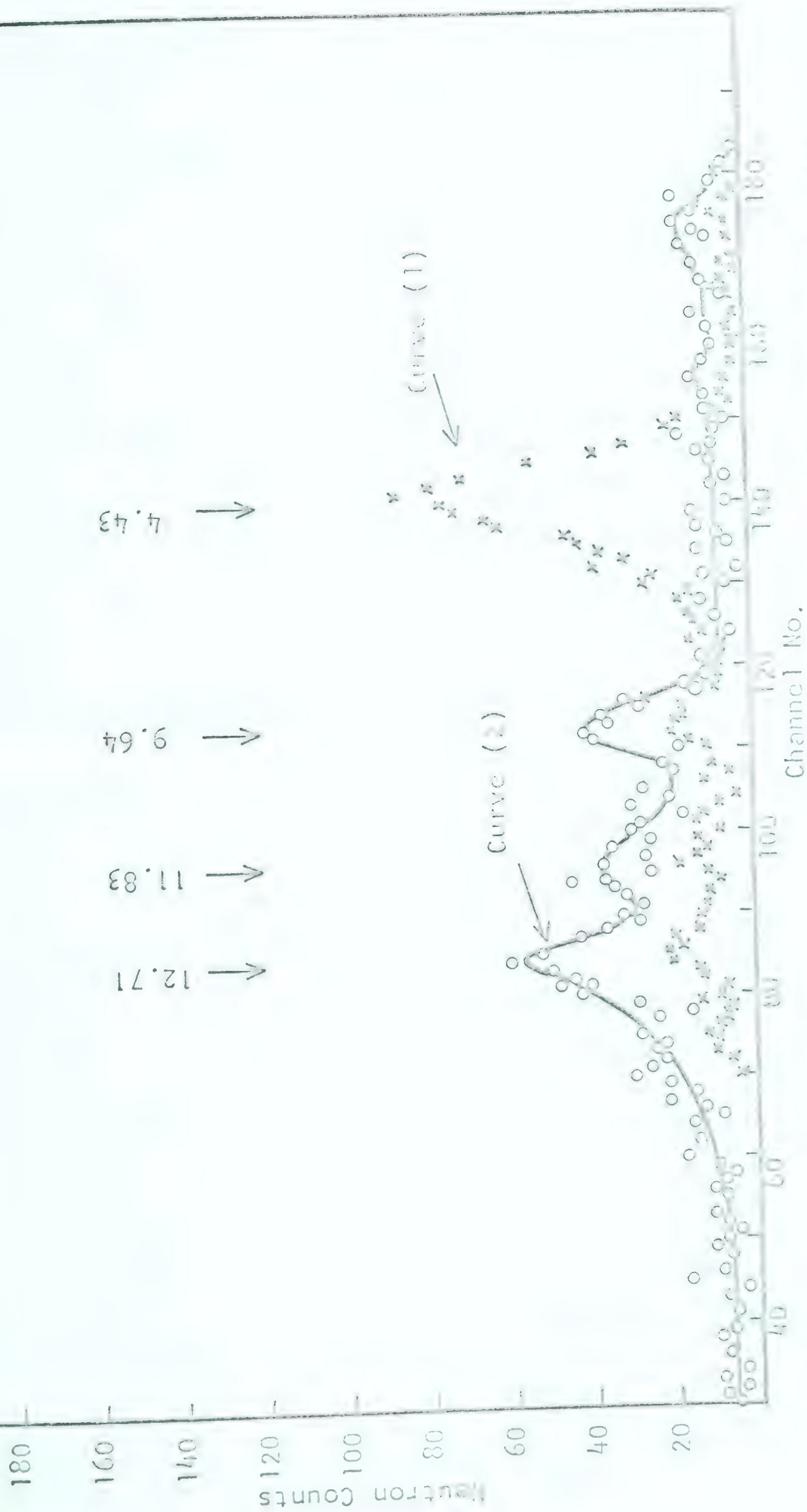


Figure 3-6. Neutron time-of-flight spectra taken with the timing detector (1) in the direction of and (2) unable to "see" the $^{12}(4,43)$ recoiling nuclei, $\theta_n \approx 45^\circ$, $S_H = 1.15$ meters.

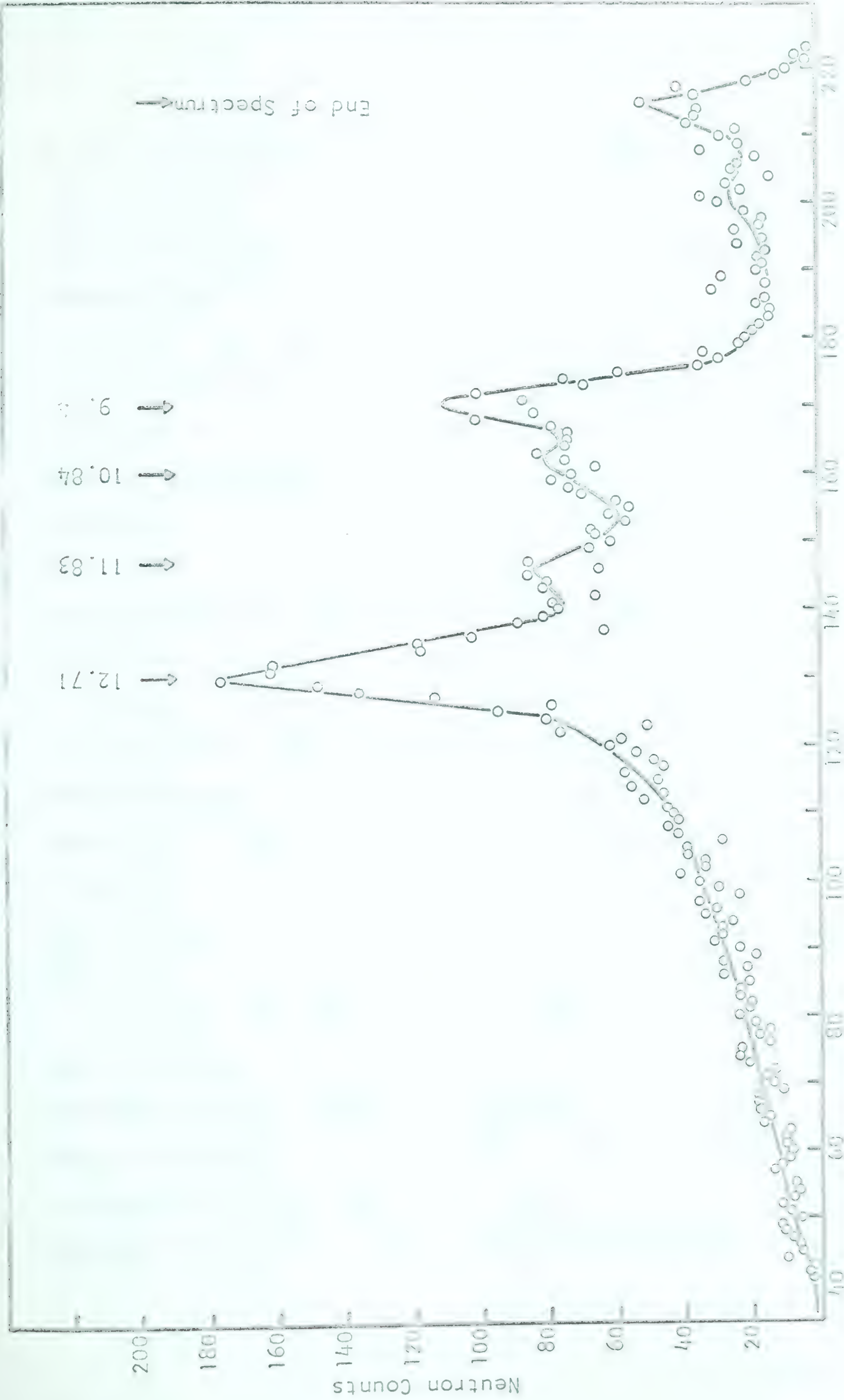
state detector, thus preventing these recoiling heavy nuclei from starting the time converter. Unless otherwise stated, all subsequent runs were made with this foil in place.

Figure 3-7 shows the time-of-flight spectrum taken at a neutron flight path of 1.42 meters; $\gamma = 90^\circ$, $\theta_n = 45^\circ$, and $\theta_{tg} = 45^\circ$. The resolution here is not significantly better than that obtained for $S_n = 1.15$ meters and the running time was over three times as long (Figure 3-5) to obtain the same statistics. The running time for the spectrum of Figure 3-7 was 116 minutes which indicates an almost intolerably low coincidence counting rate. In view of the above, the flight path used in the remaining measurements was set at 1.15 meters.

(c) One-Parameter Measurements at $\theta_n = 45^\circ$

Measurements with the neutron detector at 45° were made in order to accentuate the 12.71 MeV state in C^{12} as mentioned in part (a) of this section. Two 256 channel, TMC pulse-height analyzers were used to simultaneously record the charged-particle-gated neutron time-of-flight spectra and the neutron-gated charged-particle spectra as functions of the solid state detector angle, γ . Both kicksorters were gated by the coincidence circuit gate generator (shown in Figure 2-5) and the side channels were set as previously described.

Spectra were taken for thirteen positions (γ_T) of the solid state detector from 60° to 265° . Direct charged-particle spectra



Channel no. (0.55 ns/ch)

Figure 3-7. Neutron time-of-flight spectrum taken with 10 μ in. nickel foil in front of the timing detector. $\theta_n \approx 45^\circ$, $S_n \approx 1.42$ meters, $\gamma \approx 90^\circ$, $E_d \approx 1.5$ MeV. Charge ≈ 650 μ C.

for each setting were also recorded. Since the variations in the character of these curves from setting to setting were not rapid, only the data for four positions representative of the trends are presented. These data are shown in Figures 3-8 to 3-11 for $\gamma = 90^\circ, 130^\circ, 240^\circ, \text{ and } 265^\circ$. The peaks in the direct spectra were identified with the aid of kinematical calculations made for all deuteron reactions that could occur in the target material and its possible contaminants. The calculations were performed by the University of Alberta IBM 1620 computer using the program, Nuclear Reactions I, described in Appendix I. The Pu^{239} alpha-particle source in the target chamber was used to provide the energy calibration of the kicksorter.

Computer calculations have also been performed to determine the energies of the alpha groups which would result from the decay of the states in C^{12} through the ground and first excited states of Be^8 . These calculations are fully described in Appendix I, under the heading Nuclear Reactions II, and the results for the decay of the 12.71, 11.83, and the 9.64 MeV levels of C^{12} are given there.

If the 12.71 MeV state decays to the ground state of Be^8 , a rather sharp group of alpha particles is expected in the neutron-gated charged-particle spectra. These spectra, of which Figures 3-8a to 3-11a are typical, show no evidence of this group. This is understandable on the basis of the tentative spin-parity assignment of 1^+ (Aj 62) for the 12.71 MeV state, making alpha

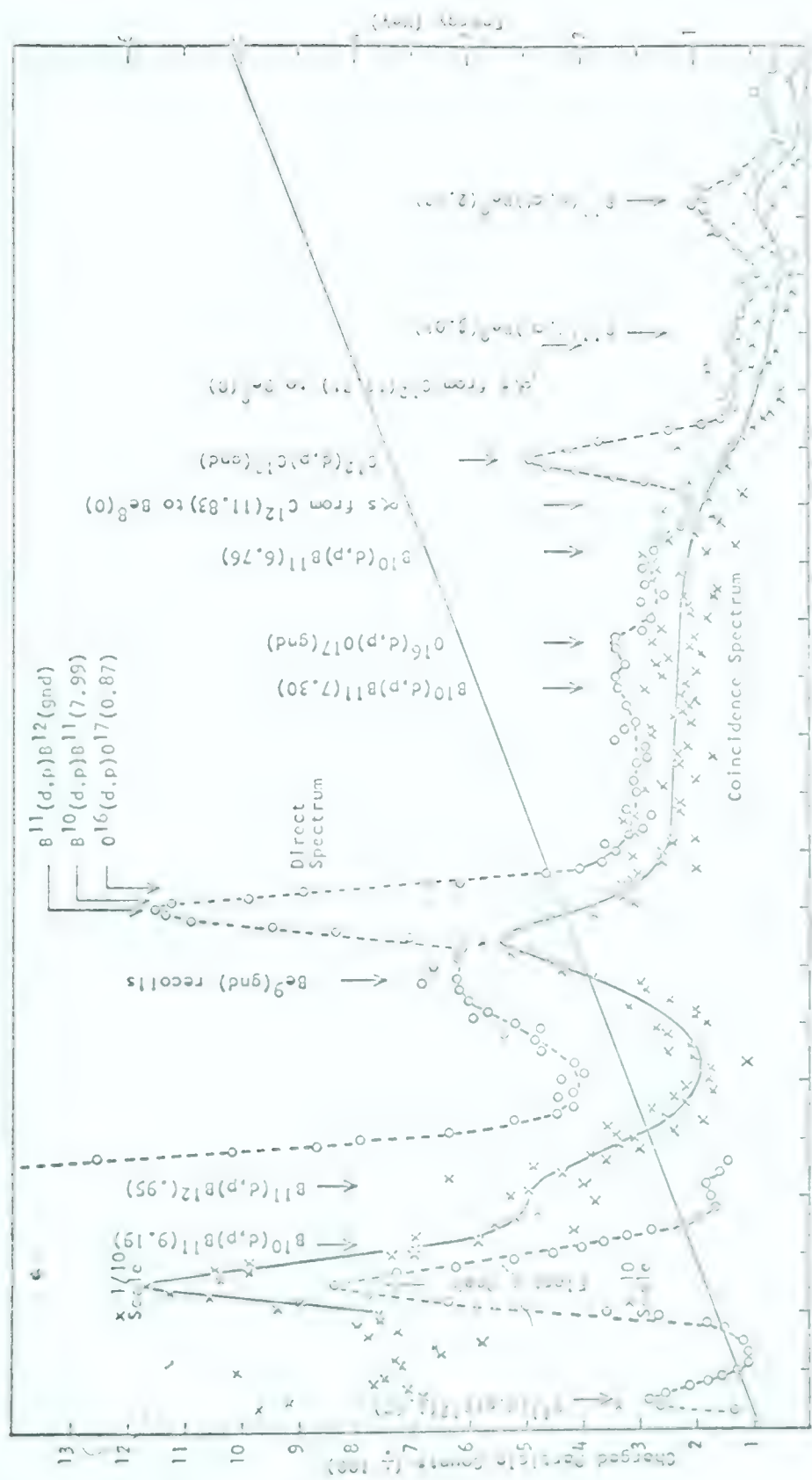


Figure 3-8(a). Neutron-gated and direct charged-particle spectra. $\theta_n = 45^\circ$, $S_0 = 1.15$ meters, $\chi = 900$, $\rho_{ep} = 450$. $E_d = 1.5$ MeV, Charge = 500 microcoulombs.

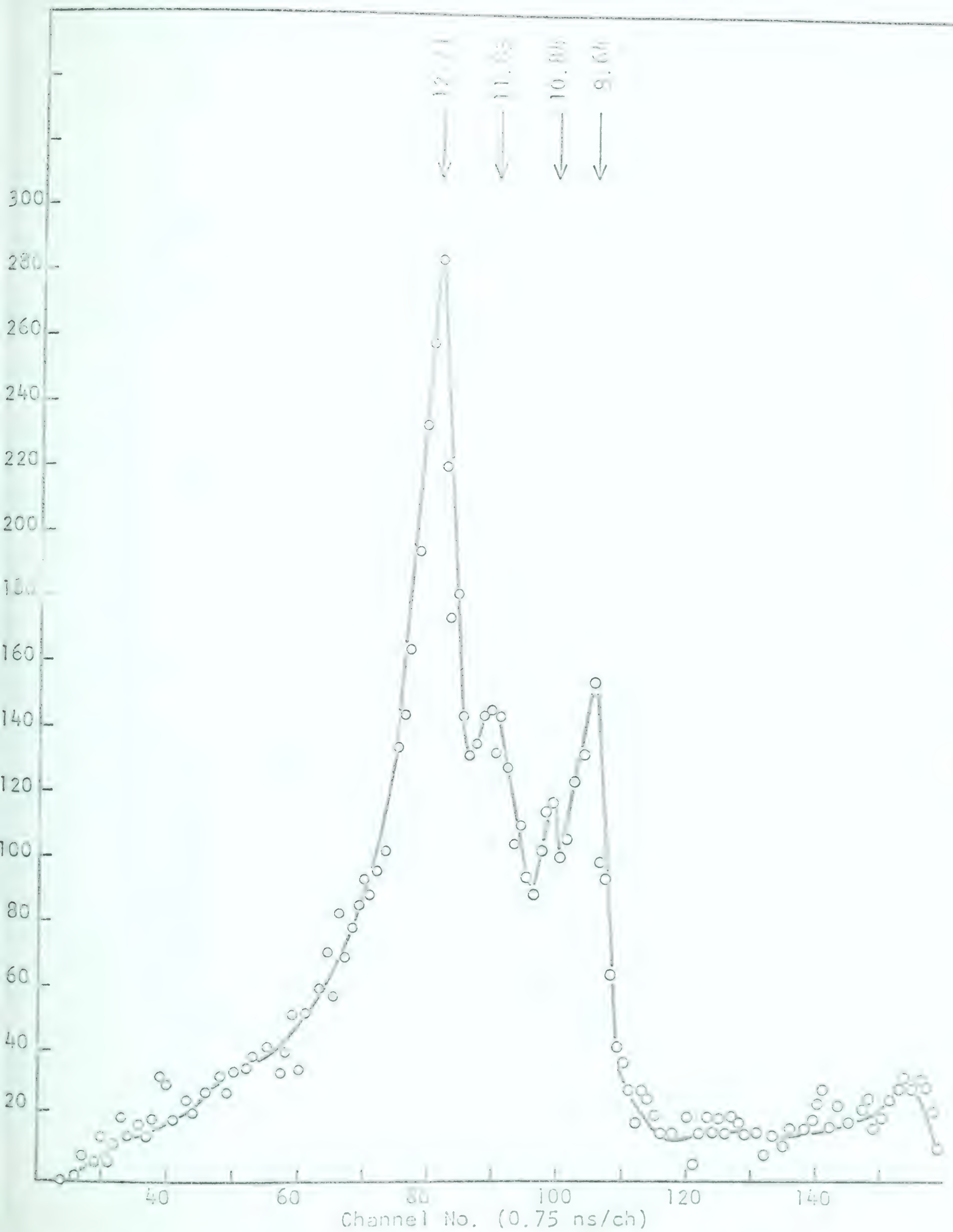


Figure 3-8(b). Neutron time-of-flight spectrum, $\theta_n = 45^\circ$, $S_n = 1.15$ meters, $\gamma = 90^\circ$, $\theta_{tg} = 45^\circ$, $E_d = 1.5$ MeV. Chg. = $500 \mu c$.

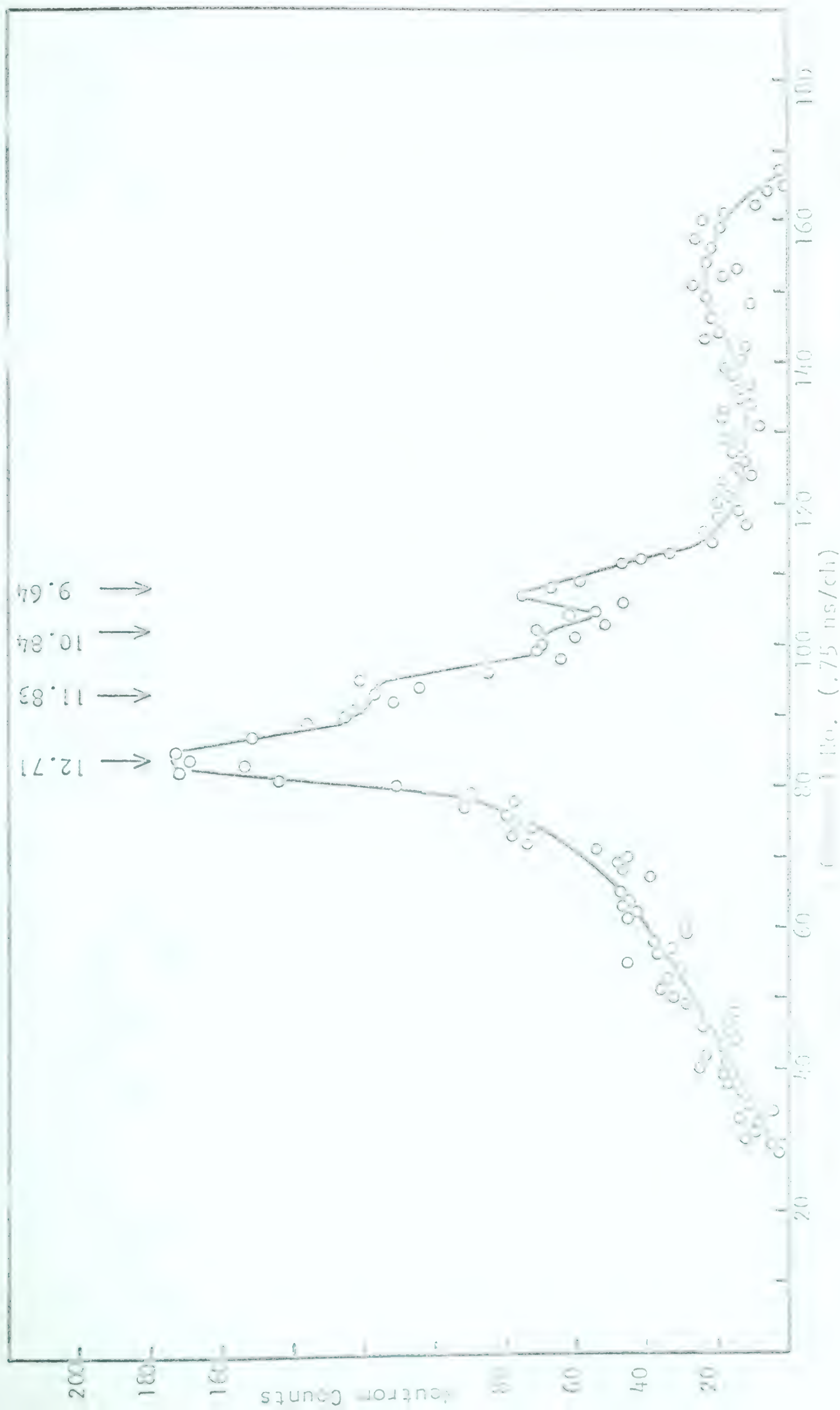


Figure 3-5(b). Neutron time-of-flight spectra. $C_n = 450$, $S_n = 1.15$ meters, $\gamma = 130^\circ$, $C_{tg} = 450$, $F_d = 1.5$ MeV. Charge = 500 microcoulombs.

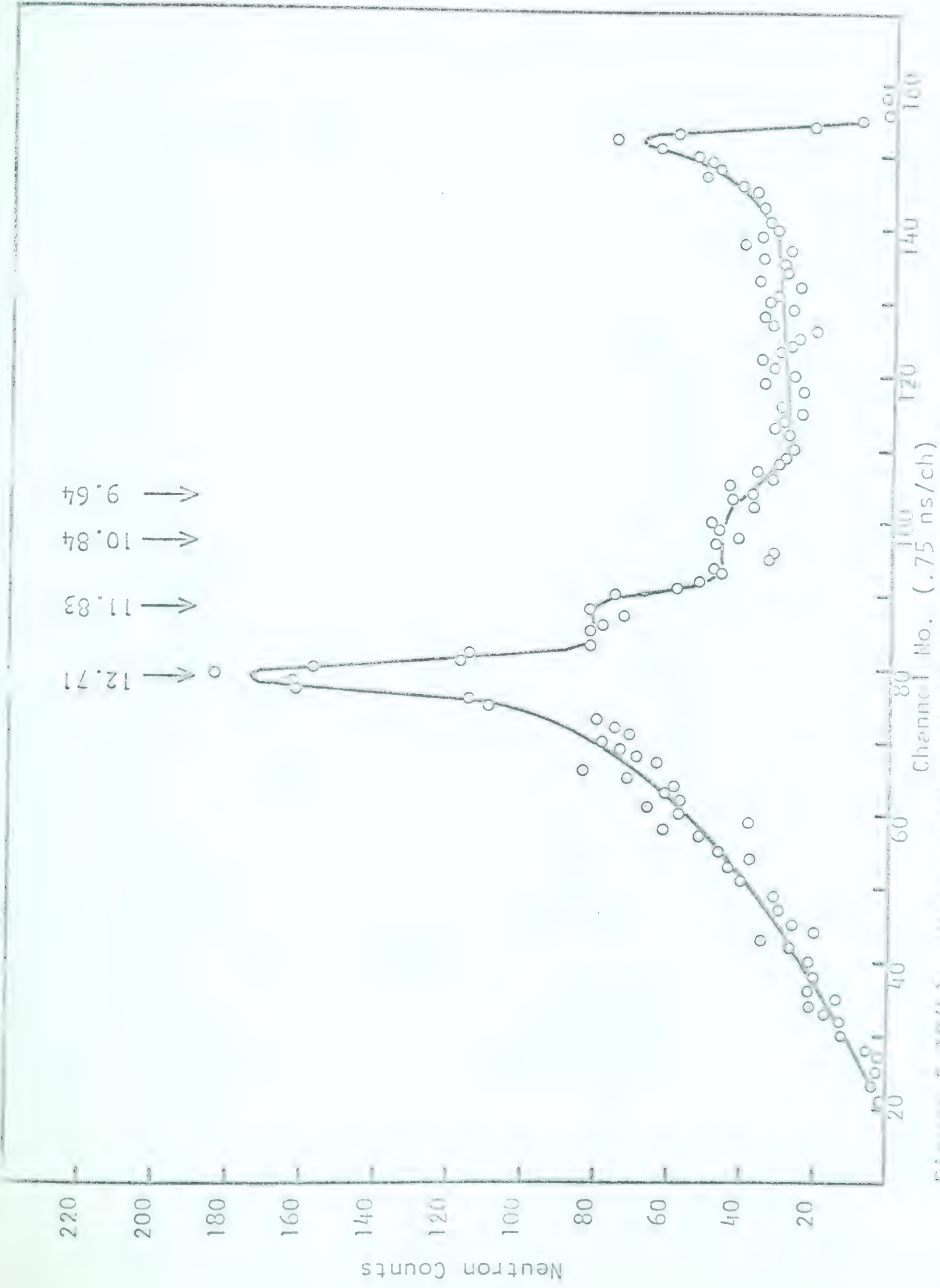


Figure 3-10(b). Neutron time-of-flight spectrum. $\theta_n = 45^\circ$, $S_n = 1.15$ meters, $\gamma = 2400$, $\theta_{tg} = 75^\circ$, $E_d = 1.5$ MeV. Charge = 1200 microcoulombs.

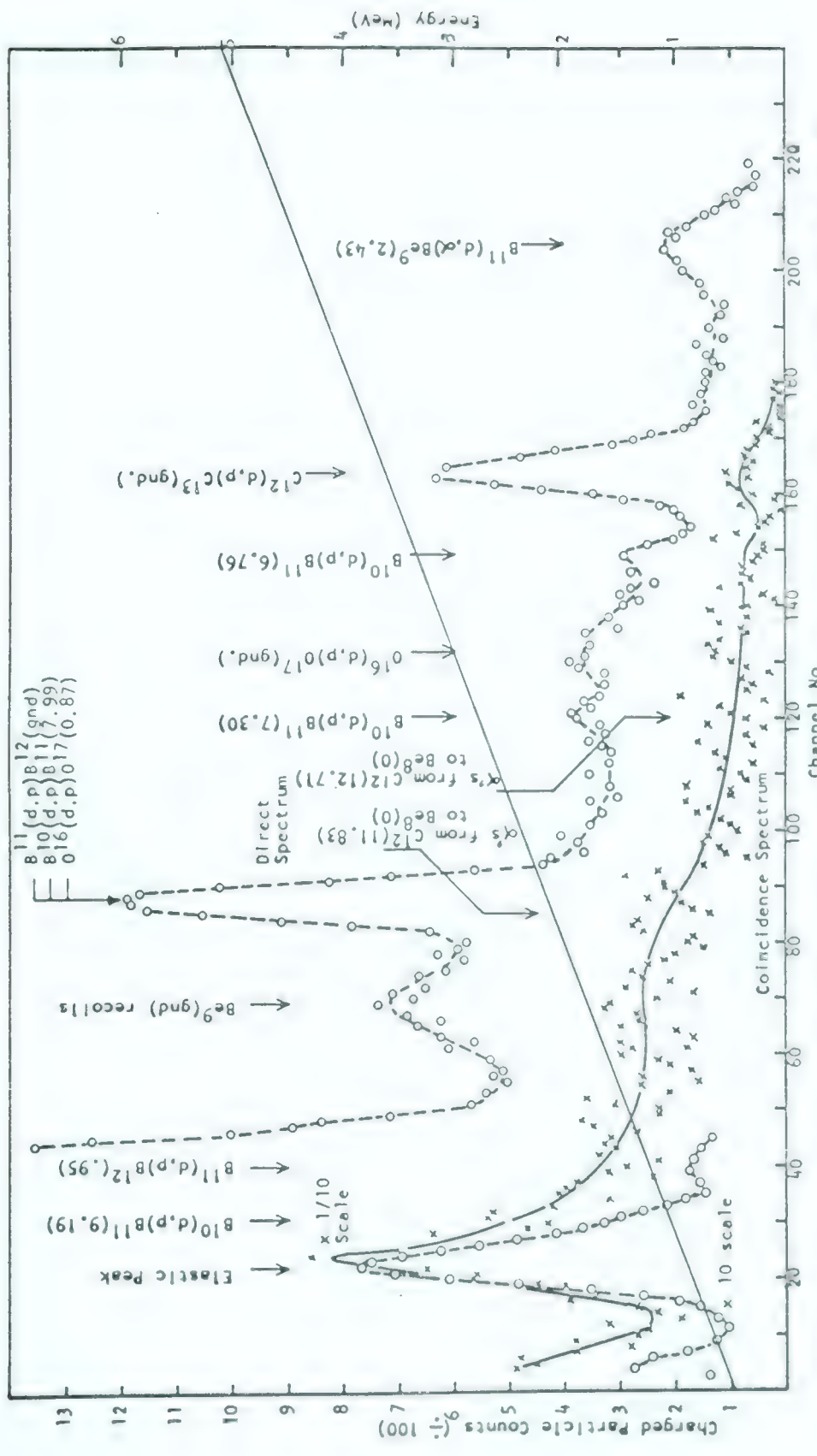


Figure 3-11(a). Neutron-gated and direct charged-particle spectra. $\theta_n = 45^\circ$, $\theta_d = 1.15$ meters, $\chi = 2650$, $\theta_{tg} = 45^\circ$. $E_d \approx 1.5$ MeV. Charge = 500 microcoulombs.

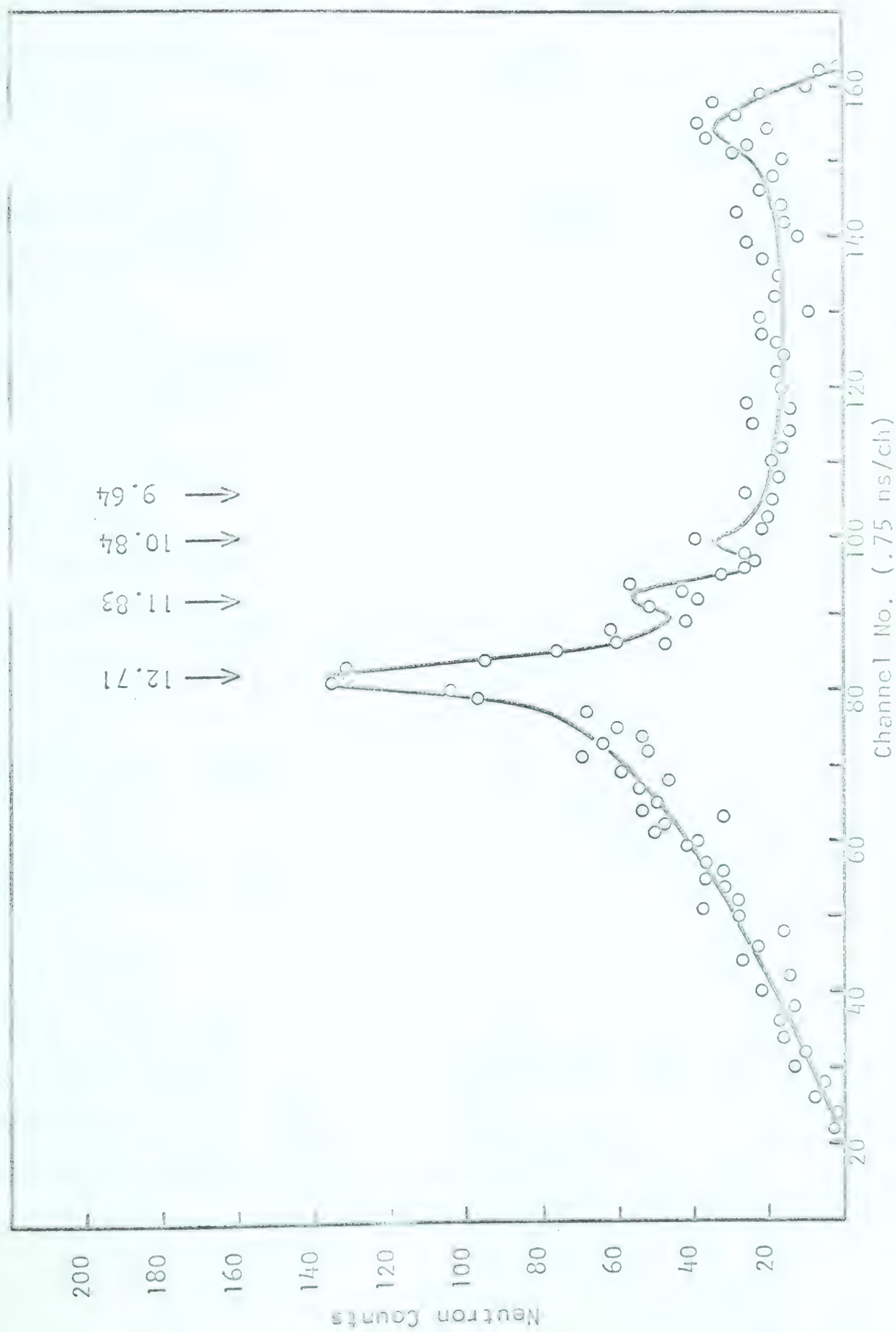


Figure 3-11(b). Neutron time-of-flight spectrum. $\theta_n = 45^\circ$, $S_n = 1.15$ meters, $\gamma = 2650$, $\theta_{tg} = 45^\circ$, $E_d = 1.5$ MeV. Charge = 500 microcoulombs.

decay to the 0^+ ground state of Be^8 forbidden. Hence, these data provide very strong support for the 1^+ assignment for this level of C^{12} .

Also, these spectra do not show peaks (where indicated in the figures) which would correspond to the alpha group from the 11.83 MeV level of C^{12} leading to the Be^8 ground state. Thus, if the 11.83 state does decay sequentially through Be^8 , it would seem that it does so predominantly via the 2.9 MeV state. There is no selection rule forbidding the unobserved transition since there is little doubt about the 1^- spin-parity assignment for this level of C^{12} (Sa 62).

The two peaks which occur near the end of the charged-particle coincidence spectra, as for example in Figure 3-9a at 3.4 and 4.35 MeV, are attributed to alpha particles from the $\text{B}^{11}(\text{d},\alpha)\text{Be}^{9*}$ (3.04 and 2.43 MeV) reactions respectively in coincidence with neutrons from the subsequent breakup of the Be^9 states. The 3.4 MeV peak may also have contributions from random coincidences between neutrons and protons from the $\text{C}^{12}(\text{d},\text{p})\text{C}^{13}(\text{gnd})$ reaction.

With reference to Figure 3-8a, the peak at 1 MeV and the hump at 1.25 MeV are due to random coincidences between neutrons and scattered deuterons and the very intense proton group from the $\text{B}^{11}(\text{d},\text{p})\text{B}^{12}(0.95)$ reaction respectively. The peak near 2 MeV consists, in part, of random events involving protons from the $\text{B}^{11}(\text{d},\text{p})\text{B}^{12}(\text{gnd})$, $\text{B}^{10}(\text{d},\text{p})\text{B}^{11}(7.99)$, and $\text{O}^{16}(\text{d},\text{p})\text{O}^{17}(0.87)$

reactions. It also contains alpha particles from the decay of the 9.64 MeV state of C^{12} to the ground state of Be^8 , a well established transition (see Chapter I), and those from the decay of the 12.71 MeV state of C^{12} to the 2.9 MeV state of Be^8 , assuming that this transition takes place. The valley at 1.5 MeV fills in, and the peak at 2 MeV decreases in height as γ increases throughout its range; this is in keeping with the kinematic shift in energy of the alpha-particle groups from the 9.64 and 12.71 MeV levels of C^{12} . The overlapping of these two alpha-particle groups points out the need for a two parameter analysis of this case to sort out the charged-particle spectra according to the neutron groups with which they are associated or, in other words, according to the levels of C^{12} from which they originate. Such measurements were carried out and will be reported in part (d) of this section.

Figures 3-8b, 9b, 10b, and 11b show the charged-particle-gated neutron time-of-flight spectra corresponding to the charged-particle spectra discussed above. One of the features of these curves is the variation in the intensity of the neutrons leading to the 12.71 MeV state of C^{12} with the position of the solid state detector. It is clear that there are more alpha particles originating from this state on the side of the deuteron beam opposite the neutron detector in the general direction of the recoiling C^{12} nuclei. Now if this level decays by a direct three-body process, there would be a high probability of equal sharing of the disintegration energy between the three particles as indicated from the three-body distributions

shown in Figure 3-15. The total disintegration energy being 5.43 MeV, this means that each particle would have about 1.81 MeV of energy. Therefore, the recoiling C^{12} nuclei, which have an energy of only 0.134 MeV (at an angle of 60° from the deuteron beam), would be expected to have little or no effect on the number of alpha particles emitted in a given direction in the reaction plane, and hence the angular distribution should be almost isotropic.

On the other hand, if the decay of this state proceeds through Be^8 (in particular, the 2.9 MeV level of Be^8), it can be argued that one should expect the angular distribution of the alpha particles to be peaked about the center of mass direction of the recoiling C^{12} nuclei. Assuming isotropic breakup of the Be^8 state formed (2.9 MeV), this angular distribution would be reflected in the neutron time-of-flight spectra.

The angular distribution of the alpha particles from the decay of the 12.71 MeV state to the 2.9 MeV state of Be^8 can be calculated by assuming that the carbon level is an intermediate stage of the reaction, $B^{11}(p,\alpha)Be^8(2.9)$. This assumption is reasonably well justified because the stripping pattern for the neutrons leading to the 12.71 MeV state is predominantly Butler with the angular momentum of the captured proton equal to one ($\ell_p = 1$) (Sa 62). The angular distribution will then be symmetrical about the direction of the captured proton; that is, about the direction of the recoiling C^{12} nucleus (To 61). Taking the ground state of B^{11} as having a J^π of $3/2^-$, there are two possible

values of the incoming-channel spin; $S_1 = 1$ and $S_1 = 2$. The incoming orbital momentum is $\ell_p = 1$ (Sa 62), the intermediate C^{12} state is taken as a 1^+ level, and the out-going channel spin and the out-going orbital momentum are both 2, based on the 2^+ assignment of the Be^8 (2.9) state. From the tables of Sharp et al (Sh 54), and using the above angular momentum quantum numbers, the angular distribution functions were found to be, for $S_1 = 1$,

$$W_1(\psi) \sim 1 + \frac{1}{2} P_2(\cos\psi),$$

and for $S_1 = 2$,

$$W_2(\psi) \sim 1 - \frac{1}{10} P_2(\cos\psi),$$

where ψ is the angle of emission of the alpha particles in the coordinate system in which the C^{12} is at rest. $P_2(\cos\psi)$ is the usual Legendre polynomial of the second degree. These functions are shown in Figure 3-12a plotted against ψ and the corresponding laboratory angle γ . Also shown in the figure are experimental points representing the peak heights of the $C^{12}(12.71)$ neutron group in the thirteen measured particle-gated time-of-flight spectra. These points have been normalized to 500 μc of charge, to a target angle of 45° , and to 1.5 at $\gamma = 90^\circ$; they have also been corrected for background and for the solid angle transformation from the laboratory system to the center of mass system of the C^{12} nucleus (see Appendix I, Nuclear Reactions I, where the

kinematics have been described in some detail). The shape of the experimental distribution compares reasonably well with W_1 . The shift in the symmetry axis, approximately 40° in the center of mass system, from that defined by the recoiling C^{12} nuclei could be a manifestation of the distortion effects taking place in the formation of the carbon state (To 61). That such effects are present in this case is indicated by the rise in the neutron angular distribution at back angles (Sa 62).

On the basis of the agreement of experimental distribution of Figure 3-12a with W_1 and not with an isotropic distribution (which would be a straight, horizontal line in the figure), it would appear more likely than not that the 12.71 MeV state of C^{12} decays sequentially through the 2.9 MeV level of Be^8 . It would also seem that $S_1 = 1$ is the dominant incoming channel spin for the reaction.

Because the peaks in the time-of-flight spectra of the group corresponding to the 11.83 MeV state in C^{12} are not very prominent, an angular distribution based on the peak heights would hardly be justified. Nevertheless, the experimental points, normalized and corrected for solid angle, are presented in Figure 3-12b in order to get a crude idea of the distribution of alpha particles originating from the 11.83 MeV state. The predicted distributions for the alpha particles leading to both the ground and first excited states of Be^8 are isotropic, assuming that pure Butler stripping is the dominant process in the formation of the carbon state, with

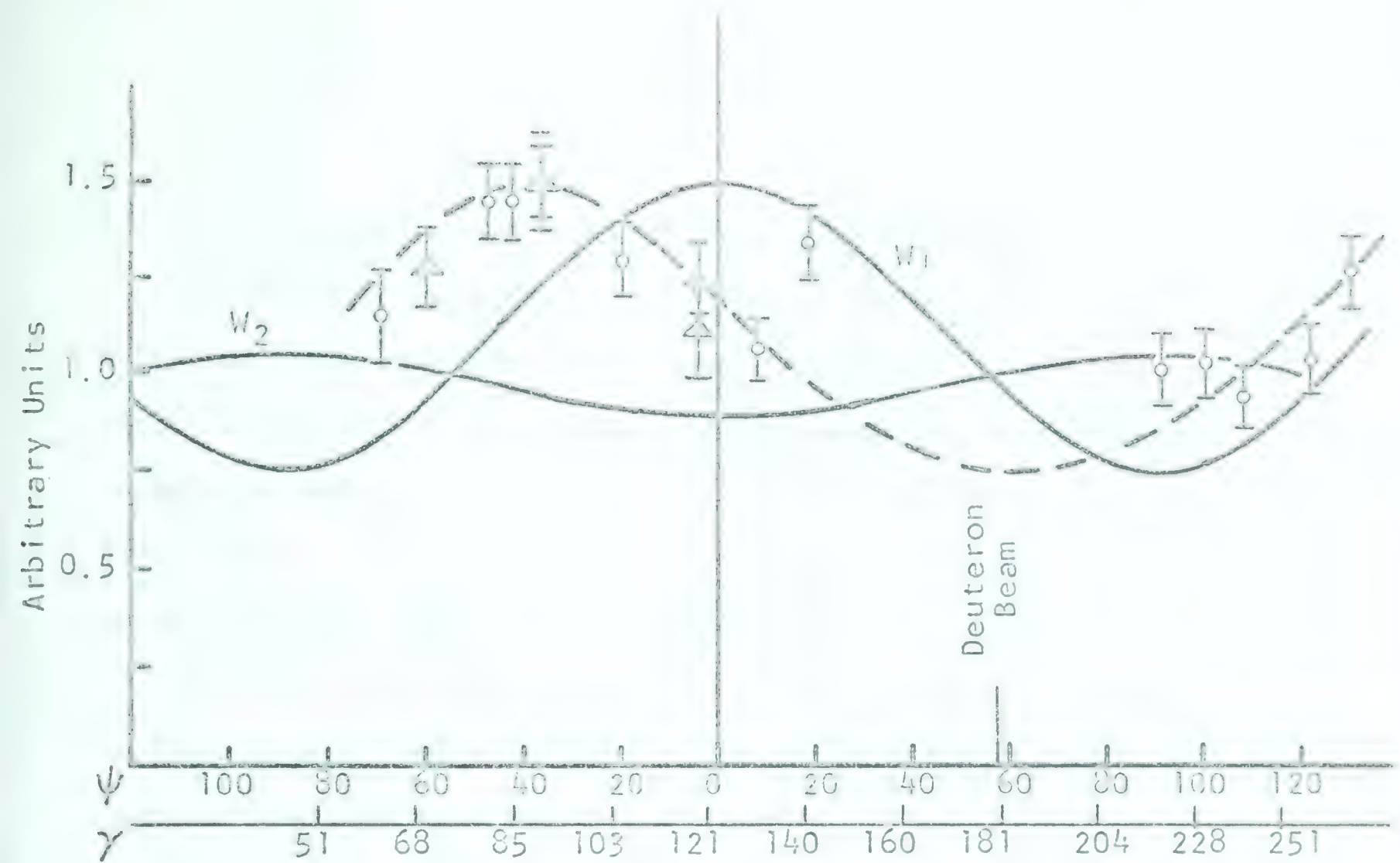


Figure 3-12(a). Angular distribution of alpha particles from $C^{12}(12.71)$ to $Be^8(2.9)$.

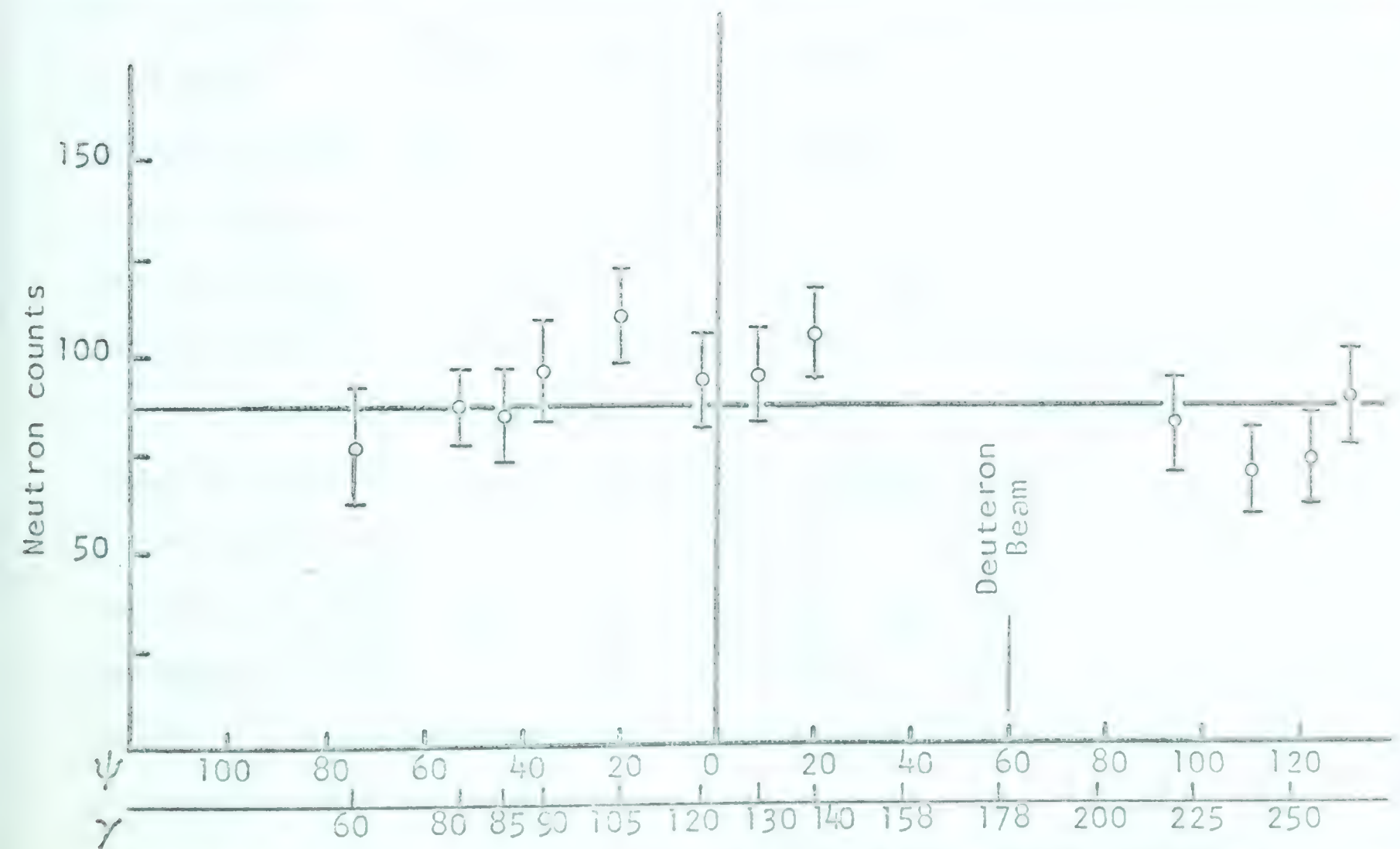


Figure 3-12(b). Experimental angular distribution of alpha particles from $C^{12}(11.83)$ to $Be^8(2.9)$.

$\ell_p = 0$ (Sa 62), and that the Be^8 is formed by a $\text{B}^{11}(\text{p}, \alpha)\text{Be}^8$ reaction.

Two of the three three-body energy distribution functions for this case, shown in Figure 3-18 (curves a and b) and discussed in detail in part (f) of this section, predict equal sharing of the disintegration energy. On this basis, a three-body breakup of this state would also be isotropic since the energy of the recoiling C^{12} nuclei (.153 MeV) would not significantly alter the distribution.

The very crude experimental distribution of Figure 3-12b could be interpreted as being isotropic. This only confirms what would be expected irrespective of the mode of decay.

The experimental angular distribution of the alpha particles from the 9.64 MeV state of C^{12} to the ground state of Be^8 is shown in Figure 3-13. These points (open circles) correspond to the peak heights of the $\text{C}^{12}(9.64)$ neutron group in the neutron time-of-flight spectra, corrected as before for background and the solid angle transformation. They are normalized to 1.58 at $\gamma = 90^\circ$, and are connected by the dot-dashed curve for visual aid. The three points enclosed in triangles were obtained from two-parameter data and will be discussed in part (d) of this section. The solid curves shown in Figure 3-13 are the distributions predicted assuming a proton capture reaction in the direction of the $\text{C}^{12}(9.64)$ recoil, and were determined using the following angular momentum and parity assignments (Aj 62): B^{11} , $3/2^-$; $\ell_p = 2$ (Sa 62); $\text{C}^{12}(9.64)$, 3^- ; $\text{Be}^8(0)$, 0^+ . W_1 is the distribution for the incoming channel spin, S_1 , equal to one, and is given by

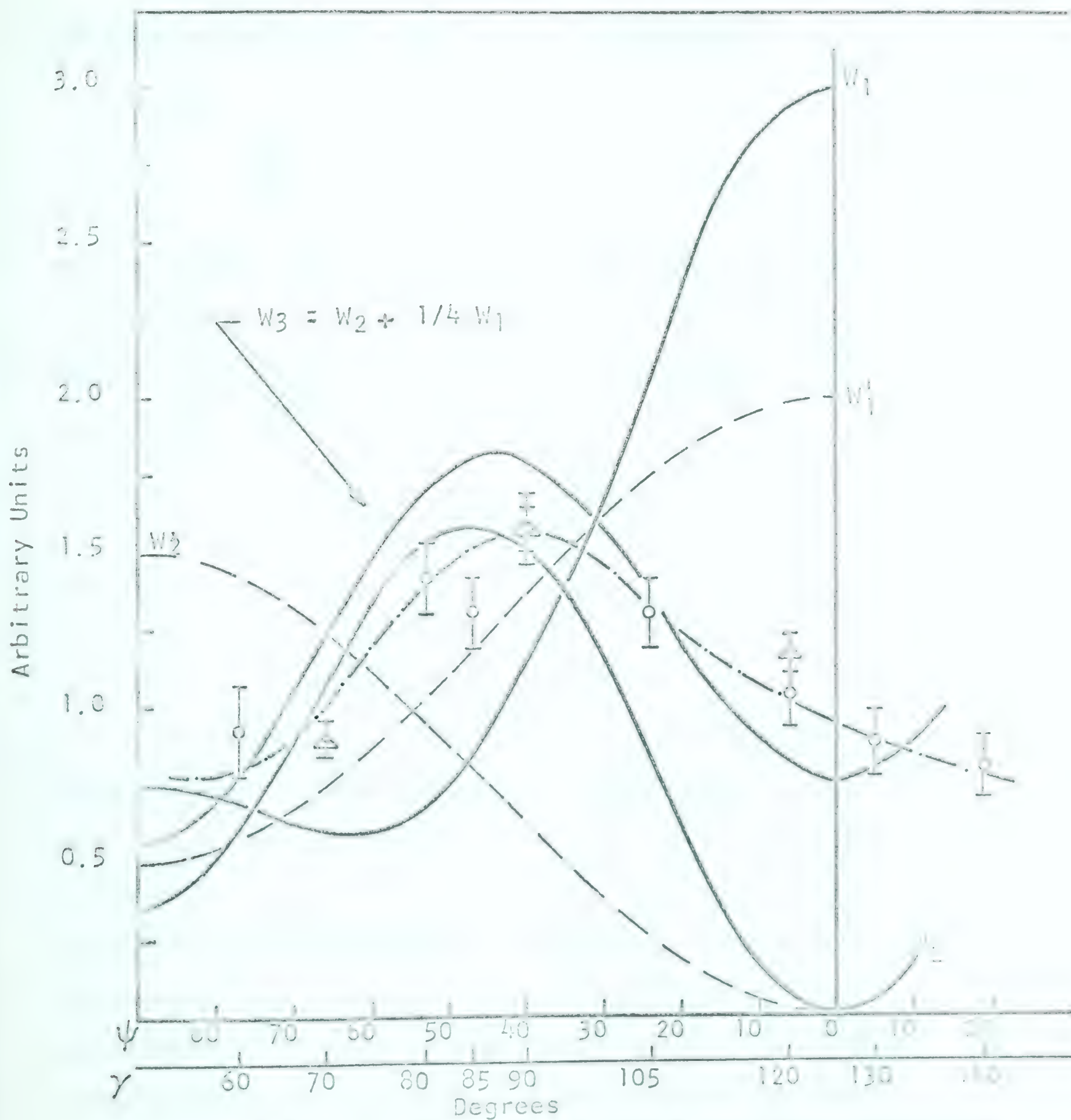


Figure 3-13. Angular distributions for alpha particles from $\text{Cl}^{35}(9.64)$ to $\text{Be}^8(0)$.

$$W_1(\psi) \sim 1 + 8/7 P_2(\cos\psi) + 6/7 P_4(\cos\psi).$$

The distribution for the other possible incoming channel spin, $S_1 = 2$, is

$$W_2(\psi) \sim 1 + 2/7 P_2(\cos\psi) - 9/7 P_4(\cos\psi).$$

W_3 is $W_2 + .25W_1$. W'_1 and W'_2 are the distributions one gets for the two values of the incoming-channel spins using a 1^- assignment for the $C^{12}(9.64)$ state (Aj 59), with everything else the same as above. Explicitly,

$$W'_1(\psi) \sim 1 + P_2(\cos\psi)$$

and

$$W'_2(\psi) \sim 1 - P_2(\cos\psi) .$$

It is evident that no combination of W'_1 and W'_2 could be found that would reproduce the general trend of the experimental curve. Hence, the 1^- assignment is ruled out. On the other hand, it is equally evident that W_2 plus a small amount of W_1 rather closely resembles the experimental distribution. A smearing or flattening of the distribution and a shift in the symmetry axis are explicable considering the inability of the Born-approximation stripping theory alone to account for the increase in the neutron intensity at back angles (Sa 63). Therefore, the experimental

distribution of Figure 3-13 is considered to be strong evidence in favor of the 3^- assignment for the 9.64 MeV state of C^{12} .

(d) Two Parameter Measurements at $\theta_n = 45^\circ$

Two parameter analysis of the neutron time-of-flight spectra and the neutron-gated charged-particle spectra were carried out to obtain energy distributions of the alpha particles originating from the levels of C^{12} fed by the (d,n) stripping reaction and, where possible, to obtain angular distributions of these particles. With the neutron detector fixed at 45° in the laboratory system, the 12.71 MeV state is again the accentuated level of C^{12} as discussed earlier. The experimental arrangement was as described in part (a) of this section with the neutron flight path set at 1.15 meters. The 1024 channel, two parameter, TMC pulse-height analyzer operating in the 32 x 32 mode was used. Data were recorded for three positions of the solid state detector: $\gamma = 70^\circ$, 90° , and 120° . For angles greater than 120° , the (n, α) coincidence rate was too low to be practicable. As it was, the running time for each of the three mentioned angles was approximately three hours.

An isometric view of the two-parameter data obtained for $\gamma = 90^\circ$ is shown in Figure 3-14. The charged-particle-gated neutron time-of-flight spectrum is displayed on the y-axis, and the neutron-gated charged-particle spectra are displayed on the x-axes. The charged-particle spectrum at $y = 0$ corresponds to all the charged particles which are in coincidence with all the neutrons of the time

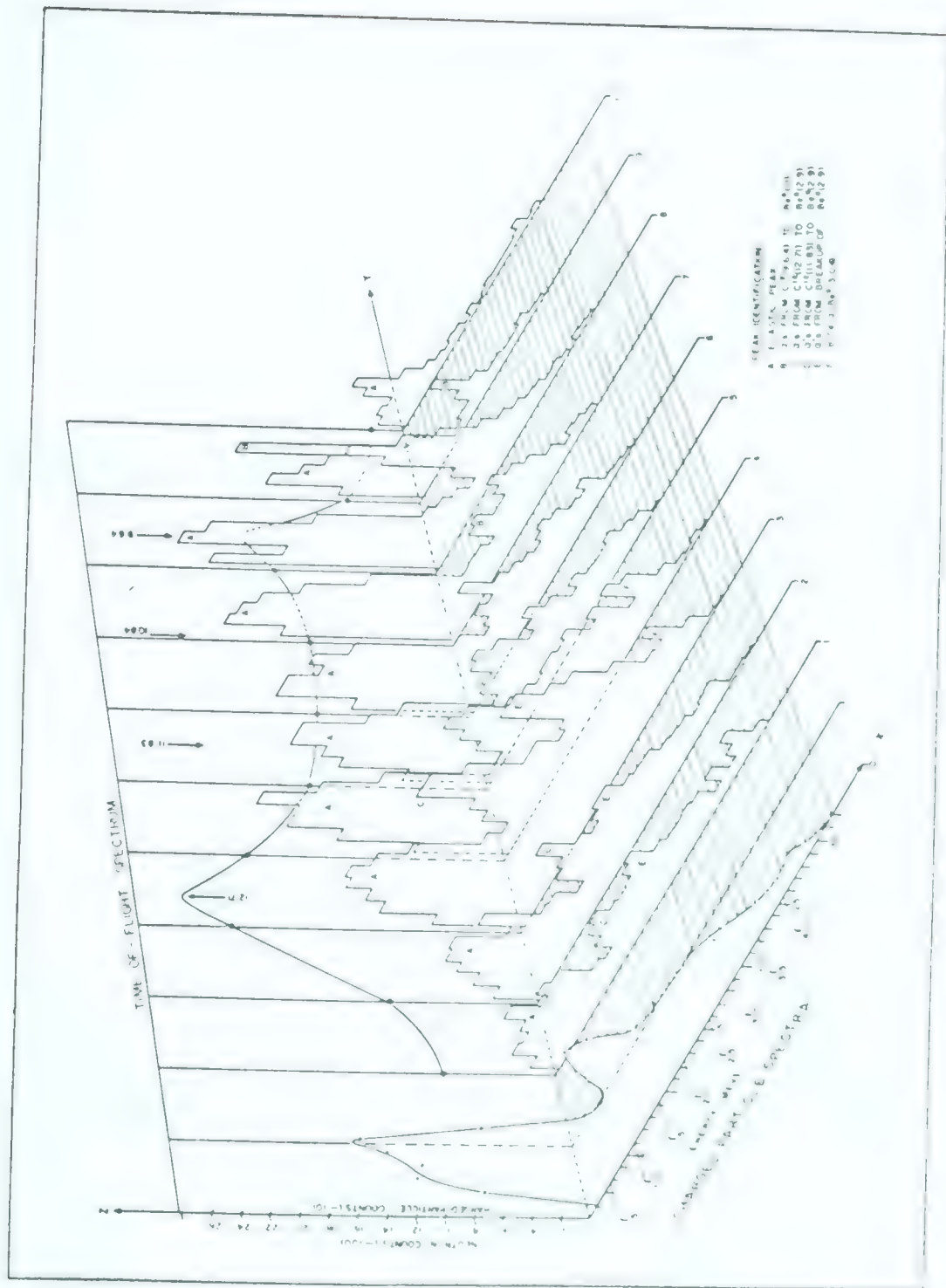


Figure 3-14. Isometric display of the two-parameter data obtained for $\theta_n \approx 45^\circ$, $S_n = 1.15$ meters, $\chi \approx 90^\circ$, and $E_d \approx 1.5$ MeV.

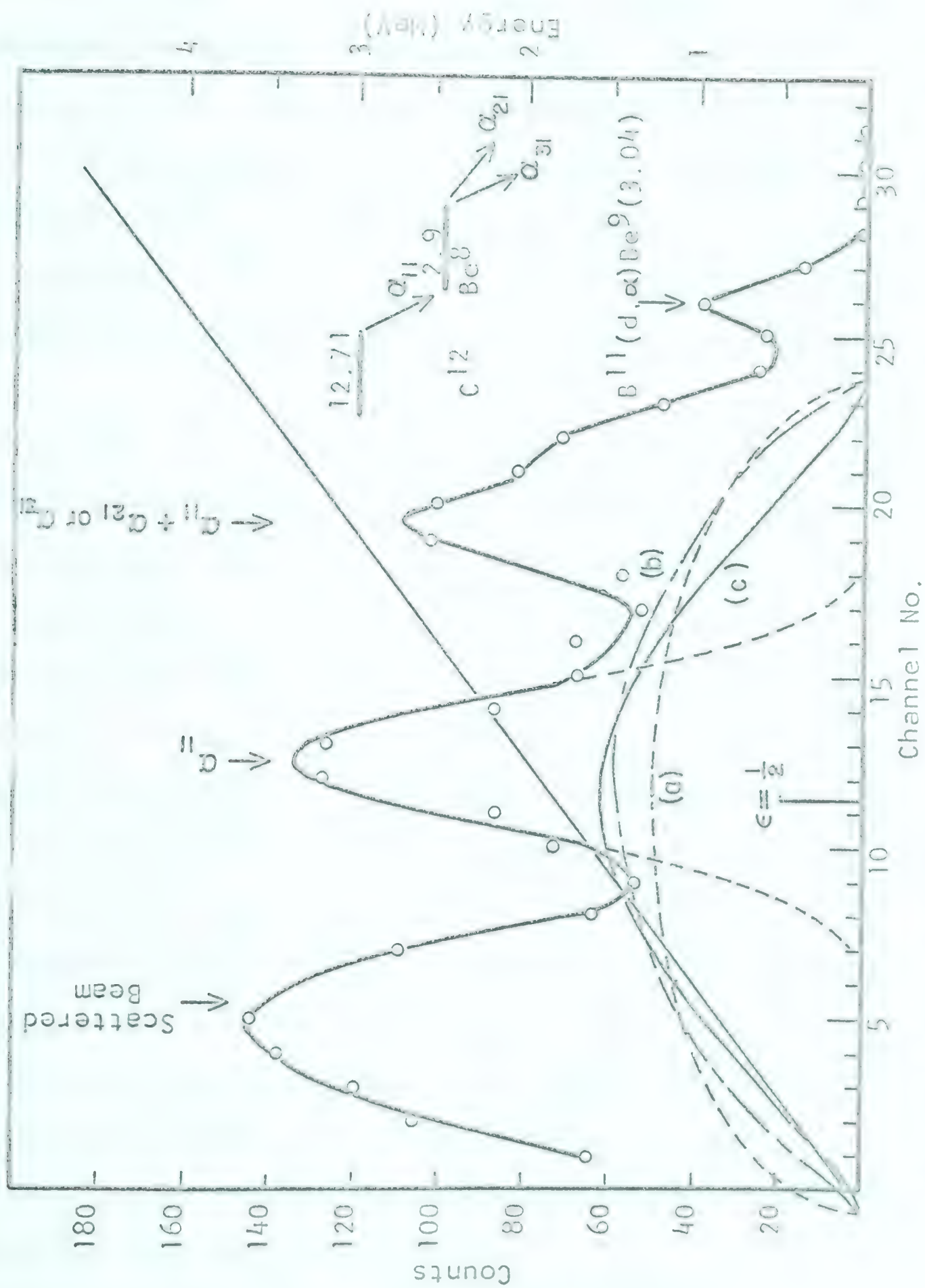


Figure 3-15. Expanded drawing of charged-particle spectrum no. 3 of Figure 3-14 with three-body breakup distributions.

spectrum (as in Figure 3-8a), and the others correspond to only those charged particles which are in coincidence with neutrons in the adjacent part of the neutron time-of-flight spectrum.

Of particular interest here is the spectrum of the charged particles which are in coincidence with the neutrons leading to the 12.71 MeV state of C^{12} . This spectrum is primarily contained in the one labelled no. 3 in the figure and, to a lesser extent, in spectrum no. 4.

Figure 3-15 shows spectrum no. 3 redrawn in greater detail. The large peak at the low energy end of the spectrum is the result of random coincidences between the neutrons and scattered deuterons. The two broad peaks at 2 and 3.1 MeV are only consistent with the interpretation that they are due to alpha particles from the sequential decay of the 12.71 MeV state through the 2.9 MeV state of Be^8 , with the 3 MeV peak ($\Gamma_{exp.} \sim .8$ MeV) resulting from the breakup of the Be^8 state, and the 2 MeV peak ($\Gamma_{exp.} \sim .7$ MeV) from the alphas leading to the Be^8 state.

Also shown in Figure 3-15 are three curves a, b, and c which represent the type of energy distributions one might expect if the 12.71 MeV level disintegrates by a direct three-body process. The three curves are neither normalized to each other nor to the experimental spectrum as they are presented only to show the general shapes of the three-body distributions.

Curve 'a' is the classical distribution (Ne 58) given by

$$f_a(\epsilon) = [\epsilon(1 - \epsilon)]^{1/2}$$

where $\epsilon = E/E_{\max}$, E is the center of mass energy of any one of the particles and E_{\max} is the maximum kinetic energy that it can have which, in this case, is $2/3 Q_D$ (Q_D = the disintegration energy = 5.43 MeV. The kinetic energy of the $C^{12}(12.71)$ nucleus has been neglected as it is not expected to significantly alter the shape of the distribution.

Curve 'b' is the classical distribution multiplied by the product of the three penetrability factors for the alpha particles. It was felt that such a function would at least illustrate the general nature of the distribution with centrifugal and coulomb barriers taken into account. Explicitly curve 'b' is given by

$$f_b(\epsilon_1) = f_a(\epsilon_1) P_1^{(1)} P_1^{(2)} P_0^{(3)}$$

where $P_\ell^{(n)}$ denotes the penetrability of the n^{th} particle emitted with orbital angular momentum ℓ . The ℓ values assigned were based on a 1^+ spin-parity assignment for the 12.71 MeV state. Two alphas with one unit of orbital momentum or one with two units (the others having zero units) are the only possibilities for this case, and of these two, the former would be more probable than the latter. The assumption was made that for a given value of ϵ_1 the other two alpha particles shared equally the remaining energy.

Curve 'c' shows the distribution one would expect using the function given by Delves (De 60) which takes into account the angular momentum barrier and the three-body impact parameter. In

general, this function is

$$f(\epsilon) = \epsilon^{\ell_1 + 1/2} (1 - \epsilon)^{\ell_2 + 1/2},$$

where $\ell_1 + \ell_2 = J$, the angular momentum of the decaying state. In particular, for this case the most probable value of ℓ_1 and ℓ_2 is again 1, so that

$$f_c(\epsilon) = \epsilon^{3/2} (1 - \epsilon)^{3/2}.$$

All three distributions indicate that there is a high probability that there would be an equal sharing of the disintegration energy among the three particles (and, hence, that the angular distribution of the particles would be isotropic). Such a sharing is clearly inconsistent with the experimental energy distribution.

The three points enclosed by triangles in Figure 3-12a were obtained from the peak heights of the 2 MeV group of Figure 15 and from the corresponding groups in the data for the other two angles, $\gamma = 70^\circ$ and 120° . They were normalized to 1.5 at 90° as well as corrected for the solid angle factor. They are in very good agreement with the data taken from the single parameter, time-of-flight spectra.

Very little can be said about the 11.83 MeV state of C^{12} from this two parameter data. If this level does decay through $Be^8(2.9)$, one would expect broad peaks in the regions of 1.5 MeV and 2-2.5 MeV. There are traces of such peaks in the charged-

particle spectrum (Figure 3-14, no. 5) associated with the 11.83 MeV level but the statistics are very bad since the neutron detector is well off the stripping peak for this level.

The decay of the 9.64 MeV C^{12} state to the ground state of Be^8 shows up very well in spectrum no. 8 of Figure 3-14. The effect of this level is also evident in spectra no. 7 and 9. Similar peaks were obtained in the data for the other two positions of the solid state detector (70° and 120°). Measurement of the area under the peaks due to the 9.64 MeV level for the three detector positions provided the three points of Figure 3-13 enclosed in triangles. These agree very well with the points of the angular distribution obtained from the single parameter time-of-flight spectra discussed in part (c).

(e) One-Parameter Measurements at $\theta_n = 0^\circ$

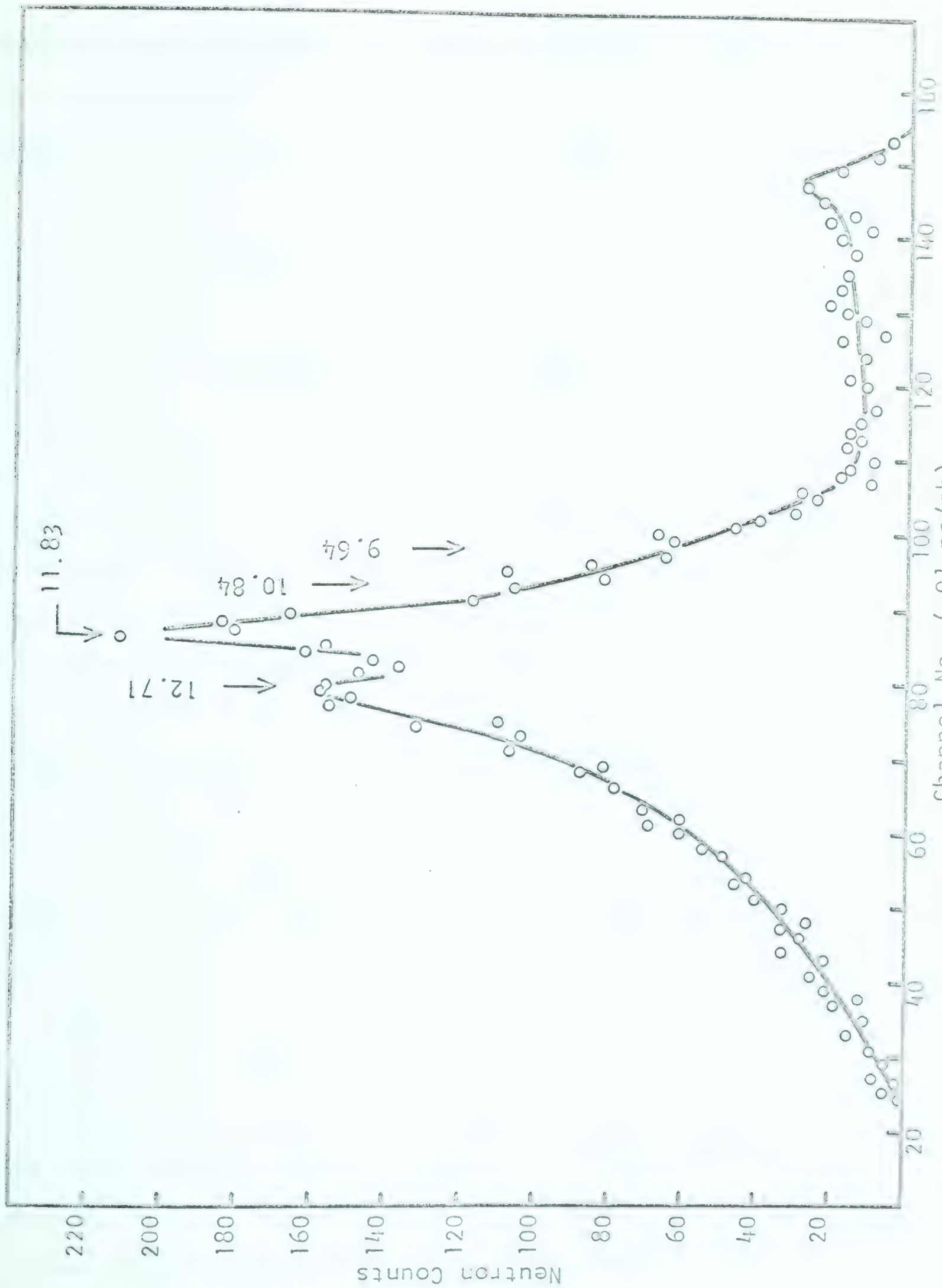
With the apparatus set up as described in part (c) of this section, one-parameter neutron time-of-flight spectra and neutron-gated charged-particle spectra were obtained with the neutron detector on the stripping peak of the 11.83 MeV level of C^{12} , zero degrees, for five settings of the solid state detector: $\gamma = 70^\circ$, 90° , 100° , 120° , and 140° . The 140° data are presented in Figure 3-16.

The angular distribution of the alpha particles from the decay of the 11.83 MeV state, as implied by the normalized and solid-angle-corrected neutron peaks corresponding to this state,

is isotropic within the statistics of the points. The corrected data are as follows:

γ	Corrected neutron Counts
70°	167 ± 13
90°	165 ± 13
100°	179 ± 14
120°	173 ± 13
140°	194 ± 14

There are four peaks in the neutron-gated charged-particle spectrum of Figure 3-16a. The two at 3.35 and 3.75 MeV are due to coincidences between the primary alpha particles and the neutrons produced in the reactions: $B^{11}(d,\alpha)Be^{9*}$ (3.04 and 2.43 respectively), $Be^{9*} \rightarrow n + Be^8$. The protons from the $C^{12}(d,p)C^{13}(gnd)$ reaction would also contribute some random coincidences to the 3.04 MeV peak. The peak at 1.5 MeV is due to alpha particles from the 12.71 MeV state of C^{12} to the 2.9 MeV state of Be^8 , and that at approximately 2 MeV can only be accounted for by alpha particles from the breakup of the 2.9 MeV state of Be^8 , fed by any or all of the levels in C^{12} at 10.84, 11.83, and 12.71 MeV. Alpha particles from the 10.84 MeV state to the Be^8 ground state, if this transition occurs, would contribute to the hump at 2.5 MeV. If the 11.83 MeV level decays through $Be^8(2.9)$, a broad peak at 1 MeV would be present; such a group would, however, be lost in the large peak resulting from random events. There is no evidence in any of the five charged-



Channel No. (.91 ns/ch)

Figure 3-16(b). Neutron time-of-flight spectrum. $\theta_n = 0^\circ$, $S_n = 1.15$ meters, $\gamma = 140^\circ$, $\theta_{tg} = 45^\circ$, $E_d = 1.5$ MeV. Charge = 500 microcoulombs.

particle coincidence spectra for peaks corresponding to transitions from the 11.83 or the 12.71 MeV states to the Be^8 ground state. In Figure 3-16a, these would occur at 2.9 and 3.5 MeV, respectively.

(f) Two-Parameter Measurements at $\theta_n = 0^\circ$

On the basis of the single-parameter spectra it can only be said that the 12.71 MeV state of C^{12} does not decay to the ground state of Be^8 , a conclusion which is in agreement with the measurements made at $\theta_n = 45^\circ$. Nothing, however, can be said regarding the disintegration of the 11.83 MeV level because of the complexity of these spectra. It was hoped that a two-parameter analysis of the neutron and charged-particle coincidence spectra would provide a definite indication of the decay mode of this state, and perhaps of the 10.84 MeV level as well since its stripping peak is also at 0° (Sa 62). The experimental arrangement was as described in part (d) of this section, with the neutron detector at 0° and the solid state detector at 90° and 140° .

An isometric drawing of the data obtained for $\gamma = 140^\circ$ is shown in Figure 3-17. The data taken at $\gamma = 90^\circ$ has the same general features so that the following remarks apply to both cases.

Spectrum no. 5 shows the charged particles in coincidence with the neutrons leading to the 11.83 MeV state; it is redrawn in Figure 3-18 to a larger scale to facilitate closer examination. The energy scale was obtained by comparing the 'single-parameter' spectrum, no. 0 of Figure 3-17, with that of Figure 3-16a and with a direct spectrum taken at 140° . The various alpha particles

resulting from the sequential decay of the 11.83 MeV state through Be^8 are shown in the energy level diagram in Figure 3-18. Their positions on the energy axis of the spectrum are also indicated, allowance having been made for the energy losses in the 10 μin . nickel foil in front of the solid state detector. Peaks corresponding to transitions to the ground state (α_{10}) and to the breakup of the 2.9 MeV state of Be^8 are evident. The latter peak, at approximately 1.5 MeV, no doubt contains alpha particles from the 2.9 MeV level of Be^8 fed from the 12.71 MeV level of C^{12} (as this level overlaps the 11.83 MeV level in the neutron time-of-flight spectrum), but must be due primarily to the alpha particles, α_{21} or α_{31} , from the 2.9 MeV level fed by the 11.83 MeV level of C^{12} as evidenced by the decided difference in character of the charged-particle spectra corresponding to the adjacent neutron time-of-flight channels (see Figure 3-17). The α_{11} group would be lost in the large peak at .75 MeV which is the result of random coincidences between neutrons and scattered deuterons from the beam. The hump in the spectrum at about 1.3 MeV could be a result of α_{20} and α_{30} summing in the detector.

Curves a, b, c, and d in Figure 3-18 are unnormalized three-body energy distributions, one of which would be expected to obtain if the 11.83 MeV level disintegrates by a direct three-body process. Curve 'a' is the classical distribution for this case and curve 'b' is the classical distribution modified by penetrability factors for the three alpha particles. That is,

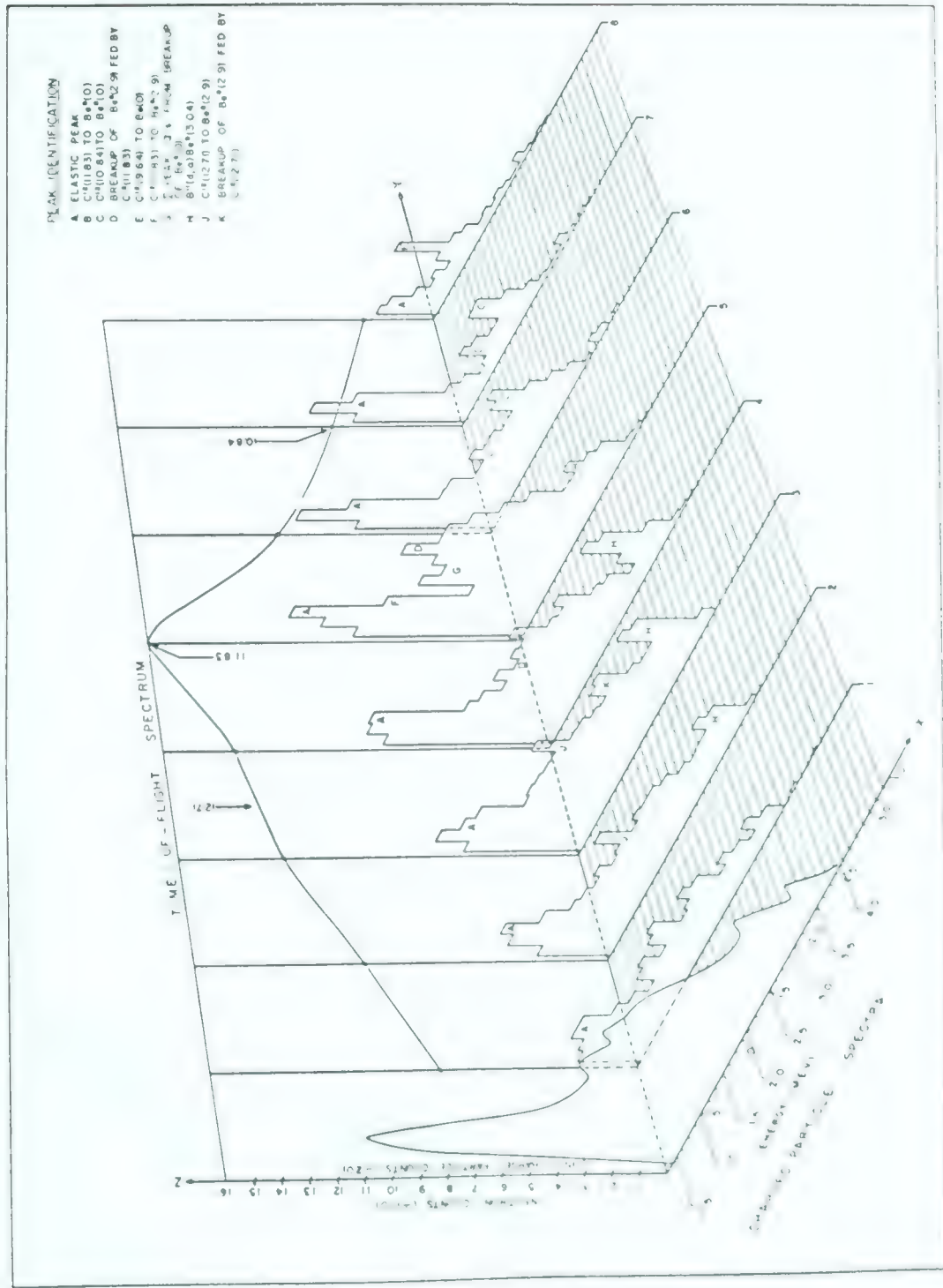
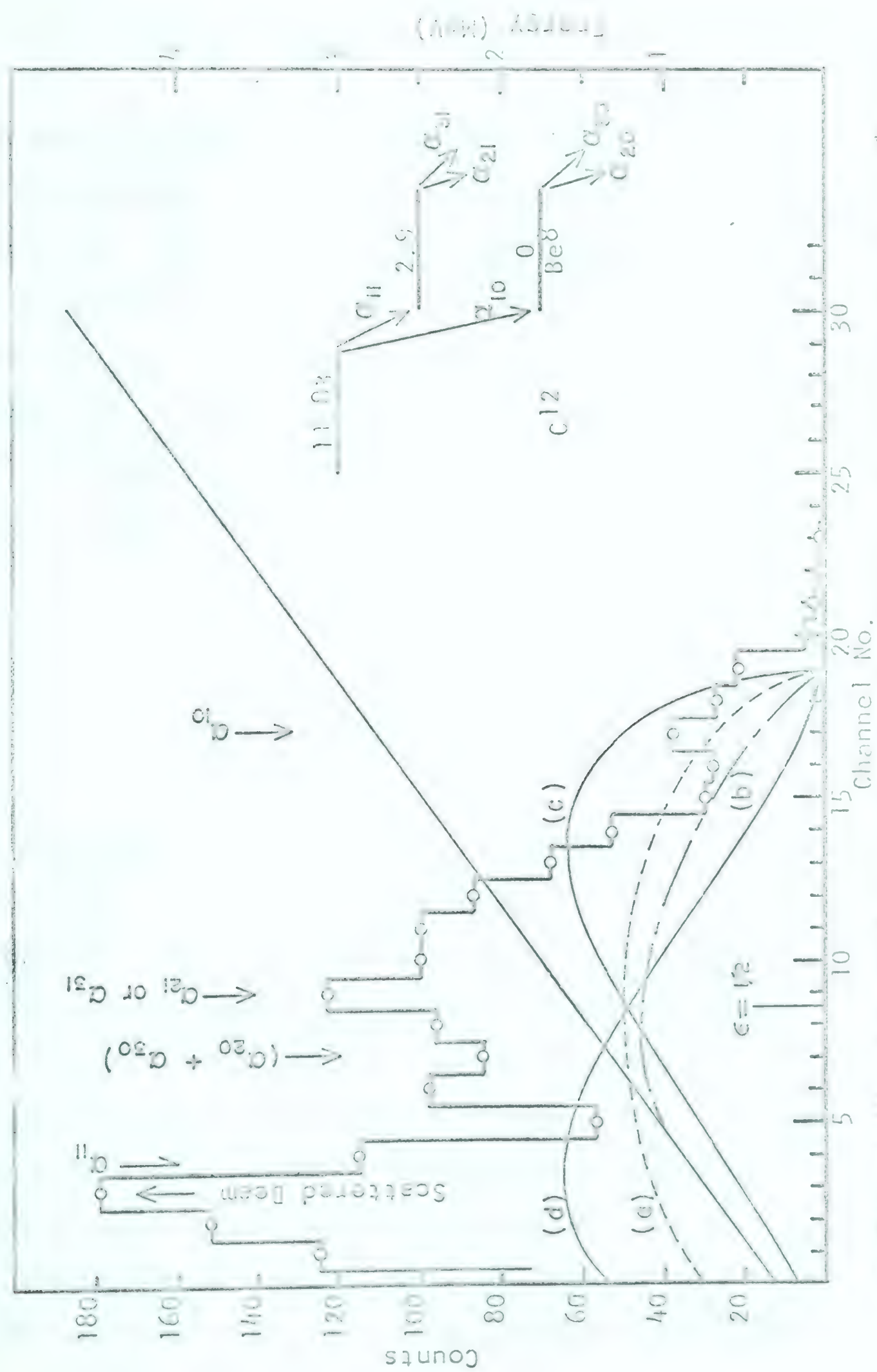


Figure 3-17. Isometric display of the two-parameter data obtained for $\theta_n = 0^\circ$, $S_n = 1.15$ meters, $\chi = 140^\circ$, and $E_D = 1.5$ MeV.



$$f_b(\epsilon_1) = f_a(\epsilon_1) P_1^{(1)} P_0^{(2)} P_0^{(3)}$$

where the assumptions have been made that particle 1 has the angular momentum of the carbon state ($J = 1$), and that for an assigned energy E_1 for particle 1, the other two particles share equally the remaining energy. Curve 'b' differs little in shape from 'a', both indicating that there would be an equal sharing of the disintegration energy among the three alpha particles. Curves 'c' and 'd' are the Delves (loc. cit.) distributions with $\ell_1 = 1$, $\ell_2 = 0$, and $\ell_1 = 0$, $\ell_2 = 1$ respectively. Explicitly,

$$f_c(\epsilon) = \epsilon^{3/2} (1 - \epsilon)^{1/2}$$

and

$$f_d(\epsilon) = \epsilon^{1/2} (1 - \epsilon)^{3/2}.$$

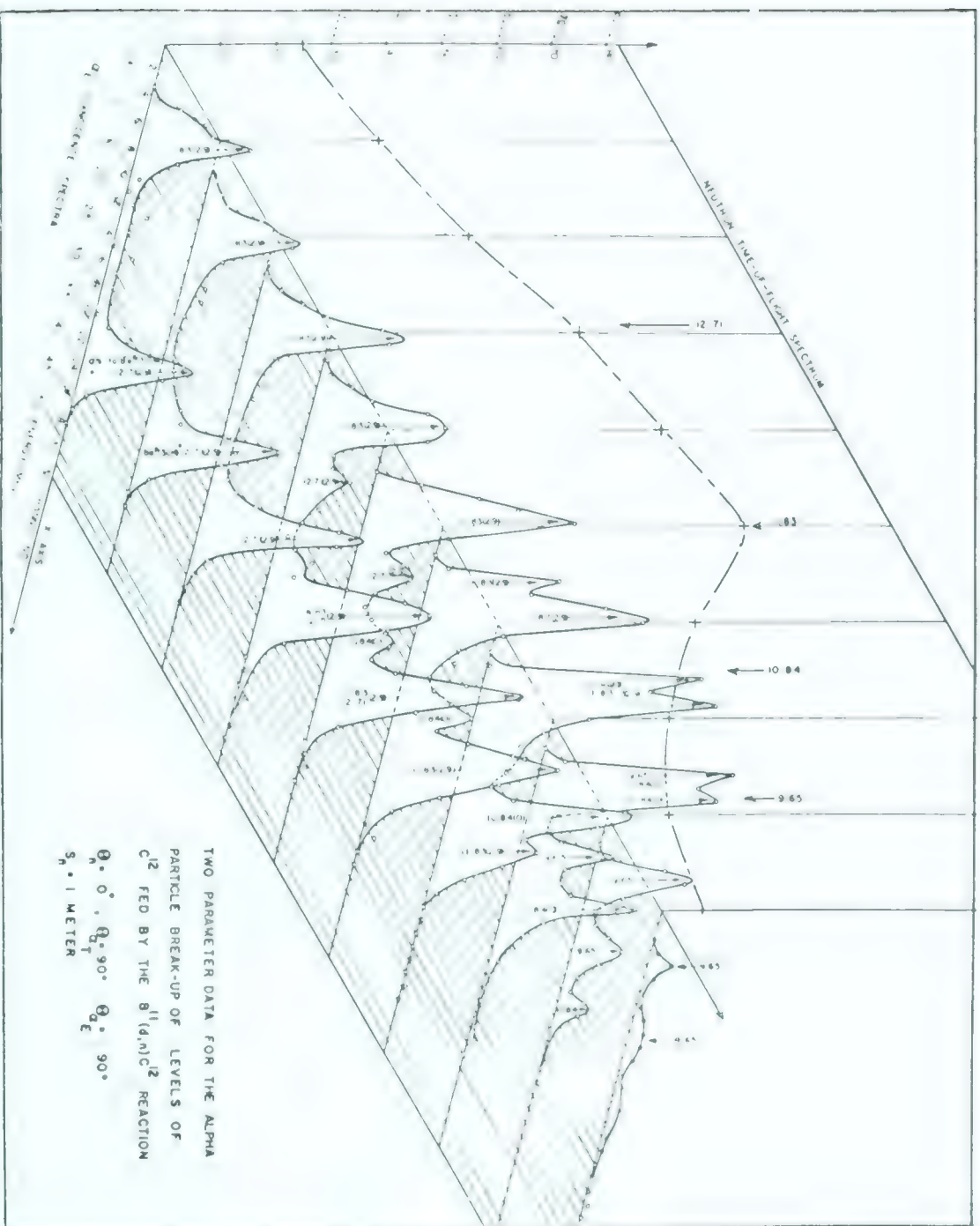
Of these three-body distributions, only curve 'd' could be considered to account in part for the measured distribution, with the three peaks riding on it. However, if this were the case, the number of counts in the "random" peaks (caused by chance coincidences between neutrons and scattered deuterons from the beam) of the charged-particle spectra would not follow the neutron time-of-flight spectrum. Therefore, it is considered that the three-body distributions cannot account for the shape of the charged-particle spectrum. On this basis it is concluded that the 11.83 MeV state decays entirely through Be^8 , and further that, from a crude measurement of the areas

under the peaks at 2.75 (α_{10}) and 1.5 (α_{21} or α_{31}) MeV, it is estimated that roughly ten percent of the transitions proceed via the Be^8 ground state.

The peaks in spectra no. 6 and 7 of Figure 3-17 at 2.25 MeV could only correspond to alpha particles from the 10.84 MeV state in C^{12} decaying to the ground state of Be^8 . This is in agreement with the only other observation of the decay of this state (see Chapter I).

IV. Measurements Using Two Solid State Detectors

A series of measurements employing two solid state detectors was carried out in an effort to detect two or all three of the alpha particles produced in the breakup of a given level of C^{12} . The counter geometry is shown in Figure 3-4b. The solid state detector (α_T) on the same side of the deuteron beam as the neutron spectrometer was used to provide the timing pulses. The pulse-height spectrum corresponding to the charged particles detected by the other solid state counter, α_E , in coincidence with particles detected by α_T (with a resolving time of 35 nanoseconds), was analyzed with the neutron spectrum by the two-parameter analyzer set up as previously described. The complete electronic arrangement is shown in Figure 2-5. Measurements were taken for several combinations of the detector positions, $(\theta_{\alpha_E}, \theta_{\alpha_T})$, at each of the neutron detector positions (0° and 45°). The running time for each geometry was the order of eight hours so that, in order to account for any drifts in the electronics during a run, the kicksorter was read out and cleared



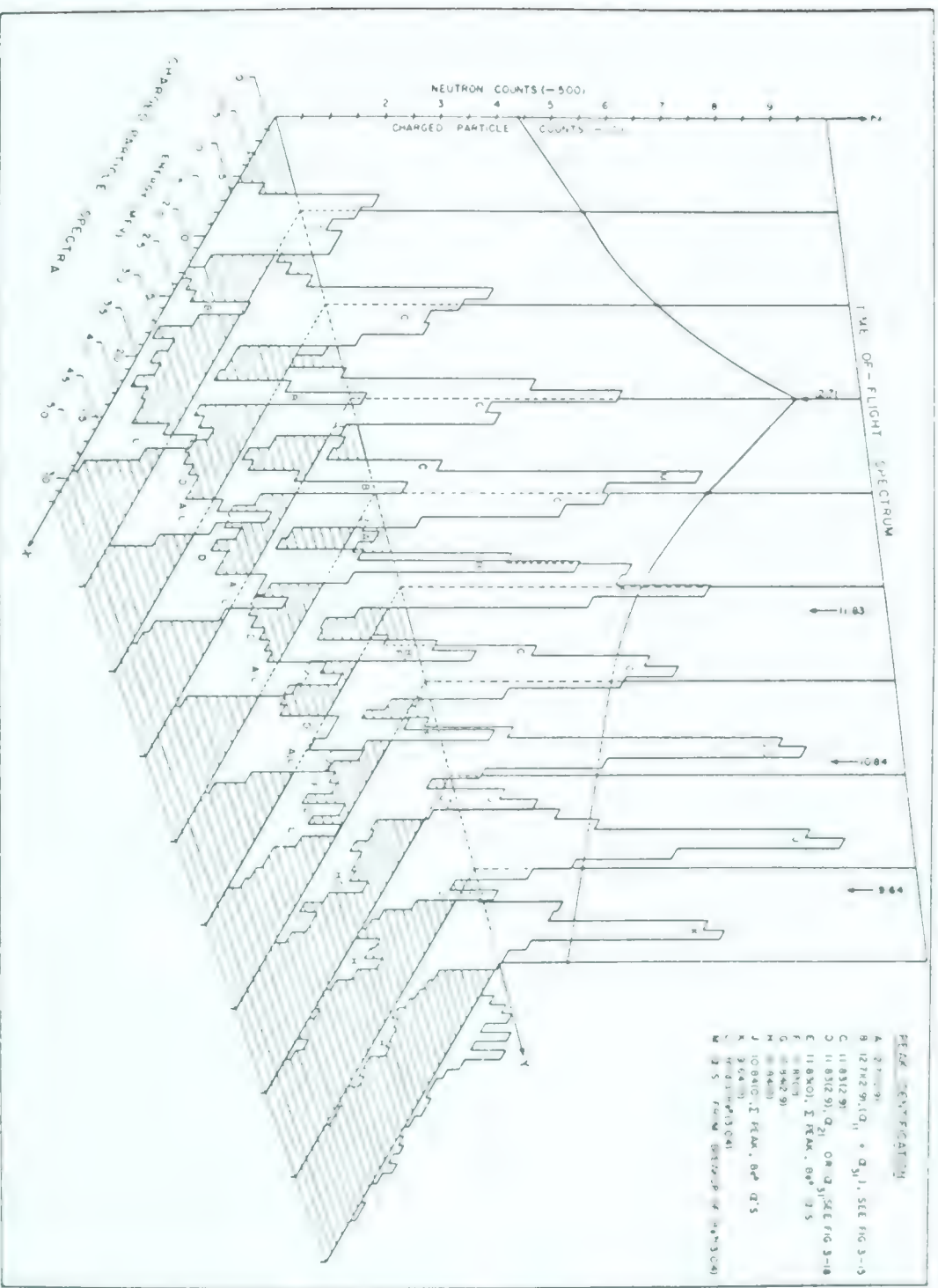


Figure 3-20. Isometric display of the two-parameter data obtained for $\theta_n \approx 45^\circ$, $S_n \approx 1$ meter, $\theta_{at} \approx 90^\circ$, $\theta_{\alpha E} \approx 85^\circ$, $E_d \approx 1.5$ MeV.

after every 100 μc of charge collected at the target (i.e., about every twenty minutes). A check on the random counting rate was obtained by delaying the α_{T} pulses with respect to the α_{E} pulses by 70 nanoseconds. On the basis of 100 μc runs, the true to chance ratio was greater than 25:1 for every geometry.

If the states of C^{12} decay sequentially through Be^8 , the kinematics are well defined, and peaks would be expected in the charged-particle spectra. On the other hand, flat spectra would be expected if the levels disintegrate by a direct three-body process. The experimental spectra obtained for every geometry investigated exhibited considerable structure. Representative of the data are Figures 3-19 and 3-20. The former shows the data in isometric display for $\theta_{\text{n}} = 0^\circ$, $\theta_{\alpha_{\text{E}}} = 90^\circ$, and $\theta_{\alpha_{\text{T}}} = 90^\circ$; and the latter for $\theta_{\text{n}} = 45^\circ$, $\theta_{\alpha_{\text{E}}} = 85^\circ$, and $\theta_{\alpha_{\text{T}}} = 90^\circ$. The various peaks in these spectra can be attributed to alpha particles originating from the 9.64, 10.84, 11.83, and 12.71 MeV states of C^{12} , and are labelled accordingly. The number 0 or 2,9 in brackets following the C^{12} assignment indicates the state of Be^8 involved. These assignments were made on the basis of kinematic calculations performed by the IBM 1620 computer to determine the energies of the three alpha particles for each decay as functions of their laboratory angles of emission, assuming that the decay proceeds sequentially through Be^8 . These calculations are fully described in Appendix I, Nuclear Reactions III.

V. Conclusions

The alpha-particle energy spectra and angular distributions obtained in this work indicate that the 12.71 and 11.83 MeV levels of C^{12} decay predominantly through Be^8 . The absence of transitions to the Be^8 ground state supports the 1^+ spin-parity assignment for the 12.71 MeV state. About 90 per cent of the transitions from the 11.83 MeV state go through the 2.9 MeV state while the remaining 10 per cent feed the ground state.

It is likely that the 10.84 MeV state of C^{12} decays primarily to the ground state of Be^8 . This is in agreement with the only other observation of the decay of this state. Transitions to the first excited state of Be^8 are not ruled out by the present work, however.

The angular distribution of the alpha particles from the 9.64 MeV state strongly supports the 3^- assignment for this level as opposed to the 1^- assignment.

The information obtained from this work on the alpha-particle decay of the levels between 9 and 13 MeV excitation, coupled together with the available information (see Chapter I) on the decay of the other levels in C^{12} , supports the $Be^8-\alpha$ Two-Body Cluster Model representation of the C^{12} nucleus, at least to 16 MeV excitation.

This work also eliminates the simultaneous three-body breakup of the carbon states between 9 and 13 MeV as being the source of

the neutron continuum observed in the neutron time-of-flight spectrum (see Figure 3-1). It is suggested then that this continuum may be caused by the overlapping of the C^{12} levels including the very broad level at 10.1 MeV (Ni 62). Neutrons from the breakup of the 3.04 and the 2.43 MeV states of Be^9 formed by the $B^{11}(d,\alpha)Be^{9*}$ reaction will also contribute to this continuum.

APPENDIX I

THE KINEMATICS OF NUCLEAR REACTIONS

I. Introduction

Three programs have been written for the University of Alberta IBM 1620 computer to provide nonrelativistic solutions to the kinematics of nuclear reactions. The first and most generally useful program deals with reactions of the type

$$M_1 + M_2 \rightarrow M_3 + M_4 \quad (1)$$

or more briefly, $M_2(M_1, M_3)M_4$. Here M_1 is the bombarding particle, M_2 the target nucleus, M_3 the light reaction product, and M_4 the heavy (recoil) reaction product. The second program considers reactions of the type (1) where the residual nucleus, M_4 , breaks up into two more particles, M_5 and M_6 . This program then is suitable only for cases when M_4 is formed in an unbound state. The third program goes one step further and determines the energies of the particles formed in the breakup of M_6 into M_7 and M_8 . This program was written specifically to provide the energies and angles of emission of the three alpha particles produced in the breakup of C^{12} levels formed by the $B^{11}(d, n)C^{12*}$ reaction, assuming a two stage disintegration process through states in Be^8 , this reaction being the subject material of this thesis.

II. Programs

A. Nuclear Reaction I

This program is concerned with reactions of the type (1). Ball (Ba62) has written a similar program for the 709/7090 computer at Oak Ridge, and some of the features of his treatment are incorporated here. Tables are also available (Ma59) for the computation of the energies of nuclear reaction products, and for the transformation of quantities between the laboratory and the center of mass systems. However, tables are awkward and time consuming when complete kinematic solutions are required for a large number of reactions, as is the case when unravelling the complex spectra obtained in charged particle spectrometry. The program of Ball (Ba62) was unsatisfactory from the point of view of incompatibility with the 1620 computer.

Nuclear Reactions I computes as a function of the laboratory angle of emission of the light reaction product, M_3 , the corresponding center of mass angle, the laboratory energy of M_3 , the ratio of the cross-section in the center of mass to that in the laboratory for M_3 , the energy and laboratory angle of emission of the residual nucleus, M_4 , the momentum transfer wave number and the magnetic rigidity of M_3 . An interaction radius parameter $R/R_0 = (M_1^{1/3} + M_2^{1/3})$ is used to calculate the scattering argument.

Input Data

The input data are punched on five IBM, 80 column, cards. The following table (Table 1) indicates what information is contained on each card, and at what position on the card the data should appear. The cards should be arranged in the order given below. Any number of sets of data may be stacked together.

Table 1

Card No.	Symbol	Definition	Field begins at column	Units
1		Title Card; the first 55 columns, beginning with column 2, are available. Any notation to identify the reaction is permitted.		
2	EM1	Mass of the incident particle, M_1	2	amu
2	EM2	Mass of the target nucleus, M_2	14	amu
2	EM3	Mass of the light reaction product, M_3	26	amu
2	EM4	Mass of the residual nucleus, M_4	38	amu
3	QS	The Q of the reaction to excited state S of the residual nucleus	2	Mev
4	E1S	'Starting' incident energy of M_1	2	Mev
4	DE1	Increment in incident energy	14	Mev
4	E1F	Final incident energy of M_1	26	Mev
5	THETS	Starting laboratory angle for particle M_3 (≥ 0)	2	radians
5	DTHET	Angular increment (>0)	14	radians
5	THETF	Maximum laboratory angle for M_3 ($\leq 180^\circ$)	26	radians

Output

The listing of computed, angle dependent quantities is preceded by a heading which contains the input data (excluding the angle input data) and some computed, angle independent quantities. Table 2 indicates the significance of the computed quantities in the heading.

Table 2

Symbol	Definition	Units
E1COM	The energy of the incident particle (M_1) in the initial center of mass system	Mev
EICOM	The total kinetic energy in the initial center of mass system	Mev
EFCOM	The total kinetic energy in the final center of mass system	Mev
E3COM	The energy of M_3 in the final center of mass system	Mev
E4COM	The energy of M_4 in the final center of mass system	Mev
K1,K2	Wave numbers of M_1 and M_3 in the center of mass system	fermi ⁻¹
R OVER RO	The interaction radius divided by the nuclear radius parameter	

Table 3 shows the column headings for the listing of the remaining computed quantities.

Table 3

Symbol	Definition	Units
THETALAB	The laboratory angle theta of emission of M_3 (input data)	degrees
THETACOM	The center of mass angle corresponding to the input angle theta	degrees
PHI	The laboratory angle of the recoil nucleus, M_4	degrees
E3	Laboratory energy of the light reaction product, M_3	Mev
E4	Laboratory energy of the heavy reaction product, M_4	Mev
XSEC-CMTOL	The ratio of the cross-section in the center of mass to that in the laboratory system for the light reaction product, M_3	
KCOM	The relative wave-vector of the particles M_1 and M_3 in the center of mass system	fermis ⁻¹
KR OVER RO	The scattering argument divided by the nuclear radius parameter	
BRZ	The magnetic rigidity of particle M_3 , the light reaction product	kilogauss-inches

A typical Fortran II output page is shown in Figure 1 for the reaction $B^{11}(d,n)C^{12*}(12.71)$ at a deuteron bombarding energy, E_1 , of 1.5 Mev.

When the velocity of the center of mass in the initial system

exceeds the center of mass velocity of the light reaction product, M_3 , E_3 becomes double valued, and the maximum allowable angle, θ , is restricted to values below 180 degrees. In such cases, the program will automatically replace THETF by the calculated maximum angle, provided, of course, that THETF exceeded this maximum angle in the first place. The two values of those items tabulated in Table 3 appear one after the other in the listing of the output.

The computer time required for this program is three minutes per Q value per E_1 value for θ varying from 0 to 180° in 5° intervals.

Kinematics

Figures 2 and 3 show the velocity diagrams of reactions of the type $M_2(M_1, M_3)M_4$. Figure 2(a) depicts the situation in the initial laboratory system with the bombarding particle M_1 approaching the stationary target nucleus M_2 with a velocity v_1 and energy E_1 . Figure 2(b) shows the reaction products in the final laboratory system in which the light product M_3 , with velocity v_3 and energy E_3 , is emitted at an angle θ with respect to the direction of the incident beam and in which the residual or recoil (heavy) nucleus, M_4 , is emitted at an angle ϕ with velocity v_4 and energy E_4 .

Figure 3(a) shows the situation just prior to the reaction in the initial center of mass system. The projectile and the target nucleus are approaching one another with velocities V_1 and V_2 respectively, where

$$V_1 = \frac{M_2}{M_1 + M_2} v_1 \quad (2)$$

and

$$V_2 = \frac{M_1}{M_1 + M_2} V_1 = V_{cm} \quad (3)$$

where V_{cm} is the laboratory velocity of the center of mass of the initial system. It is worth noting, for future reference, that

$$V_{cm}^2 = \frac{2M_1 E_1}{(M_1 + M_2)^2}, \quad (4)$$

and also that ElCOM as defined in Table 1 is given by

$$\text{ElCOM} = \frac{M_2^2}{(M_1 + M_2)^2} E_1. \quad (5)$$

The total kinetic energy available in the initial center of mass system, ElCOM, is given by

$$\text{ElCOM} = \frac{1}{2} M_1 V_1^2 + \frac{1}{2} M_2 V_2^2 = \frac{M_2}{M_1 + M_2} E_1, \quad (6)$$

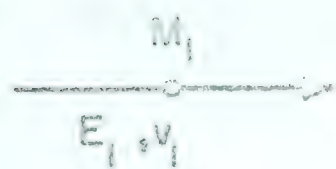
or more simply by

$$\text{ElCOM} = E_1 - E_{cm} = \frac{M_2}{M_1 + M_2} E_1$$

where E_{cm} is the energy of the center of mass of the initial system,

DEUTERONS ON BORON 11(D,N) STRIPPING TO THE 12.71 STATE												
M1=	2.014742	M2=	11.012805	M3=	1.008986	M4=	12.003815					
QS=	1.022000											
E1=	1.50000	E1COM=	1.07191	E1COM=	1.26802	EFCOM=	2.29002					
E3COM=	2.11245	E4COM=	.17756									
K1=	.32139	K3=	.31928	R OVER	R0=	3.48783						
THETALAB	THETACOM	PHI	E3	E4	XSEC-CMTOL	KCOM	KR OVER	R0	BRZ			
0.00	0.00	179.99	2.520	.001	.8382	.0021	.0073		90.3652			
4.99	5.46	43.09	2.518	.003	.8388	.0305	.1066		90.3334			
9.99	10.91	58.67	2.513	.008	.8405	.0609	.2127		90.2386			
14.99	16.36	63.95	2.504	.017	.8433	.0912	.3181		90.0816			
19.99	21.80	65.57	2.492	.029	.8472	.1212	.4227		89.8638			
24.99	27.23	65.55	2.476	.044	.8522	.1508	.5261		89.5874			
29.99	32.64	64.68	2.458	.063	.8583	.1800	.6280		89.2549			
34.99	38.03	63.32	2.437	.084	.8654	.2087	.7281		88.8695			
39.99	43.39	61.65	2.413	.108	.8737	.2368	.8262		88.4346			
44.99	48.73	59.79	2.387	.134	.8829	.2643	.9220		87.9543			
49.99	54.05	57.78	2.359	.162	.8931	.2911	1.0153		87.4329			
54.99	59.33	55.68	2.329	.192	.9043	.3171	1.1060		86.8751			
59.99	64.58	53.51	2.297	.224	.9164	.3422	1.1937		86.2858			
64.99	69.79	51.30	2.265	.256	.9293	.3655	1.2784		85.6702			
69.99	74.97	49.05	2.231	.290	.9431	.3898	1.3598		85.0335			
74.99	80.11	46.79	2.197	.324	.9575	.4122	1.4380		84.3810			
79.99	85.21	44.51	2.162	.358	.9726	.4337	1.5126		83.7181			
84.99	90.27	42.22	2.128	.393	.9882	.4540	1.5838		83.0502			
89.99	95.29	39.93	2.094	.427	1.0042	.4734	1.6513		82.3825			
94.99	100.27	37.64	2.060	.460	1.0206	.4917	1.7151		81.7202			
99.99	105.21	35.36	2.028	.493	1.0372	.5090	1.7753		81.0682			
104.99	110.11	33.09	1.996	.525	1.0538	.5251	1.8316		80.4314			
109.99	114.97	30.82	1.965	.555	1.0704	.5402	1.8843		79.8142			
114.99	119.79	28.56	1.936	.584	1.0868	.5542	1.9331		79.2210			
119.99	124.58	26.31	1.909	.612	1.1028	.5672	1.9783		78.6558			
124.99	129.33	24.07	1.883	.638	1.1183	.5790	2.0196		78.1222			
129.99	134.05	21.84	1.859	.662	1.1331	.5898	2.0573		77.6238			
134.99	138.73	19.63	1.837	.684	1.1471	.5995	2.0912		77.1637			
139.99	143.39	17.42	1.817	.704	1.1601	.6082	2.1215		76.7446			
144.99	148.03	15.22	1.799	.721	1.1720	.6159	2.1481		76.3690			
149.99	152.64	13.03	1.784	.737	1.1826	.6225	2.1711		76.0392			
154.99	157.23	10.84	1.771	.750	1.1918	.6280	2.1906		75.7570			
159.99	161.80	8.67	1.760	.761	1.1994	.6326	2.2064		75.5240			
164.99	166.36	6.49	1.751	.769	1.2055	.6361	2.2187		75.3414			
169.99	170.91	4.33	1.745	.776	1.2099	.6386	2.2275		75.2103			
174.99	175.45	2.16	1.742	.779	1.2126	.6401	2.2328		75.1313			
179.99	179.99	0.00	1.740	.780	1.2135	.6406	2.2345		75.1049			

Figure 1. Kinematics for the reaction $B^{11}(d,n)C^{12}(12.71)$ for $E_d = 1.5$ MeV.



$$v_2 = 0$$

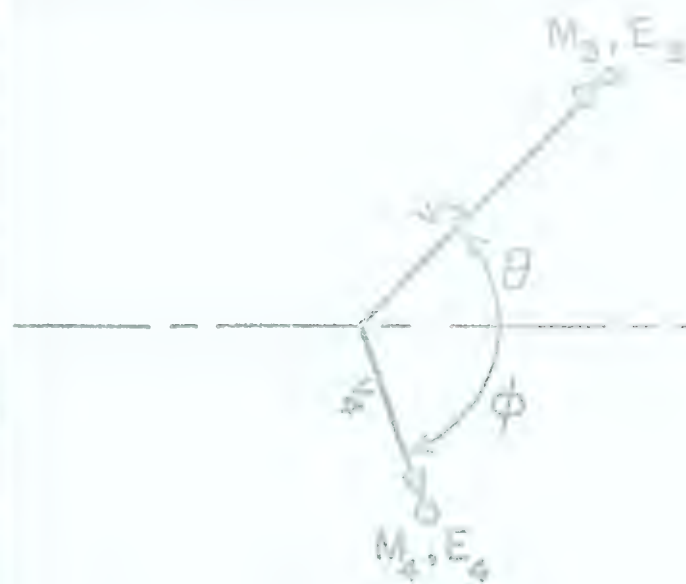


Fig. 2(a) Initial Lab. System

(b) Final Lab. System

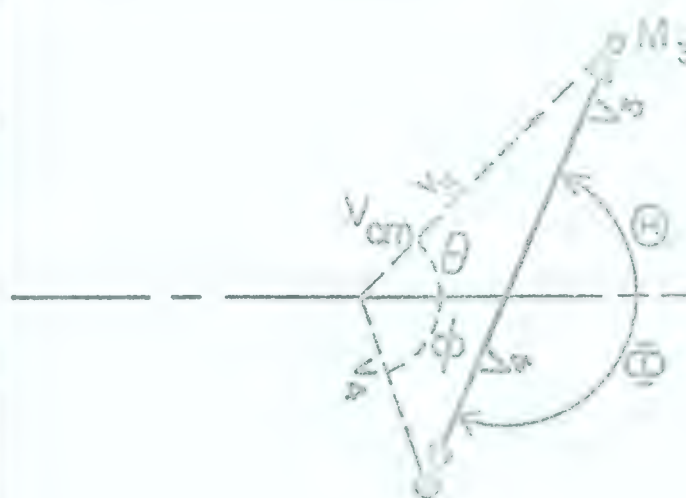
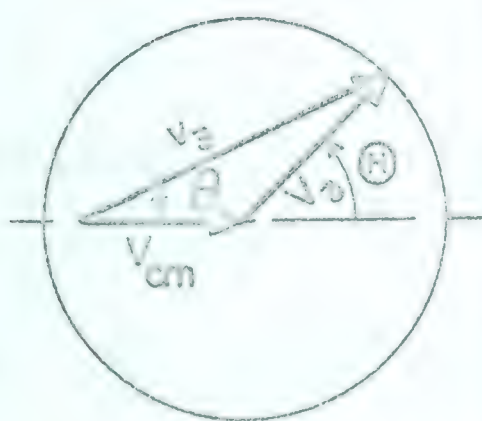
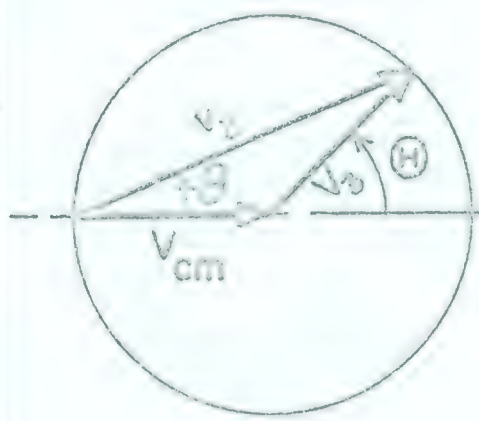


Fig. 3(a) Initial C of M System

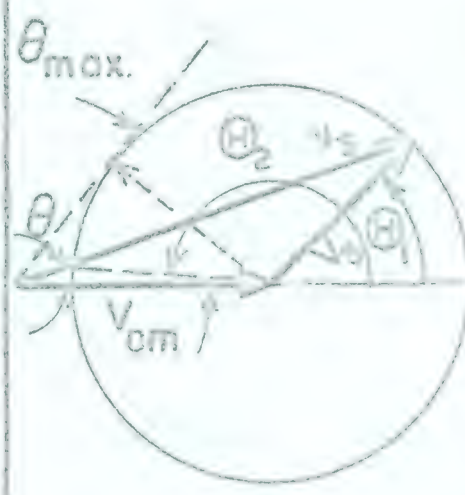
(b) Final C of M System



(a)
 $v_{cm} < v_3$



(b)
 $v_{cm} = v_3$



(c)
 $v_{cm} > v_3$

Fig. 4

and is seen from equation (4) to be

$$E_{cm} = \frac{M_1}{M_1 + M_2} E_1 . \quad (7)$$

The total disintegration energy in the final center of mass system, shown in Figure 3(b), is the Q of the reaction plus the kinetic energy available in the initial center of mass system. That is,

$$E_{FCOM} = Q_s + E_{1COM} \quad (8)$$

With reference to Figure 3(b), and by applying the laws of conservation of energy and momentum, the center of mass energies of the reaction products can be determined:

$$\frac{1}{2} M_3 V_3^2 + \frac{1}{2} M_4 V_4^2 = E_{FCOM} \quad (9)$$

and

$$M_3 V_3 = M_4 V_4 , \quad (10)$$

from which

$$E_{3COM} = \frac{M_4}{M_3 + M_4} E_{FCOM} \quad (11)$$

and

$$E_{4COM} = \frac{M_3}{M_3 + M_4} E_{FCOM} . \quad (12)$$

Convenient expressions for the laboratory energies of the reaction products, M_3 and M_4 , are obtained by applying the cosine law to the velocity triangles of Figure 3(b). The expression for E_3 is:

$$1/2 M_3 v_3^2 = 1/2 M_3 v_{cm}^2 + 1/2 M_3 v_3^2 + 2(M_3/2) v_{cm} v_3 \cos(\theta) \quad (13)$$

or

$$E_3 = A_o^2 + B_o^2 + 2A_o B_o \cos\theta \quad (14)$$

where

$$A_o^2 = \frac{M_1 M_3 E_1}{(M_1 + M_2)^2} \quad \text{and} \quad B_o^2 = E_3 \text{COM},$$

In a similar manner, using the triangle of Figure 3(b) associated with residual nucleus, M_4 :

$$E_4 = A_1^2 + B_1^2 - 2A_1 B_1 \cos\theta \quad (15)$$

where

$$A_1^2 = \frac{M_1 M_4 E_1}{(M_1 + M_2)^2} \quad \text{and} \quad B_1^2 = E_4 \text{COM}.$$

Before equations (14) and (15) can be used, the input angle, θ , must be converted to the corresponding center of mass angle, θ . Applying the law of sines to the upper velocity triangle of Figure 3(b),

$$\sin(\Theta - \theta) = (v_{cm}/v_3) \sin\theta. \quad (16)$$

The symbol used in the program for the difference $(\Theta - \theta)$ is D , and $V_{cm}/V_3 = A_0/B_0 = \gamma$. Because the computer subroutine library does not contain the inverse sine functions, a transformation to a tangent function is necessary:

$$\tan(D) = \sin(D) / \{1 - \sin^2(D)\}^{1/2} \quad (17)$$

and, hence, $\Theta = \text{ArcTan}\{\tan(D)\} + \theta$. (18)

The angle of emission of the residual nucleus in the laboratory system can be obtained by applying the sine law to the lower velocity triangle of Figure 3(b). That is,

$$\sin\phi = (V_4/V_{cm})\sin(\Theta + \phi)$$

or, by expanding the right-hand side and dividing by $\cos\phi$,

$$\tan\phi = \frac{\sin\Theta}{A_1/B_1 - \cos\Theta} \quad (19)$$

since $V_{cm}/V_4 = A_1/B_1$.

Under certain conditions the energies of the reaction products will be double valued, and the laboratory angle, θ , will be restricted to values less than 180° . These conditions are depicted in Figure 4. Figure 4(a) shows the usual case where the velocity of the center of mass, V_{cm} , is less than the velocity of M_3 , V_3 , in the final center of mass system. For this case, E_3 is single valued, and

θ can take on any value up to and including 180° . When V_{cm} is equal to V_3 , as shown in Figure 4(b), the maximum value that θ can take is 90° as this corresponds to 180° in the center of mass system. E_3 is still single valued, however. Figure 4(c) shows the situation where V_{cm} is larger than V_3 : there is a second center of mass angle, θ_2 , corresponding to a given θ , and hence two values of E_3 for a given θ . The value of θ_2 can be obtained from the geometry of Figure 4(c), and is given by

$$\theta_2 = \pi + 2\theta - \theta_1 . \quad (20)$$

This new value for the center of mass angle is then used to recalculate all those quantities in the output listing which are angle dependent. The two values of each item follow one another consecutively in the listing. It can also be seen from Figure 4(c), or from equation (28), that θ_{max} is restricted to a value less than 180° , and that it is given by

$$\sin \theta_{max} = V_3/V_{cm} = B_o/A_o = 1/\gamma \quad (21)$$

from which

$$\theta_{max} = \text{ArcTan}\{1/(\gamma^2 - 1)^{1/2}\} . \quad (22)$$

The computer examines the value of γ to ascertain which of the above three conditions obtains:

- i. if $\gamma < 1$, the computer proceeds with the range of as specified in the input data,
- ii. if $\gamma = 1$, THETF is replaced by $\pi/2$ provided that THETF exceeded $\pi/2$ in the first place,
- iii. if $\gamma > 1$, θ_{\max} is computed from equation (21), and replaces THETF provided that THETF exceeded θ_{\max} in the first place.

The Center of Mass Correction for M_3

Before measured cross sections or angular distributions can be compared with theory, it is necessary to convert them to the center of mass system of coordinates. The total intensity of reaction product, M_3 , is the same in both systems, so that

$$\sigma_{\text{lab}}(\theta) \sin\theta d\theta = \sigma_{\text{CM}}(\theta) \sin\theta d\theta \quad (23)$$

where $\sigma_{\text{lab}}(\theta)$ is the differential cross section as measured in the laboratory system, and $\sigma_{\text{CM}}(\theta)$ is the differential cross section as measured in the center of mass system. The azimuthal angle is the same in both systems and therefore has not been included in equation (23). The correction factor required is

$$\frac{\sigma_{\text{CM}}(\theta)}{\sigma_{\text{lab}}(\theta)} = \frac{\sin\theta}{\sin\Theta} \frac{d\theta}{d\Theta} \quad (24)$$

With reference to Figure 3(b)

$$\frac{\sin\theta}{\sin\Theta} = v_3/v_3 \quad (25)$$

and
$$\sin(\theta - \theta) = (v_{cm}/V_3)\sin\theta = \gamma\sin\theta \quad (26)$$

from which
$$\frac{d\theta}{d\theta} - 1 = \frac{d}{d\theta} \{\sin^{-1}(\gamma\sin\theta)\}$$

so that
$$\frac{d\theta}{d\theta} = \frac{(1 - \gamma^2 \sin^2 \theta)^{1/2}}{\gamma \cos \theta \pm (1 - \gamma^2 \sin^2 \theta)^{1/2}} \quad (27)$$

However, by applying the cosine law to the upper velocity triangle of Figure 3(b) it can be seen that the denominator of equation (27) is simply v_3/V_3 . That is,

$$v_3 = V_3[\gamma \cos \theta \pm (1 - \gamma^2 \sin^2 \theta)^{1/2}] \quad (28)$$

Therefore,
$$\frac{\sigma_{cm}(\theta)}{\sigma_{lab}(\theta)} = \frac{(1 - \gamma^2 \sin^2 \theta)^{1/2}}{v_3^2/V_3^2}$$
$$= (B_o^2/E_3)(1 - \gamma^2 \sin^2 \theta)^{1/2} \quad (29)$$

Equation (29) is in terms of previously computed quantities, and is the one which is used to calculate the center of mass correction factor.

Other quantities which are useful in angular distribution analysis are the wave numbers of the incoming projectile and the light reaction product, M_3 , and the relative wave number of the transferred momentum. These can be obtained directly from quantities which have already been computed. The general expression for wave number of a particle of

mass M and with energy E is

$$K = \frac{(2ME)^{1/2}}{\hbar} \text{ fermi}^{-1} \quad (30)$$

where \hbar is Planck's constant. Using this relationship, the equation for the wave number of M_1 in the initial center of mass system is

$$K_1^2 = M_1(E1COM)/20.908 \text{ fermi}^{-2} . \quad (31)$$

And for M_3 in the final center of mass system,

$$K_3^2 = M_3(E3COM)/20.908 \text{ fermi}^{-2} . \quad (32)$$

The relative wave number, K , of the transferred momentum is then given as shown in Figure 5 by

$$K^2 = K_1^2 + K_3^2 - 2K_1K_3\cos\theta \quad (33)$$

so that $KCOM = K \text{ fermi}^{-1}$.

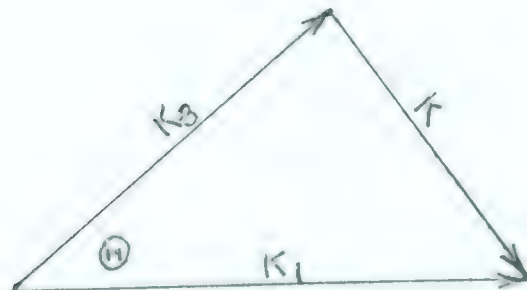


Figure 5: Wave vector diagram.

The final parameter listed in the output is the magnetic rigidity of the light reaction product, M_3 . This is given by

$$BRZ = 56.67(M_3 E_3)^{1/2} \text{ kilogauss-inches} \quad (34)$$

where B is the magnetic field in kilogauss, R the radius of curvature in inches, and Z the electronic charge of M_3 . It was felt that this parameter would be very useful in connection with the broad range spectrograph and spectrometer facility being set up at the University of Alberta.

The computer program for the foregoing was written in FORGO and then compiled in FORTRAN II. The FORGO listing is presented on pages 76 and 77.


```

..IDENT,903165,KINETICS OF NUCLEAR REACTIONS,W.C.OLSEN
C      W.C.OLSEN,903165,KINETICS OF NUCLEAR REACTIONS I
100    FORMAT(55H
1      READ 100
      PUNCH 100
      READ 101,EM1,EM2,EM3,EM4
101    FORMAT(1X4F12.6)
      READ 101,QS
      PUNCH 102,EM1,EM2,EM3,EM4
102    FORMAT(4H0M1=F10.6,3X,3HM2=F10.6,3X,3HM3=F10.6,3X,3HM4=F10.6)
      PUNCH 110,QS
110    FORMAT(4H0QS=F10.6)
      READ 101,E1S,DE1,E1F
      READ 101,THETS,DTHET,THETF
      E1=E1S
2      E1COM=E1*(EM2/(EM1+EM2))**2
      EICOM=E1*(EM2/(EM1+EM2))
      EFCOM=QS+EICOM
      A02=EM1*EM3*E1/(EM1+EM2)**2
      B02=(EM4/(EM3+EM4))*EFCOM
      A0=SQRTF(A02)
      B0=SQRTF(B02)
      A12=EM1*EM4*E1/(EM1+EM2)**2
      B12=(EM3/(EM3+EM4))*EFCOM
      A1=SQRTF(A12)
      B1=SQRTF(B12)
      ROVR0=(EM1**0.33333+EM2**0.33333)
      CAY12=EM1*E1COM/20.908
      CAY1=SQRTF(CAY12)
      CAY32=EM3*B02/20.908
      CAY3=SQRTF(CAY32)
      PUNCH 103,E1,E1COM,EICOM,EFCOM
      PUNCH 104,B02,B12
103    FORMAT(4H0E1=F9.5,3X,6HE1COM=F9.5,3X,6HEICOM=F9.5,3X,6HEFCOM=F9.5)
104    FORMAT(7H0E3COM=F9.5,3X,6HE4COM=F9.5)
      PUNCH 105,CAY1,CAY3,ROVR0
105    FORMAT(4H0K1=F9.5,3X,3HK3=F9.5,3X,10HR OVER R0=F9.5//)
106    FORMAT(3X8HTHETALAB3X8HTHETACOM6X3HPHI8X2HE39X2HE46X10HXSEC-CMTOL)
107    FORMAT(1HI26X4HKCOM6X10HKR OVER R06X3HBRZ//)
      PUNCH 106
      PUNCH 107
      C=B0/A0
      GAM=A0/B0
      IF(1.-C)5,4,3
3      THETF=ATANF(C/SQRTF(1.-C**2))
      GO TO 5
4      THETF=1.5707963
5      THETA=THETS
6      THETL=THETA*57.2957786
      SIND=GAM*SINF(THETA)
      TAND=SIND/SQRTF(1.-SIND**2)
      COMRD=ATANF(TAND)+THETA
      COMTH=COMRD*57.2957786
7      E3=A02+B02+2.*A0*B0*COSF(COMRD)
      E4=A12+B12-2.*A1*B1*COSF(COMRD)
      TANPH=SINF(COMRD)/(A1/B1-COSF(COMRD))

```



```
PHIRD=ATANF(TANPH)
IF(TANPH)8,8,9
8 PHIRD=3.1415927+PHIRD
9 PHI=PHIRD*57.2957786
GAM2=GAM**2
SNTH2=SINF(THETA)**2
SIGR=B02*SQRTF(1.-GAM2*SNTH2)/E3
CAY2=CAY12+CAY32-2.*CAY1*CAY3*COSF(COMRD)
CAY=SQRTF(CAY2)
CAYR=CAY*ROVRO
BRZ=56.67*SQRTF(EM3*E3)
PUNCH 108,THETL,COMTH,PHI,E3,E4,SIGR,CAY,CAYR,BRZ
108 FORMAT(F10.2,2F11.2,2F11.3,F12.4/1HI24XF8.4,F12.4,F14.4)
IF(C-1.)10,13,13
10 COMRD=3.1415927+2.*THETA-COMRD
COMTH=COMRD*57.2957786
E3=A02+B02+2.*A0*B0*COSF(COMRD)
E4=A12+B12-2.*A1*B1*COSF(COMRD)
TANPH=SINF(COMRD)/(A1/B1-COSF(COMRD))
PHIRD=ATANF(TANPH)
IF(TANPH)11,11,12
11 PHIRD=3.1415927+PHIRD
12 PHI=PHIRD*57.2957786
SIGR=B02*SQRTF(1.-GAM2*SNTH2)/E3
CAY2=CAY12+CAY32-2.*CAY1*CAY3*COSF(COMRD)
CAY=SQRTF(CAY2)
CAYR=CAY*ROVRO
BRZ=56.67*SQRTF(EM3*E3)
PUNCH 108,THETL,COMTH,PHI,E3,E4,SIGR,CAY,CAYR,BRZ
13 THETA=THETA+DTHET
IF(THETA-THFTF)6,6,14
14 E1=E1+DF1
IF(E1-E1F)15,15,16
15 PUNCH 109
109 FORMAT(1H2)
GO TO 2
16 PUNCH 109
GO TO 1
END
```


B. Nuclear Reactions II

This program is an extension of Nuclear Reactions I in the sense that it considers those reactions in which the residual nucleus, M_4 , is left in an unbound state which decays, in the reaction plane defined by M_3 and M_4 , into two more particles and/or nuclei, M_5 and M_6 . The coplanar velocity diagram of the final system is shown in Figure 6. The program instructs the computer to determine the laboratory energies and angles of emission, (E_5, γ) and (E_6, β) , of M_5 and M_6 as well as E_3, θ , E_4 and ϕ defined in Nuclear Reactions I. Nuclear Reactions II also determines, for M_5 , the angles of emission, ψ , in the center of mass system of M_4 corresponding to the angles γ , and the ratio of the cross section in the center of mass of M_4 to that in the laboratory system.

Input Data

Seven standard, 80 column IBM cards are required to accommodate one set of input data for this program. Table 4 indicates the contents of each card. Any number of sets of data may be stacked together, each separated by cards 8 and 9 of Table 4.

Output

A typical output page is shown in Figure 7a for the reaction $B^{11}(d,n)C^{12*}(9.64) \rightarrow \alpha + Be^8(0)$. The listing is self-explanatory except perhaps for the following symbols:

B11(D,N)C12(9.64) TO ALPHA PLUS BE8(0)

M1= 2.014742 M2= 11.012805 M3= 1.008986

M4= 12.003815 M5= 4.003876 M6= 8.007853

QS= 4.091000 OR= 2.270000

E1= 1.500000

THETA= 0.00 THETA-COM= 0.00 E3= 5.557

PHI= 179.99 E4= .033

GAMMA	PSI	E5	XSEC-CMTOL	BETA	E6
.02	-179.99	1.265	1.195	180.03	1.037
10.92	-169.99	1.269	1.192	188.54	1.033
21.82	-159.99	1.281	1.180	197.11	1.022
32.64	-149.99	1.300	1.162	205.73	1.003
43.36	-139.99	1.326	1.139	214.44	.977
53.96	-129.99	1.357	1.111	223.26	.945
64.42	-119.99	1.394	1.081	232.22	.908
74.73	-109.99	1.435	1.050	241.36	.867
84.88	-99.99	1.479	1.019	250.70	.823
94.89	-89.99	1.524	.989	260.28	.778
104.74	-79.99	1.569	.960	270.14	.733
114.46	-69.99	1.613	.935	280.30	.690
124.06	-59.99	1.653	.912	290.79	.649
133.55	-49.99	1.690	.893	301.61	.612
142.95	-39.99	1.722	.877	312.78	.580
152.28	-29.99	1.748	.864	324.26	.554
161.55	-19.99	1.767	.855	336.00	.535
170.78	-9.99	1.779	.850	347.95	.523
180.05	0.00	1.783	.848	0.00	.519
189.21	10.00	1.779	.850	12.04	.523
198.44	20.00	1.767	.855	23.99	.535
207.71	30.00	1.748	.864	35.73	.554
217.04	40.00	1.722	.877	47.21	.580
226.44	50.00	1.690	.893	58.38	.612
235.93	60.00	1.653	.912	69.20	.649
245.53	70.00	1.613	.935	79.69	.690
255.25	80.00	1.569	.960	89.85	.733
265.10	90.00	1.524	.989	99.71	.778
275.11	100.00	1.479	1.019	109.29	.823
285.26	110.00	1.435	1.050	118.63	.867
295.57	120.00	1.394	1.081	127.77	.908
306.03	130.00	1.357	1.111	136.73	.945
316.63	140.00	1.326	1.139	145.55	.977
327.35	150.00	1.300	1.162	154.26	1.003
338.17	160.00	1.281	1.180	162.88	1.022
349.07	170.00	1.269	1.192	171.45	1.033
359.97	180.00	1.265	1.195	179.96	1.037

THETA= 44.99 THETA-COM= 47.44 E3= 5.364

PHI= 86.82 E4= .226

GAMMA	PSI	E5	XSEC-CMTOL	BETA	E6
-93.15	-225.73	.913	1.657	86.85	1.583
-80.33	-215.73	.923	1.637	93.73	1.573
-67.65	-205.73	.953	1.579	100.68	1.542
-55.20	-195.73	1.003	1.493	107.67	1.492
-43.35	-185.73	1.071	1.392	114.75	1.425
-31.88	-175.73	1.154	1.285	121.93	1.341
-20.89	-165.73	1.250	1.182	129.27	1.245
-10.38	-155.73	1.357	1.086	136.82	1.138
-.29	-145.73	1.471	1.002	144.62	1.024
9.40	-135.73	1.588	.929	152.75	.907
18.77	-125.73	1.706	.867	161.33	.790
27.85	-115.73	1.819	.816	170.47	.676
36.68	-105.73	1.926	.773	180.35	.569
45.32	-95.73	2.023	.739	191.19	.473
53.80	-85.73	2.106	.713	203.25	.389
62.16	-75.73	2.173	.693	216.81	.322
70.43	-65.73	2.223	.679	232.07	.272
78.64	-55.73	2.254	.670	248.94	.242
86.85	-45.73	2.264	.668	-93.13	.231
95.00	-35.73	2.254	.670	-75.29	.242
103.21	-25.73	2.223	.679	-58.43	.272
111.47	-15.73	2.173	.693	-43.17	.322
119.83	-5.73	2.106	.713	-29.60	.389
128.31	4.26	2.023	.739	-17.54	.473
136.95	14.26	1.926	.773	-6.71	.569
145.79	24.26	1.819	.816	3.16	.676
154.87	34.26	1.706	.867	12.30	.790
164.23	44.26	1.588	.929	20.88	.907
173.93	54.26	1.471	1.002	29.02	1.024
184.02	64.26	1.357	1.086	36.82	1.138
194.54	74.26	1.250	1.182	44.36	1.245
205.52	84.26	1.154	1.285	51.70	1.341
217.00	94.26	1.071	1.392	58.89	1.425
228.94	104.26	1.003	1.493	65.96	1.492
241.30	114.26	.953	1.579	72.96	1.542
253.97	124.26	.923	1.637	79.90	1.573
266.80	134.26	.913	1.657	86.79	1.583

Figure 7a (continued)

B11(D,N)C12(11.83) TO ALPHA + BE8(0)

M1= 2.014742 M2= 11.012805 M3= 1.008986

M4= 12.003815 M5= 4.003876 M6= 8.007853

QS= 1.901000 QB= 4.460000

E1= 1.500000

THETA= 0.00 THETA-COM= 0.00 E3= 3.399

PHI= 179.99 E4= .001

GAMMA	PSI	E5	XSEC-CMTOL	BETA	E6
0.00	-179.99	2.907	1.022	180.07	1.553
10.11	-169.99	2.908	1.022	189.78	1.552
20.22	-159.99	2.911	1.021	199.57	1.549
30.32	-149.99	2.916	1.019	209.37	1.544
40.41	-139.99	2.922	1.017	219.19	1.538
50.49	-129.99	2.930	1.014	229.03	1.530
60.55	-119.99	2.940	1.011	238.90	1.520
70.60	-109.99	2.950	1.007	248.80	1.510
80.63	-99.99	2.962	1.003	258.74	1.498
90.64	-89.99	2.973	.999	268.71	1.487
100.62	-79.99	2.985	.995	278.73	1.475
110.59	-69.99	2.996	.992	288.78	1.464
120.55	-59.99	3.006	.988	298.87	1.454
130.48	-49.99	3.016	.985	309.00	1.444
140.40	-39.99	3.024	.983	319.16	1.436
150.31	-29.99	3.031	.980	329.34	1.429
160.21	-19.99	3.036	.979	339.55	1.424
170.10	-9.99	3.039	.978	349.77	1.421
180.12	0.00	3.040	.978	.06	1.420
189.89	10.00	3.039	.978	10.22	1.421
199.78	20.00	3.036	.979	20.44	1.424
209.68	30.00	3.031	.980	30.65	1.429
219.59	40.00	3.024	.983	40.83	1.436
229.51	50.00	3.016	.985	50.99	1.444
239.44	60.00	3.006	.988	61.12	1.454
249.40	70.00	2.996	.992	71.21	1.464
259.37	80.00	2.985	.995	81.26	1.475
269.35	90.00	2.973	.999	91.28	1.487
279.36	100.00	2.962	1.003	101.25	1.498
289.39	110.00	2.950	1.007	111.19	1.510
299.44	120.00	2.940	1.011	121.09	1.520
309.50	130.00	2.930	1.014	130.96	1.530
319.58	140.00	2.922	1.017	140.80	1.538
329.67	150.00	2.916	1.019	150.62	1.544
339.77	160.00	2.911	1.021	160.42	1.549
349.88	170.00	2.908	1.022	170.21	1.552
359.99	180.00	2.907	1.022	179.92	1.553

Figure 7b

THETA= 44.99 THETA-COM= 48.17 E3= 3.246

PHI= 70.36 E4= .153

GAMMA	PSI	E5	XSEC-CMTOL	BETA	E6
-109.61	-241.45	2.243	1.325	70.39	2.370
-98.13	-231.45	2.255	1.317	78.29	2.358
-86.69	-221.45	2.290	1.296	86.24	2.323
-75.39	-211.45	2.348	1.262	94.25	2.265
-64.27	-201.45	2.426	1.220	102.36	2.187
-53.36	-191.45	2.522	1.171	110.59	2.091
-42.69	-181.45	2.634	1.120	118.99	1.979
-32.26	-171.45	2.757	1.069	127.60	1.856
-22.09	-161.45	2.889	1.020	136.46	1.724
-12.15	-151.45	3.024	.974	145.64	1.589
-2.42	-141.45	3.160	.933	155.19	1.453
7.10	-131.45	3.291	.897	165.18	1.322
16.45	-121.45	3.415	.865	175.68	1.198
25.66	-111.45	3.526	.839	186.75	1.087
34.75	-101.45	3.623	.818	198.42	.990
43.74	-91.45	3.701	.801	210.71	.912
52.65	-81.45	3.758	.790	223.56	.855
61.52	-71.45	3.793	.783	236.84	.819
70.39	-61.45	3.805	.781	-109.60	.808
79.20	-51.45	3.793	.783	-96.11	.819
88.07	-41.45	3.758	.790	-82.82	.855
96.99	-31.45	3.701	.801	-69.98	.912
105.97	-21.45	3.623	.818	-57.69	.990
115.06	-11.45	3.526	.839	-46.02	1.087
124.27	-1.45	3.415	.865	-34.95	1.198
133.62	8.54	3.291	.897	-24.45	1.322
143.15	18.54	3.160	.933	-14.46	1.453
152.88	28.54	3.024	.974	-4.91	1.589
162.82	38.54	2.889	1.020	4.26	1.724
173.00	48.54	2.757	1.069	13.12	1.856
183.42	58.54	2.634	1.120	21.73	1.979
194.09	68.54	2.522	1.171	30.13	2.091
205.00	78.54	2.426	1.220	38.36	2.187
216.12	88.54	2.348	1.262	46.47	2.265
227.43	98.54	2.290	1.296	54.48	2.323
238.86	108.54	2.255	1.317	62.44	2.358
250.34	118.54	2.243	1.325	70.33	2.370

Figure 7b (continued)

B11(D,N)C12(11.83) TO ALPHA + BE8(2.9)

M1= 2.014742 M2= 11.012805 M3= 1.008986

M4= 12.003815 M5= 4.003876 M6= 8.007853

QS= 1.901000 QB= 1.560000

E1= 1.500000

THETA= 0.00 THETA-COM= 0.00 E3= 3.399

PHI= 179.99 E4= .001

GAMMA	PSI	E5	XSEC-CMTOL	BETA	E6
0.00	-179.99	1.001	1.038	180.05	.560
10.19	-169.99	1.001	1.038	189.63	.559
20.37	-159.99	1.003	1.036	199.28	.557
30.55	-149.99	1.006	1.033	208.95	.554
40.70	-139.99	1.010	1.029	218.64	.550
50.83	-129.99	1.015	1.024	228.38	.546
60.94	-119.99	1.020	1.018	238.15	.540
71.02	-109.99	1.026	1.012	247.99	.534
81.06	-99.99	1.033	1.006	257.88	.527
91.08	-89.99	1.040	.999	267.83	.520
101.06	-79.99	1.047	.992	277.85	.513
111.01	-69.99	1.053	.986	287.93	.507
120.92	-59.99	1.060	.980	298.08	.501
130.81	-49.99	1.065	.975	308.30	.495
140.68	-39.99	1.070	.971	318.56	.490
150.53	-29.99	1.074	.967	328.88	.486
160.36	-19.99	1.077	.965	339.23	.483
170.18	-9.99	1.079	.963	349.60	.482
180.14	0.00	1.079	.963	0.00	.481
189.81	10.00	1.079	.963	10.39	.482
199.63	20.00	1.077	.965	20.76	.483
209.46	30.00	1.074	.967	31.11	.486
219.31	40.00	1.070	.971	41.43	.490
229.18	50.00	1.065	.975	51.69	.495
239.07	60.00	1.060	.980	61.91	.501
248.98	70.00	1.053	.986	72.06	.507
258.93	80.00	1.047	.992	82.14	.513
268.91	90.00	1.040	.999	92.16	.520
278.93	100.00	1.033	1.006	102.11	.527
288.97	110.00	1.026	1.012	112.00	.534
299.05	120.00	1.020	1.018	121.84	.540
309.16	130.00	1.015	1.024	131.61	.546
319.29	140.00	1.010	1.029	141.35	.550
329.44	150.00	1.006	1.033	151.04	.554
339.62	160.00	1.003	1.036	160.71	.557
349.80	170.00	1.001	1.038	170.36	.559
359.99	180.00	1.001	1.038	179.94	.560

Figure 7c

THETA= 44.99 THETA-COM= 48.17 E3= 3.246

PHI= 70.36 E4= .153

GAMMA	PSI	E5	XSEC-CMTOL	BETA	E6
-109.63	-241.45	.629	1.652	70.38	1.084
-96.80	-231.45	.636	1.632	77.29	1.077
-84.15	-221.45	.657	1.575	84.24	1.056
-71.80	-211.45	.691	1.490	91.25	1.022
-59.87	-201.45	.737	1.389	98.33	.976
-48.40	-191.45	.794	1.284	105.53	.919
-37.42	-181.45	.860	1.181	112.89	.853
-26.90	-171.45	.933	1.086	120.44	.780
-16.81	-161.45	1.011	1.002	128.26	.702
-7.11	-151.45	1.091	.930	136.41	.622
2.25	-141.45	1.171	.868	145.00	.542
11.34	-131.45	1.249	.817	154.15	.464
20.18	-121.45	1.322	.774	164.05	.391
28.83	-111.45	1.388	.740	174.89	.325
37.32	-101.45	1.445	.714	186.96	.268
45.68	-91.45	1.491	.694	200.51	.222
53.96	-81.45	1.525	.680	215.74	.188
62.17	-71.45	1.546	.672	232.55	.167
70.39	-61.45	1.552	.669	-109.60	.160
78.55	-51.45	1.546	.672	-91.82	.167
86.76	-41.45	1.525	.680	-75.01	.188
95.04	-31.45	1.491	.694	-59.78	.222
103.40	-21.45	1.445	.714	-46.22	.268
111.89	-11.45	1.388	.740	-34.16	.325
120.54	-1.45	1.322	.774	-23.31	.391
129.38	8.54	1.249	.817	-13.42	.464
138.47	18.54	1.171	.868	-4.27	.542
147.84	28.54	1.091	.930	4.31	.622
157.54	38.54	1.011	1.002	12.47	.702
167.63	48.54	.933	1.086	20.28	.780
178.15	58.54	.860	1.181	27.84	.853
189.13	68.54	.794	1.284	35.19	.919
200.60	78.54	.737	1.389	42.39	.976
212.53	88.54	.691	1.490	49.47	1.022
224.88	98.54	.657	1.575	56.48	1.056
237.53	108.54	.636	1.632	63.43	1.077
250.36	118.54	.629	1.652	70.34	1.084

Figure 7c (continued)

B11(D,N)C12(12.71) TO ALPHA + BE8(0)

M1= 2.014742 M2= 11.012805 M3= 1.008986

M4= 12.003815 M5= 4.003876 M6= 8.007853

QS= 1.021000 QB= 5.340000

E1= 1.500000

THETA= 0.00 THETA-COM= 0.00 E3= 2.519

PHI= 179.99 E4= .001

GAMMA	PSI	E5	XSEC-CMTOL	BETA	E6
0.00	-179.99	3.471	1.025	180.12	1.870
10.12	-169.99	3.472	1.025	189.75	1.869
20.24	-159.99	3.476	1.024	199.51	1.865
30.36	-149.99	3.483	1.022	209.29	1.858
40.46	-139.99	3.492	1.019	219.09	1.849
50.55	-129.99	3.503	1.016	228.91	1.838
60.62	-119.99	3.515	1.012	238.76	1.825
70.67	-109.99	3.529	1.008	248.65	1.811
80.71	-99.99	3.545	1.004	258.58	1.796
90.71	-89.99	3.560	.999	268.56	1.781
100.70	-79.99	3.576	.995	278.57	1.765
110.67	-69.99	3.591	.991	288.63	1.750
120.61	-59.99	3.605	.987	298.73	1.736
130.54	-49.99	3.618	.983	308.87	1.723
140.45	-39.99	3.629	.980	319.05	1.712
150.35	-29.99	3.638	.978	329.26	1.703
160.24	-19.99	3.644	.976	339.49	1.697
170.12	-9.99	3.648	.975	349.74	1.693
180.13	0.00	3.650	.975	0.00	1.691
189.87	10.00	3.648	.975	10.25	1.693
199.75	20.00	3.644	.976	20.50	1.697
209.64	30.00	3.638	.978	30.73	1.703
219.54	40.00	3.629	.980	40.94	1.712
229.45	50.00	3.618	.983	51.12	1.723
239.38	60.00	3.605	.987	61.26	1.736
249.32	70.00	3.591	.991	71.36	1.750
259.29	80.00	3.576	.995	81.42	1.765
269.28	90.00	3.560	.999	91.43	1.781
279.28	100.00	3.545	1.004	101.41	1.796
289.32	110.00	3.529	1.008	111.34	1.811
299.37	120.00	3.515	1.012	121.23	1.825
309.44	130.00	3.503	1.016	131.08	1.838
319.53	140.00	3.492	1.019	140.90	1.849
329.63	150.00	3.483	1.022	150.70	1.858
339.75	160.00	3.476	1.024	160.48	1.865
349.87	170.00	3.472	1.025	170.24	1.869
359.99	180.00	3.471	1.025	179.87	1.870

Figure 7d

THETA= 44.99 THETA-COM= 48.73 E3= 2.386

PHI= 59.77 E4= .134

GAMMA	PSI	E5	XSEC-CMTOL	BETA	E6
-120.22	-251.48	2.806	1.268	59.81	2.668
-108.96	-241.48	2.818	1.262	67.94	2.656
-97.76	-231.48	2.854	1.246	76.14	2.620
-86.66	-221.48	2.913	1.219	84.40	2.561
-75.71	-211.48	2.992	1.185	92.75	2.481
-64.93	-201.48	3.091	1.146	101.23	2.383
-54.34	-191.48	3.205	1.104	109.86	2.268
-43.96	-181.48	3.331	1.062	118.69	2.142
-33.79	-171.48	3.466	1.020	127.76	2.008
-23.82	-161.48	3.604	.981	137.12	1.869
-14.03	-151.48	3.743	.945	146.82	1.730
-4.42	-141.48	3.878	.913	156.91	1.596
5.03	-131.48	4.004	.885	167.43	1.470
14.35	-121.48	4.118	.861	178.41	1.356
23.57	-111.48	4.216	.842	189.89	1.257
32.70	-101.48	4.296	.827	201.84	1.177
41.76	-91.48	4.355	.816	214.22	1.118
50.78	-81.48	4.391	.810	226.91	1.082
59.81	-71.48	4.403	.808	-120.22	1.070
68.77	-61.48	4.391	.810	-107.36	1.082
77.78	-51.48	4.355	.816	-94.66	1.118
86.84	-41.48	4.296	.827	-82.29	1.177
95.97	-31.48	4.216	.842	-70.34	1.257
105.19	-21.48	4.118	.861	-58.86	1.356
114.51	-11.48	4.004	.885	-47.87	1.470
123.97	-1.48	3.878	.913	-37.35	1.596
133.59	8.51	3.743	.945	-27.27	1.730
143.37	18.51	3.604	.981	-17.57	1.869
153.34	28.51	3.466	1.020	-8.21	2.008
163.51	38.51	3.331	1.062	.85	2.142
173.89	48.51	3.205	1.104	9.68	2.268
184.48	58.51	3.091	1.146	18.31	2.383
195.26	68.51	2.992	1.185	26.79	2.481
206.22	78.51	2.913	1.219	35.14	2.561
217.32	88.51	2.854	1.246	43.40	2.620
228.52	98.51	2.818	1.262	51.60	2.656
239.77	108.51	2.806	1.268	59.73	2.668

Figure 7d (continued)

B11(D,N)C12(12.71) TO ALPHA + 91.12.1)

M1= 2.014742 M2= 11.012805 M3= 1.008986

M4= 12.003815 M5= 4.003876 M6= 8.007853

QS= 1.021000 QB= 2.440000

E1= 1.500000

THETA= 0.00 THETA-COM= 0.00 E3= 2.519

PHI= 179.99 E4= .001

GAMMA	PSI	E5	XSEC-CMTOL	BETA	E6
0.00	-179.99	1.566	1.038	180.01	.874
10.18	-169.99	1.567	1.037	189.64	.873
20.37	-159.99	1.570	1.035	199.29	.871
30.54	-149.99	1.574	1.032	208.96	.866
40.69	-139.99	1.580	1.028	218.66	.860
50.82	-129.99	1.588	1.024	228.40	.853
60.93	-119.99	1.597	1.018	238.19	.844
71.00	-109.99	1.606	1.012	248.02	.835
81.05	-99.99	1.616	1.005	257.91	.824
91.06	-89.99	1.627	.999	267.87	.814
101.04	-79.99	1.637	.993	277.89	.803
110.99	-69.99	1.647	.986	287.97	.793
120.91	-59.99	1.657	.981	298.12	.784
130.80	-49.99	1.666	.976	308.32	.775
140.67	-39.99	1.673	.971	318.59	.768
150.52	-29.99	1.679	.968	328.89	.762
160.35	-19.99	1.684	.965	339.24	.757
170.18	-9.99	1.686	.964	349.61	.754
180.15	0.00	1.687	.963	0.00	.753
189.81	10.00	1.686	.964	10.38	.754
199.64	20.00	1.684	.965	20.75	.757
209.47	30.00	1.679	.968	31.10	.762
219.32	40.00	1.673	.971	41.40	.768
229.19	50.00	1.666	.976	51.67	.775
239.08	60.00	1.657	.981	61.87	.784
249.00	70.00	1.647	.986	72.02	.793
258.95	80.00	1.637	.993	82.10	.803
268.93	90.00	1.627	.999	92.12	.814
278.94	100.00	1.616	1.005	102.08	.824
288.99	110.00	1.606	1.012	111.97	.835
299.06	120.00	1.597	1.018	121.81	.844
309.17	130.00	1.588	1.024	131.59	.853
319.30	140.00	1.580	1.028	141.33	.860
329.45	150.00	1.574	1.032	151.03	.866
339.62	160.00	1.570	1.035	160.70	.871
349.81	170.00	1.567	1.037	170.35	.873
359.99	180.00	1.566	1.038	179.98	.874

Figure 7c

THETA= 44.99 THETA-COM= 48.73 E3= 2.386

PHI= 89.77 E4= .134

GAMMA	PSI	E5	XSEC-CMTOL	BETA	E6
-120.22	-251.48	1.131	1.437	59.79	1.442
-108.25	-241.48	1.139	1.426	67.28	1.434
-96.37	-231.48	1.164	1.394	74.83	1.410
-84.68	-221.48	1.203	1.344	82.43	1.370
-73.25	-211.48	1.257	1.283	90.12	1.316
-62.12	-201.48	1.324	1.215	97.94	1.250
-51.31	-191.48	1.401	1.146	105.92	1.172
-40.83	-181.48	1.486	1.079	114.12	1.087
-30.67	-171.48	1.577	1.015	122.60	.996
-20.80	-161.48	1.671	.960	131.41	.902
-11.19	-151.48	1.765	.910	140.64	.809
-1.82	-141.48	1.856	.866	150.39	.718
7.33	-131.48	1.941	.830	160.75	.632
16.32	-121.48	2.018	.800	171.86	.555
25.18	-111.48	2.085	.776	183.80	.489
33.92	-101.48	2.139	.758	196.66	.435
42.58	-91.48	2.178	.745	210.40	.395
51.19	-81.48	2.203	.738	224.88	.371
59.82	-71.48	2.211	.735	-120.22	.362
68.35	-61.48	2.203	.738	-105.32	.371
76.96	-51.48	2.178	.745	-90.85	.395
85.62	-41.48	2.139	.758	-77.11	.435
94.36	-31.48	2.085	.776	-64.25	.489
103.22	-21.48	2.018	.800	-52.31	.555
112.21	-11.48	1.941	.830	-41.20	.632
121.38	-1.48	1.856	.866	-30.83	.718
130.74	8.51	1.765	.910	-21.09	.809
140.35	18.51	1.671	.960	-11.86	.902
150.22	28.51	1.577	1.016	-3.04	.996
160.38	38.51	1.486	1.079	5.42	1.087
170.86	48.51	1.401	1.146	13.62	1.172
181.67	58.51	1.324	1.215	21.61	1.250
192.80	68.51	1.257	1.283	29.43	1.316
204.24	78.51	1.203	1.344	37.12	1.370
215.92	88.51	1.164	1.394	44.72	1.410
227.80	98.51	1.139	1.426	52.26	1.434
239.77	108.51	1.131	1.437	59.75	1.442

Figure 7c (continued)

Table 4

Card No.	Symbol	Definition	Begins At Column	Units
1		This is the Title Card. The first 55 columns, beginning at column 2, are available. Any notation to identify the reaction is permitted.	2	
2	EM1	The mass of the bombarding particle, M_1	2	amu
	EM2	The mass of the target nucleus, M_2	14	amu
	EM3	The mass of the primary, light reaction product, M_3	26	amu
3	EM4	The mass of the primary residual nucleus, M_4	2	amu
	EM5	The mass of the secondary, light reaction product, M_5	14	amu
	EM6	The mass of the secondary, heavy reaction product, M_6	26	amu
4	QS	The Q of the primary reaction to the excited state, S, of the M_4 nucleus	2	Mev
	QB	The disintegration energy of the secondary reaction in which M_4 breaks up into M_5 and M_6	14	
5	THETS	The starting, or initial laboratory angle of emission, θ , of M_3	2	rad
	DTHET	The increment in θ	14	rad
	THETF	The final or maximum angle, θ , of interest	26	rad

Table 4 (cont'd)

Card No.	Symbol	Definition	Begins At Column	Units
6	ROST	The starting angle of emission, ρ , of M_5 measured with respect to the laboratory direction of the residual nucleus, M_4 , as shown in Figure 5. This is usually zero.	2	rad.
	DRO	The increment in the angle ρ .	14	rad.
	ROF	The final or largest value of ρ of interest. This is usually 2π .	26	rad.
7	E1S	The initial value of the bombarding energy of M_1	2	Mev
	DE1	The increment in E1	14	Mev
	E1F	The final value of the bombarding energy of M_1	26	Mev
8		..I	1	
9		..BRANCH 0040R	1	

- i. THETA-COM. This is the center of mass angle, θ , corresponding to θ .
- ii. XSEC-CMTOL. This is the notation used for the ratio of the cross section for M_5 in the center of mass system of M_4 to that in the laboratory system.

All mass values are in amu, all angles in degrees, and all energies in Mev.

Kinematics

The kinetic energies of the products of the secondary reaction are, in the center of mass system of M_4 ,

$$E_5^P = \frac{M_6}{(M_5 + M_6)} Q_B, \text{ for } M_5, \quad (34)$$

and

$$E_6^P = \frac{M_5}{(M_5 + M_6)} Q_B, \text{ for } M_6, \quad (35)$$

where Q_B is the disintegration energy of the secondary process.

Expressions for the laboratory energies of M_5 and M_6 can be derived with the help of Figure 6. Applying the law of cosines to the velocity triangle bounded by v_4 , v_5 , and V_5 one gets

$$v_5^2 = v_4^2 + V_5^2 - 2v_4V_5\cos\phi, \quad (36)$$

and upon multiplying through by $M_5/2$

$$E_5 = E_5^F + E_5^P - 2(E_5^F \cdot E_5^P)^{1/2} \cos\phi \quad (37)$$

where

v_5 = the laboratory velocity of M_5

V_5 = the velocity of M_5 in the center of mass system of M_4

$$E_5^F = (M_5/M_4)E_4.$$

E_4 is given by equation (14).

Considering the triangle bounded by the velocities v_4 , v_6 , and

V_6 of Figure 6 and again applying the cosine law, one gets

$$v_6^2 = v_4^2 + V_6^2 + 2v_4V_6\cos\rho \quad (38)$$

and by multiplying through by $M_6/2$

$$E_6 = E_6^F + E_6^P + 2(E_6^F \cdot E_6^P)^{1/2}\cos\rho \quad (39)$$

where

$$\begin{aligned} v_6 &= \text{the laboratory velocity of } M_6 \\ V_6 &= \text{the velocity of } M_6 \text{ in the center of mass} \\ &\quad \text{system of } M_4 \\ E_6^F &= (M_6/M_4)E_4 \end{aligned}$$

Equations (37) and (39) are used to calculate E_5 and E_6 as functions of the angle, ρ , between v_4 and V_5 .

It is worth noting here that ρ is an arbitrary angle which forms part of the input data, and which varies from zero to 360° in small increments of 10 or 15° , say.

The angles of emission of M_5 and M_6 can be determined by first calculating the values of δ and ϵ for each value of ρ . A convenient expression for δ in terms of previously determined quantities is

$$\cos\delta = \frac{(E_5 + E_5^F - E_5^P)}{2(E_5 \cdot E_5^F)^{1/2}} \quad (40)$$

For computer convenience δ is denoted by DL in the program.

For $\rho \leq \pi$, the laboratory emission angle of M_5 , γ , is given by

$$\gamma = \phi - \delta \quad (41)$$

and for $\sigma > \pi$,

$$\gamma = \phi + \delta, \quad (42)$$

Epsilon, the angle between v_4 and v_6 , is given by

$$\cos \epsilon = \frac{(E_6 + E_6^F - E_6^P)}{2(E_6 \cdot E_6^F)^{1/2}}. \quad (43)$$

For $\rho \leq \pi$, the laboratory emission angle of M_6 , β , is given by

$$\beta = \phi + \epsilon \quad (44)$$

and for $\rho > \pi$,

$$\beta = \phi - \epsilon. \quad (45)$$

The Center of Mass Correction for M_5

Consider the laboratory system of coordinates (x,y,z) of velocity space as having its z-axis in the laboratory direction of residual nucleus, M_4 , of the primary reaction. That is, the z-axis makes an angle ϕ with the direction of the incident beam of bombarding particles. And let the coordinate system (x', y', z') in which M_4 is at rest have its origin at the end of the velocity vector \vec{v}_4 , and its z'-axis in the direction of the velocity of M_4 in the center of mass system of the primary reaction (i.e., \vec{v}_4). These two coordinate systems are shown in Figure 6. This choice of the z'-axis is convenient when considering the angular distribution of particles from the breakup of levels formed in a stripping

reaction, for example, the $B^{11}(d,n)C^{12*}$ reaction. If pure Butler theory applies, the angular distribution of the α -particles from the decay of C^{12} leading to states in Be^8 will be symmetric about the direction of the captured proton; that is, about the z' -axis.

The primed system is related to the unprimed system by a translation, \vec{v}_4 , and a rotation of $\alpha = (\pi - \theta - \phi)$, both in the (y,z) plane, the plane of the primary reaction. If (δ, η) and (ψ, ν) are the polar and azimuthal angles in the unprimed and primed systems respectively, the transformation equations are

$$V_5 \sin \psi \cos \nu = v_5 \sin \delta \cos \eta \quad (46a)$$

$$V_5 \sin \psi \sin \nu = v_5 \sin \delta \sin \eta \cos \alpha - (v_5 \cos \delta - v_4) \sin \alpha \quad (46b)$$

$$V_5 \cos \psi = v_5 \sin \delta \sin \eta \sin \alpha + (v_5 \cos \delta - v_4) \cos \alpha. \quad (46c)$$

The total number of particles, M_5 , detected is the same in both systems. Therefore,

$$\sigma(\delta) \sin \delta d\delta d\eta = \sigma(\psi) \sin \psi d\psi d\nu \quad (47)$$

where $\sigma(\delta)$ and $\sigma(\psi)$ are the cross sections for the production of M_5 in the laboratory (unprimed) system and the center of mass system (primed) of M_4 respectively. The required correction factor is given by

$$\frac{\sigma(\psi)}{\sigma(\delta)} = \frac{\sin \delta}{\sin \psi} \frac{d\delta d\eta}{d\psi d\nu}. \quad (48)$$

Now,
$$d\delta = \frac{\partial \delta}{\partial V_5} dV_5 + \frac{\partial \delta}{\partial \psi} d\psi + \frac{\partial \delta}{\partial v} dv \quad (49)$$

and
$$d\eta = \frac{\partial \eta}{\partial V_5} dV_5 + \frac{\partial \eta}{\partial \psi} d\psi + \frac{\partial \eta}{\partial v} dv . \quad (50)$$

V_5 is a constant quantity and therefore $dV_5 = 0$. The partial derivatives $\partial \delta / \partial v$ and $\partial \eta / \partial v$ can be obtained by differentiating equations (46) partially with respect to v and solving the resulting system of three equations for the derivatives. In a similar manner, by differentiating with respect to ψ , $\partial \delta / \partial \psi$ and $\partial \eta / \partial \psi$ may be determined. The results of these calculations for M_5 confined to the primary reaction plane where $\eta = v = \pm \pi/2$ are:

$$\frac{\partial \delta}{\partial v} = \frac{\partial \eta}{\partial \psi} = 0 , \quad (51)$$

$$\frac{\partial \delta}{\partial \psi} = \frac{V_5}{v_5} \cos(\psi - \delta \pm \alpha) , \quad (52)$$

and
$$\frac{\partial \eta}{\partial v} = \frac{V_5}{v_5} \frac{\sin \psi}{\sin \delta} . \quad (53)$$

In equation (52), the plus sign corresponds to $\eta = v = + \pi/2$ and the minus sign to $\eta = v = -\pi/2$.

The cross section ratio, equation (48), can now be rewritten as

$$\frac{\sigma(\psi)}{\sigma(\delta)} = \frac{\sin \delta}{\sin \psi} \frac{\partial \delta}{\partial \psi} \frac{\partial \eta}{\partial v} , \quad (54a)$$

$$= \left[\frac{V_5}{v_5} \right]^2 \cos(\psi - \delta \pm \alpha) \quad (54b)$$

From Figure 6 it can be seen that in terms of the arbitrary angle ρ , and for $\eta = \nu = \pi/2$, ψ is given by

$$\psi_{\pi/2} = \rho + \theta + \phi - 2\pi \quad (55)$$

For $\eta = \nu = -\pi/2$, $\psi_{-\pi/2} = -\psi_{\pi/2}$. In the computer program, ψ is computed from equation (55) only. Hence positive and negative values of ψ correspond to cases when η and ν are $+\pi/2$ and $-\pi/2$ respectively. Absolute value signs around ψ in equation (54b) are required to eliminate this distinction.

From the point of view of programming convenience, it is desirable to have an expression for the cross section ratio in terms of the arbitrary angle ρ . Such an expression can easily be obtained by noting that

$$\frac{\partial \delta}{\partial \psi} = \frac{\partial \delta}{\partial \rho} \frac{\partial \rho}{\partial \psi} = \frac{\partial \delta}{\partial \rho} \quad (56)$$

since $\partial \rho / \partial \psi = 1$ from equation (55), and that, from Figure 6,

$$\sin \delta = - \left[\frac{v_5}{V_5} \right] \sin \rho \quad (57)$$

Hence
$$\delta = \text{ArcSin}\{-(E_5 P / E_5)^{1/2} \sin \rho\} \quad (58)$$

Differentiating this expression with respect to ρ , one obtains

$$\frac{\partial \delta}{\partial \rho} = \left[\frac{E_5 P}{1 - \frac{E_5 P}{E_5} \sin^2 \rho} \right]^{1/2} \frac{\sin \rho \frac{\partial}{\partial \rho} \sqrt{E_5} - \sqrt{E_5} \cos \rho}{E_5} \quad (59)$$

Using equation (37) for E_5 ,

$$\frac{\partial \sqrt{E_5}}{\partial \rho} = \frac{\sqrt{E_5 P \cdot E_5 F}}{\sqrt{E_5}} \sin \rho \quad (60)$$

$$\text{Hence, } \frac{\partial \delta}{\partial \rho} = \frac{\partial \delta}{\partial \psi} = \left[\frac{E_5 P}{1 - \frac{E_5 P}{E_5} \sin^2 \rho} \right]^{1/2} \frac{\sqrt{E_5 P \cdot E_5 F} \sin^2 \rho - E_5 \cos \rho}{(E_5)^{3/2}} \quad (61)$$

Substitution of equation (61) for $\partial \delta / \partial \rho$ and equation (53) for $\partial \eta / \partial \nu$ at $\eta = \nu = \pm \pi/2$ into equation (54a) gives

$$\frac{\sigma(\psi)}{\sigma(\delta)} = \frac{E_5 P}{(E_5)^2} \frac{|\sqrt{E_5 P \cdot E_5 F} \sin^2 \rho - E_5 \cos \rho|}{[1 - (E_5 P / E_5) \sin^2 \rho]^{1/2}} \quad (62)$$

Equation (62) is used to calculate the cross section ratio for each value of the angle ρ . The results are tabulated under the column heading XSEC-CMTOL. The absolute value of the binomial term is taken since negative values of this ratio are unphysical.

The program was written in FORGO and compiled in FORTRAN II. Five minutes of computer time are required to produce the output for one bombarding energy value (E_1) and one angle θ , for ρ varying from 0 to 2π in 10° intervals. The listing of the program statements is given on pages 88 and 89.


```
..IDENT,903157,KINETICS OF NUCLEAR REACTIONS,TWO, W.OLSEN
..LOAD FORTRAN DUMP EXECUTE
C      W.OLSEN,903157,KINETICS OF NUCLEAR REACTIONS, II
100    FORMAT(55H
        READ 100
        PUNCH 100
        READ 101,EM1,EM2,EM3,EM4,EM5,EM6
101    FORMAT(1X3F12.6)
        READ 101,QS,QB
        READ 101,THETS,DTHET,THETF
        READ 101,ROST,DRO,ROF
        READ 101,E1S,DE1,E1F
        PUNCH 102,EM1,EM2,EM3
        PUNCH 103,EM4,EM5,EM6
        PUNCH 104,QS,QB
102    FORMAT(4HOM1=F10.6,3X,3HM2=F10.6,3X,3HM3=F10.6)
103    FORMAT(4HOM4=F10.6,3X,3HM5=F10.6,3X,3HM6=F10.6)
104    FORMAT(4HOQS=F10.6,3X,3HQB=F10.6)
        E1=E1S
7      PUNCH 105,E1
105    FORMAT(4HOE1=F10.6)
        AO2=EM1*EM3*E1/(EM1+EM2)**2
        BO2=(EM4/(EM3+EM4))*(QS+EM2*E1/(EM1+EM2))
        AO=SQRTF(AO2)
        BO=SQRTF(BO2)
        THETA=THETS
1      SIND=AO*SINF(THETA)/BO
        TAND=SIND/SQRTF(1.-SIND**2)
        CAPTH=ATANF(TAND)+THETA
        E3=AO2+BO2+2.*AO*BO*COSF(CAPTH)
        A12=EM1*EM4*E1/(EM1+EM2)**2
        B12=(EM3/(EM3+EM4))*(QS+EM2*E1/(EM1+EM2))
        A1=SQRTF(A12)
        B1=SQRTF(B12)
        E4=A12+B12-2.*A1*B1*COSF(CAPTH)
        TANPH=SINF(CAPTH)/(A1/B1-COSF(CAPTH))
        PHIRD=ATANF(TANPH)
        IF(TANPH)2,2,3
2      PHIRD=PHIRD+3.1415927
3      PHI=PHIRD*57.2957786
        THETD=THETA*57.2957786
        COMTH=CAPTH*57.2957786
        PUNCH 106,THETD,COMTH,E3
        PUNCH 107,PHI,E4
106    FORMAT(7H0THETA=F7.2,3X,10HTHETA-COM=F7.2,3X,3HE3=F7.3)
107    FORMAT(5H0PHI=F7.2,3X,3HE4=F7.3//)
108    FORMAT(4X5HGAMMA6X3HPSI8X2HE54X10HXSEC-CMTOL4X4HBETA7X2HE6)
        PUNCH 108
        E5P=EM6*QB/(EM5+EM6)
        E6P=EM5*QB/(EM5+EM6)
        RO=ROST
        E5F=EM5*E4/EM4
4      E5=E5F+E5P-2.*SQRTF(E5F*E5P)*COSF(RO)
        COSDL=(E5+E5F-E5P)/(2.*SQRTF(E5F*E5))
        SNDL2=(1.-COSDL**2)
        IF(SNDL2)8,9,9
```



```
8   SNDL2=0.00000
9   TANDL=SQRTF(SNDL2)/COSDL
   DELTA=ATANF(TANDL)
   IF(TANDL)10,10,11
10  DELTA=DELTA+3.1415927
11  IF(RO-3.1415927)12,12,13
12  GAMRD=PHIRD-DELTA
   GO TO 14
13  GAMRD=PHIRD+DELTA
14  GAMMA=GAMRD*57.2957786
   E6F=E6*E4/E5
   E6=E6F+E6P+2.*SQRTF(E6F*E6P)*COSF(RO)
   COSEP=(E6+E6F-E6P)/(2.*SQRTF(E6*E6F))
   SNEP2=(1.-COSEP**2)
   IF(SNEP2)15,16,16
15  SNEP2=0.00000
16  TANEP=SQRTF(SNEP2)/COSEP
   EP=ATANF(TANEP)
   IF(TANEP)17,17,18
17  EP=EP+3.1415927
18  IF(RO-3.1415927)19,19,20
19  BETRD=PHIRD+EP
   GO TO 21
20  BETRD=PHIRD-EP
21  BETA=BETRD*57.2957786
   PSIRD=RO+CAPTH+PHIRD-6.2831854
   PSI=PSIRD*57.2957786
   SINRO=SINF(RO)
   COSRO=COSF(RO)
   E5R=E5P/E5
   P=E5R/E5
   Q=1./((SQRTF(1.-E5R*SINRO**2)))
   R=ABSF(SQRTF(E5P*E5F)*SINRO**2-E5*COSRO)
   SIGR=P*Q*R
   PUNCH 109,GAMMA,PSI,E5,SIGR,BETA,E6
109  FORMAT(2F10.2,F10.3,F11.3,F10.2,F10.3)
   RO=RO+DRO
   IF(RO-ROF)4,4,6
6   PUNCH 110
110  FORMAT(1H2)
   THETA=THETA+DTHET
   IF(THETA-THETF)1,1,22
22  E1=E1+DE1
   IF(E1-E1F)7,7,23
23  STOP
   END
```




C. Nuclear Reactions III

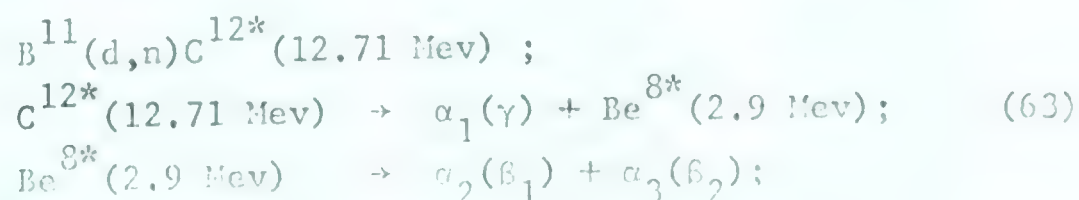
Nuclear Reactions III is again a straightforward extension of Nuclear Reactions II. In this case, M_6 is a nucleus formed in an unbound state by the first two stages of the reaction. It subsequently breaks up into the two particles M_7 and M_8 . It is the purpose of this program to instruct the computer to determine the following quantities for a given value of E_1 and θ : (E_3, θ) , (E_4, ϕ) , (E_5, γ) , E_6 , (E_7, β_1) and (E_8, β_2) . (E_7, β_1) and (E_8, β_2) are the laboratory energies and angles of emission of the particles M_7 and M_8 respectively. The other variables have been defined in the previous programs, and all are shown in the velocity diagram of Figure 8.

Input Data

Six IBM cards comprise a set of input data for this program. Table 5 explains what information each card should contain. The ordering of the cards follows that indicated in the Table. The program must be read in for each set of data.

Output

A typical FORTRAN II output page is shown in Figure 9. The reaction in this example is:



.20147420E+01	.11012805E+02	.10089860E+01	.12003815E+02
.40038760E+01	.80078530E+01	.40038760E+01	.40038760E+01
.15000000E+01	.10210000E+01	.24400000E+01	.29400000E+01
44.999995	48.739826	2.386402	59.776026
			.134334
-120.223970	1.131529	1.442893	
59.776026	.139984	419.776020	4.296890
103.383080	.210805	248.637270	4.226069
130.811330	.418444	257.544880	4.018430
148.730820	.748749	266.551670	3.688125
162.415490	1.179210	275.725230	3.257664
174.039300	1.680493	285.161190	2.756380
184.544640	2.218437	295.007390	2.218437
194.390830	2.756380	305.512730	1.680494
203.826790	3.257663	317.136520	1.179211
213.000350	3.688125	330.821190	.748749
222.007140	4.018430	348.740670	.418444
230.914730	4.226068	376.168860	.210806
59.776026	4.296890	419.776020	.139984
-102.295520	1.149927	1.424495	
-108.883290	.144079	251.053930	4.274397
-65.802533	.214447	79.938570	4.204029
-38.364553	.420758	88.870295	3.997718
-20.350864	.748950	97.902791	3.669526
-6.586573	1.176658	107.104630	3.241818
5.097943	1.674735	116.572870	2.743741
15.650536	2.209238	126.457320	2.209238
25.534986	2.743740	137.009910	1.674736
35.003222	3.241817	148.694420	1.176659
44.205073	3.669525	162.458710	.748951
53.237563	3.997718	180.472370	.420758
62.169288	4.204028	207.910330	.214448
-108.946050	4.274397	250.991170	.144079
-84.688539	1.203869	1.370553	
-97.569576	.156586	262.430410	4.207949
-55.756979	.225610	91.385224	4.138925
-28.320781	.427976	100.389330	3.936559
-10.041554	.749895	109.498860	3.614641
3.954909	1.169427	118.785450	3.195108
15.818819	1.657982	128.350240	2.706553
26.511925	2.182267	138.348900	2.182268
36.510588	2.706552	149.042000	1.657983
46.075373	3.195107	160.905910	1.169428
55.361965	3.614640	174.902360	.749895
64.471495	3.936558	193.181570	.427977
73.475578	4.138925	220.617740	.225610

Figure 9. Sample of Kinematics for the reaction:



Table 5

Card No.	Symbol	Definition	Begins at Column	Units
1	EM1	Mass of M_1	2	amu
1	EM2	Mass of M_2	17	amu
1	EM3	Mass of M_3	32	amu
1	EM4	Mass of M_4	47	amu
2	EM5	Mass of M_5	2	amu
2	EM6	Mass of M_6	17	amu
2	EM7	Mass of M_7	32	amu
2	EM8	Mass of M_8	47	amu
3	ROST	The initial angle of emission ρ of M_5 with respect to the laboratory direction of M_4 . See Figure 8. This is usually zero.	2	radians
3	DRO	The increment in ρ	17	radians
3	ROF	The final angle, ρ ; usually 2π .	32	radians
4	ZETST	The initial angle of emission, ζ , of M_7 with respect to the laboratory direction of M_6 . See Figure 8. This is usually zero.	2	radians
4	DZET	The increment in ζ	17	radians
4	ZETF	The final value of ζ , 180°	32	radians
5	E1	The bombarding energy of M_1	2	Mev
5	QS	The Q of the primary reaction	17	Mev
5	QB	The disintegration energy of M_4	32	Mev
5	QF	The disintegration energy of M_6	47	Mev
6	THETA	The laboratory angle of emission of M_3	2	radians

for $\theta = 45^\circ$ and $E_1 = 1.5$ Mev.

The first two lines consist of the eight mass values, four per line, and the third line consists of the input energies E_1 , Q_S , Q_B , and Q_F . These quantities are in fixed point format. The next line records, from left to right; θ , Θ , E_3 , ϕ , and E_4 . The listing which follows consists of two parts: a line containing the values of γ , E_5 , and E_6 for each value of ρ , followed by four columns of single spaced numbers which correspond to, from left to right; β_1 , E_7 , β_2 , and E_8 . These last four quantities correspond to ζ as it is varied from its minimum to maximum values (0 to π radians in 15° intervals in the above example). This format for the listing is repeated for each value of ρ as it is varied from its minimum to maximum values (0 to 2π in 15° intervals in the above example). Because of the periodicity of the trigonometric functions, β_1 and β_2 are correct to within $\pm n\pi$, where n is an integer. Specifically, in the above example,

$$\begin{aligned}\theta &= 45 \text{ degrees,} \\ E_{\text{neutron}} &= 2.386 \text{ Mev,} \\ \Theta_n &= 48.74 \text{ degrees,} \\ \phi_{C12} &= 59.77 \text{ degrees,} \\ E_{C12} &= 0.134 \text{ Mev,} \\ \gamma_{\alpha_1} &= -120.22 \text{ degrees,} \\ E_{\alpha_1} &= 1.131 \text{ Mev,} \\ E_{Be8} &= 1.443 \text{ Mev,}\end{aligned}$$

and considering the first row only in the listing for M_7 and M_8 ,

$$\beta_1 = 59.77^\circ - \pi = -120.23^\circ, \quad E_{\alpha_2} = 0.139 \text{ Mev}$$

and $\beta_2 = 419.77^\circ - 2\pi = 59.77^\circ, \quad E_{\alpha_3} = 4.297 \text{ Mev.}$

Kinematics

Only the kinematics for the breakup of M_6 need be considered here as the processes leading to the existence of M_6 have been treated previously.

The kinetic energies of M_7 and M_8 in the center of mass of M_6 are

$$E_7^P = \frac{M_8}{(M_7 + M_8)} Q_F \quad (64)$$

for M_7 , and

$$E_8^P = \frac{M_7}{(M_7 + M_8)} Q_F \quad (65)$$

for M_8 , where Q_F is the disintegration energy of M_6 .

An expression for E_7 in terms of the arbitrary (input) angle ζ can be obtained by considering the velocity triangle bounded by v_6 , v_7 , and V_7 (Figure 8). Thus,

$$v_7^2 = v_6^2 + V_7^2 - 2v_6V_7\cos\zeta. \quad (66)$$

Multiplying through by $(M_7/2)$

$$E_7 = E_{7F} + E_7^P - 2(E_{7F} \cdot E_7^P)^{1/2} \cos\zeta, \quad (67)$$

where $E_7^F = (M_7/M_6)E_6$.

A similar expression for E_8 can be obtained by applying the cosine law to the triangle bounded by velocity vectors v_6 , v_8 , and V_8 . Thus,

$$E_8 = E_8^F + E_8^P + 2(E_8^F \cdot E_8^P)^{1/2} \cos \zeta \quad (68)$$

where $E_8^F = (M_8/M_6)E_6$.

The angles of emission of M_7 and M_8 in the laboratory system, β_1 and β_2 respectively, can be determined by first calculating the angles ω and ξ .

$$\cos \omega = \frac{E_7 + E_7^F - E_7^P}{2(E_7 \cdot E_7^F)^{1/2}} \quad (69)$$

and

$$\cos \xi = \frac{E_8 + E_8^F - E_8^P}{2(E_8 \cdot E_8^F)^{1/2}} \quad (70)$$

For programming convenience ξ is denoted XI. Now, for $\rho \leq \pi$

$$\beta_1 = \phi + \epsilon - \omega \quad , \quad (71)$$

and

$$\beta_2 = \phi + \epsilon + \xi \quad , \quad (72)$$

for $\rho > \pi$

$$\beta_1 = \phi - \epsilon - \omega \quad , \quad (73)$$

and

$$\beta_2 = \phi - \epsilon + \xi \quad . \quad (74)$$

The program was written in FORGO and compiled in FORTRAN II.

The computer running time for one set of data as described in the section on the input data is 35 minutes. The listing of the FORGO statements is given on pages 96 and 97.


```

..IDENT 903155,KINETICS OF NUCLEAR REACTIONS,W.OLSEN
..LOAD FORGO CLOCK 7200 ALLOW
C      W.OLSEN,903155=KINETICS OF NUCLEAR REACTIONS III
      READ 100,EM1,EM2,EM3,EM4,EM5,EM6,EM7,EM8
100    FORMAT(1X4E15.8)
      PUNCH 100,EM1,EM2,EM3,EM4,EM5,EM6,EM7,EM8
      READ 100,ROST,DRO,ROF
      READ 100,ZETST,DZET,ZETF
14     READ 100,E1,QS,QB,QF
      READ 100,THETA
      PUNCH 100,E1,QS,QB,QF
      A02=EM1*EM3*E1/(EM1+EM2)**2
      B02=(EM4/(EM3+EM4))*(QS+EM2*E1/(EM1+EM2))
      A0=SQRTF(A02)
      B0=SQRTF(B02)
      SIND=A0*SINF(THETA)/B0
      TAND=SIND/SQRTF(1.-SIND**2)
      CAPTH=ATANF(TAND)+THETA
      E3=A02+B02+2.*A0*B0*COSF(CAPTH)
      A12=EM1*EM4*E1/(EM1+EM2)**2
      B12=(EM3/(EM3+EM4))*(QS+EM2*E1/(EM1+EM2))
      A1=SQRTF(A12)
      B1=SQRTF(B12)
      E4=A12+B12-2.*A1*B1*COSF(CAPTH)
      TANPH=SINF(CAPTH)/(A1/B1-COSF(CAPTH))
      PHIRD=ATANF(TANPH)
      IF(TANPH)1,1,2
1      PHIRD=PHIRD+3.1415927
2      PHI=PHIRD*57.2957786
      THETD=THETA*57.2957786
      COMTH=CAPTH*57.2957786
      PUNCH 101,THETD,COMTH,E3,PHI,E4
101    FORMAT(1H0,5F12.6)
      E5P=EM6*QB/(EM5+EM6)
      E6P=EM5*QB/(EM5+EM6)
      RO=ROST
      E5F=EM5*E4/EM4
3      E5=E5F+E5P-2.*SQRTF(E5F*E5P)*COSF(RO)
      COSDL=(E5+E5F-E5P)/(2.*SQRTF(E5F*E5))
      SNDL2=(1.-COSDL**2)
      IF(SNDL2)16,17,17
16     SNDL2=0.000000
17     TANDL=SQRTF(SNDL2)/COSDL
      DELTA=ATANF(TANDL)
      IF(TANDL)6,6,30
6      DELTA=DELTA+3.1415927
30     IF(RO-3.1415927)7,7,24
7      GAMRD=PHIRD-DELTA
      GO TO 25
24     GAMRD=PHIRD+DELTA
25     GAMMA=GAMRD*57.2957786
      E6F=EM6*E4/EM4
      E6=E6F+E6P+2.*SQRTF(E6F*E6P)*COSF(RO)
      PUNCH 102,GAMMA,E5,E6
102    FORMAT(1H0,3F12.6//)
      COSEP=(E6+E6F-E6P)/(2.*SQRTF(E6*E6F))

```



```

      SNEP2=(1.-COSEP**2)
      IF(SNEP2)18,19,19
18    SNEP2=0.000000
19    TANEP=SQRTF(SNEP2)/COSEP
      EP=ATANF(TANEP)
      IF(TANEP)8,8,9
8     EP=EP+3.1415927
9     E7P=EM8*QF/(EM7+EM8)
      E8P=EM7*QF/(EM7+EM8)
      E7F=EM7*E6/EM6
      E8F=EM8*E6/EM6
      ZETA=ZETST
4     E7=E7P+E7F-2.*SQRTF(E7P*E7F)*COSF(ZETA)
      COSOM=(E7+E7F-E7P)/(2.*SQRTF(E7F*E7))
      SNOM2=(1.-COSOM**2)
      IF(SNOM2)20,21,21
20    SNOM2=0.000000
21    TANOM=SQRTF(SNOM2)/COSOM
      OMEGA=ATANF(TANOM)
      IF(TANOM)10,10,31
10    OMEGA=OMEGA+3.1415927
31    IF(RO-3.1415927)11,11,26
11    BET1=PHIRD+EP-OMEGA
      GO TO 27
26    BET1=PHIRD-EP-OMEGA+6.2831854
27    BETA1=BET1*57.2957786
      E8=F8P+E8F+2.*SQRTF(F8P*E8F)*COSF(ZETA)
      COSXI=(E8+E8F-E8P)/(2.*SQRTF(E8*E8F))
      SNXI2=(1.-COSXI**2)
      IF(SNXI2)22,23,23
22    SNXI2=0.000000
23    TANXI=SQRTF(SNXI2)/COSXI
      XI=ATANF(TANXI)
      IF(TANXI)12,12,32
12    XI=XI+3.1415927
32    IF(RO-3.1415927)13,13,28
13    BET2=PHIRD+EP+XI
      GO TO 29
28    BET2=PHIRD-EP+XI+6.2831854
29    BETA2=BET2*57.2957786
      PUNCH 103,BETA1,E7,BETA2,E8
103   FORMAT(1X4F12.6)
      ZETA=ZETA+DZET
      IF(ZETA-ZETF)4,4,5
5     RO=RO+DRO
      IF(RO-ROF)3,3,15
15    PUNCH 104
104   FORMAT(1H2)
      GO TO 14
      END

```


APPENDIX II

A TRANSISTORIZED, FREQUENCY MODULATED PROTON MAGNETIC RESONANCE SYSTEM FOR THE MEASUREMENT AND CONTROL OF MAGNETIC FIELDS

I. Introduction

The original research project of the author was the instrumentation and utilization of a Spectromagnetic Industries 50 centimeter combined broad range magnetic spectrograph and spectrometer. At that time it was felt that the precise magnetic field regulation which can be obtained using nuclear magnetic resonance techniques would be necessary for the successful operation of this instrument. However, although there were several systems using this phenomenon for field regulation commercially available, not one had probes suitable for use with our magnet, and the purchase of custom, or specially designed probes, would have been unjustifiably costly. It was therefore decided to build our own regulating system, tailoring it to satisfy our particular needs.

This NMR (nuclear magnetic resonance) system was designed to measure and control magnetic fields from one to thirteen kilogauss to a very high degree of accuracy. It is fully transistorized and employs frequency modulation of the radio frequency oscillator rather than the usual amplitude modulation of the magnetic field.

The circuits are of modular construction to facilitate trouble shooting and alignment procedures. The use of frequency modulation permits considerable reduction in probe size over that of conventional systems because the field modulating Helmholtz coils are not required. This, in fact, was the main reason why frequency modulation was employed. It also gives the probe cylindrical symmetry so that special orientation of it in the magnetic field to achieve the optimum signal to noise figure is not necessary. This feature has proved to be a great convenience.

Four probes are required to cover the frequency range from 4.8 to 55 mc/s (\sim 1 to 13 kilogauss), and they can be quickly and conveniently changed without breaking the vacuum of the spectrometer. The magnetic field is controlled by an error signal, derived from the field itself, which is used for closed loop regulation of the magnet current power supply. It provides an error signal of ± 5 volts for a 0.05 gauss change in magnetic field.

It should be mentioned that the homogeneity of the field produced by the spectromagnet was found, using the above system as a fluxmeter, to be far below contract specifications. The magnet was therefore returned to the manufacturer for rebuilding. It was for this reason that the author discontinued work on this project.

II. Background and Design Considerations

The operation of this instrument is based on the phenomenon of

nuclear magnetic resonance absorption (Bl48) in which radio frequency energy is transferred from an electrical circuit to a nuclear spin system located in a magnetic field.

Consider an assembly of non-interacting nuclei in the presence of a magnetic field, \vec{H}_0 . For each nucleus there will be $(2I + 1)$ equally spaced energy levels, where $I\hbar$ is the maximum z component of angular momentum. The energy of the i^{th} level is given by

$$E_i = E_0 - (\vec{\mu} \cdot \vec{H}_0)_i \quad (1)$$

where $\vec{\mu}$ is the magnetic moment of the nucleus, $-\vec{\mu} \cdot \vec{H}_0$ the magnetic dipole interaction energy, and E_0 the energy of the unperturbed nucleus. Taking the z axis in the direction of the magnetic field, \vec{H}_0 , E_i may be rewritten as

$$E_i = E_0 - \vec{\mu} \cdot H_0 \vec{k} = E_0 - \hbar H_0 m_i \quad (2)$$

since $\vec{\mu} = \gamma \hbar \vec{I}$, where γ is the nuclear gyromagnetic ratio. The scalar product $\vec{I} \cdot \vec{k}$ is simply m_i , the magnetic quantum number whose value runs from $-I$ to $+I$ in integral steps. Adjacent levels are thus separated in energy ΔE where

$$\Delta E = \gamma \hbar H_0 \quad (3)$$

This is the amount of energy that is required to induce transitions from a lower magnetic substate to an upper magnetic substate. It can be supplied to the spin system by placing the assembly of nuclei inside

a radio frequency coil which is driven at a frequency given by

$$h\nu = \gamma \hbar H_0$$

$$\text{or} \quad 2\pi\nu = \gamma H_0 \quad (4)$$

$$\text{or} \quad \omega = \gamma H_0$$

The nuclei used in the instrument to be described are hydrogen, or protons, for which

$$\frac{\gamma p}{2\pi} = \frac{g e}{4 m_p c} = 4.25784 \text{ mc/s/kilogauss} \quad (5)$$

where $g = 5.58550$ nuclear magnetons for protons
 $e =$ electronic charge
 $m_p =$ proton mass
 $c =$ velocity of light

Therefore, equation (4) can be written, for protons,

$$\nu = 4.25784 H_0 \text{ Mc/s} \quad (6)$$

with H_0 measure in kilogauss.

The accuracy to which the field can be measured, then, is limited only by the accuracy to which the absorption or resonance frequency can be measured. The frequency range of the rf oscillator is specified by this equation (6). Therefore, in order to measure fields in the one to thirteen kilogauss range, an oscillator with a frequency range from 4.2 to approximately 55 Mc/s is required.

The optimum rf magnetic field that the oscillator should generate inside the coil can be estimated from the "saturation condition" (B148). That is

$$\gamma^2 H_1^2 T_1 T_2^* = 1 \quad (7)$$

where H_1 is one half the amplitude of the rf field, which may be written

$$H_x = 2H_1 e^{-2\pi i \nu t}, \quad H_y = 0 \quad (8)$$

T_1 is called the spin-lattice relaxation time. It is the time required for the spin temperature of the nuclei to return to the lattice temperature after the sudden removal of the rf field or, in other words, the time required for the state populations to return to their thermal equilibrium values by the interaction of the spins with the lattice. The experimental values of T_1 range from 10^{-4} to 10^4 seconds, being largest for solids, and as low as 10^{-3} seconds for pure liquids. The lowest values can be reached by the addition of paramagnetic ions, as will be mentioned later. Two very convenient proton sources, water and glycerin, have spin-lattice relaxation times of 2.3 and 0.007 seconds respectively.

T_2^* is the characteristic time which describes the spin-spin interaction between neighboring dipoles, and is a direct measure of the inverse line width. It is defined by the equation

$$T_2^* = 1/2 g(\nu)_{\max}. \quad (9)$$

where $g(\nu)_{\max.}$ is the peak value of the observed shape, $g(\nu)$, of the absorption line. Experimentally, $g(\nu)$ is intermediate between a damped oscillator and a gaussian for aqueous ferric nitrate solutions. For a gaussian curve

$$1/T_2^* = (2\pi)^{-1/2} \gamma \Delta H, \quad (10)$$

and for a damped oscillator

$$1/T_2^* = (\sqrt{3}/2) \gamma \Delta H \quad (11)$$

where ΔH is the width at half maximum of $G(\nu)$, in gauss.

An order of magnitude estimate of the natural line width may be obtained by considering that in addition to the main magnetic field, H_0 , each nucleus is subjected to 'local' field, H_{loc} , set up by neighboring magnetic dipoles. In order of magnitude

$$H_{loc} \approx \mu/r^3 \approx \text{a few gauss for } r = 1 \text{ \AA} \quad (12)$$

so that the resonance condition now becomes

$$\nu = \gamma/2\pi (H_0 + H_{loc}). \quad (13)$$

The width of the absorption line in terms of frequency spread would then be of the order of μ^2/r^3 or 10 kc/s for $r = 1 \text{ \AA}$.

It should be noted that since T_2^* is an experimentally determined quantity, it necessarily contains all sources of line broadening, including inhomogenieties in the main magnetic field, H_0 .

Bloembergen, Purcell and Pound (B148) give an expression, based on equation (7), for the optimum signal to noise ratio and it should be examined before using equation (7) to determine the optimum value of the rf field. This expression is

$$A_s/A_n \approx 1.62(10^{-4}) \frac{V_c^{2/3} \zeta Y h^2 N_o I(I+1)}{kT(kTBF)^{1/2}} \gamma^{11/4} H_o^{7/4} (T_2^*/T_1)^{1/2} \quad (14)$$

where V_c = the volume inside the rf coil,

ζ = the fraction of V_c that is occupied by the sample,

Y = a constant, the order of unity, and depends on the exact line shape and the amplitude and shape of the modulating wave,

N_o = the number of sample nuclei/cc present,

k = Boltzmann's constant,

and T = the absolute temperature of the sample.

B and F are parameters characteristic of the detecting apparatus, B being the band width of the amplifier system used, and F being an over-all noise figure.

With equation (14) in mind, the proton sample chosen for the instrument to be described was water with ferric nitrate ($\text{Fe}(\text{NO}_3)_3 \cdot 9\text{H}_2\text{O}$) added in the proportion of one part to 100 parts of water. The addition of this paramagnetic salt reduced the value of T_1 from 2.3 seconds to approximately 2×10^{-3} seconds, as determined from an experimental curve given in (B148). Extrapolation of figure 16 in (B148) gives the same value for T_2^* . Thus, the signal to noise ratio was increased by a factor of approximately 400 as compared to that for pure

water. Also, T_1 now forms an important contribution to the line width.

Using equation (7) and $T_1 = T_2^* = 2 \times 10^{-3}$ seconds as determined above, the optimum rf magnetic field amplitude, $2H_1$ from equation (8), turns out to be approximately 0.04 gauss. The optimum value of the peak rf current can then be calculated from the relation,

$$L I_1 = 2H_1 nA \quad (15)$$

where

$$I_{rf} = I_1 e^{-2\pi i \nu t} \text{ abamperes} \quad (16)$$

and

L = the inductance of the coil in abhenries,
 n = the number of turns in the coil,
and A = the area of the coil in cm^2 .

A typical value for I_1 can be obtained by considering one of the four probes mentioned in the introduction; the low frequency probe (4.8 to 9.1 mc/s). This coil has an inductance of 11 microhenries, 52 turns, and area of 0.5 cm^2 . Hence

$$I_1 \approx 1 \text{ milliampere} \quad (17)$$

Modulation

As already noted, when the frequency of the rf oscillator passes through the resonance condition, energy is absorbed from the field of the coil. This absorption manifests itself by a decrease in the resonant impedance of the tank circuit. Thus if the tank circuit is fed from a constant current source, the absorption process can be observed

by noting a decrease in the rf voltage across it. Normally, modulation of the main magnetic field, H_0 , is applied in order to sweep the resonance and obtain a periodic absorption of energy, which can then be easily observed on an oscilloscope. The modulation frequencies in practically all cases are less than 1000 cps. Hence, when the resonance is being swept, the rf voltage across the tank circuit is modulated at an audio rate, and demodulation results in the production of an audio signal characteristic of the absorption process taking place. The amplitude of the modulating field, usually supplied by a pair of Helmholtz coils spanning the sample, should be several times the line width of the sample. Typically, from equation (13), the natural line width of a liquid sample would be of the order of two gauss (for water it is much less than this). Modulating fields which can be varied from zero to twenty gauss are commonly employed.

The resonance condition can also be swept by using frequency modulation of the rf frequency. This can be done by employing a capacitor in the tank circuit, in addition to the tuning capacitor, whose capacity can be varied over small limits at an audio rate. Knoebel and Hahn (Kn51) constructed a frequency modulated magnetic resonance detector by using as the modulating capacitor a small fixed plate in close proximity to a sinusoidally vibrating plate, driven at 60 cps. A much simpler and more elegant method of producing the frequency modulation is realized by using in the tank circuit a solid state device called a varicap, which is a diode whose capacity is determined

by an applied bias voltage. This bias can be varied at an audio rate over predetermined limits to produce the desired modulation of the tank circuit resonant frequency. The variation in capacity ΔC which is equivalent to a value of field modulation ΔH is given by

$$\Delta C = 2C \Delta H/H_0 \quad (18)$$

where C is the total capacity of the tuned circuit required to establish the resonance condition given by equation (4), $\omega = \gamma H_0$. For a 20 gauss sweep, ΔH , at a field of 2.15 kilogauss (upper limit of probe number one) which corresponds to value for C of 28 μpf , $\Delta C = 0.5 \mu\text{pf}$. The modulation circuit designed for the instrument to be described allows a continuous variation of ΔC from zero to 1.5 μpf .

Magnetic Field Regulation

Because the value of the magnetic field produced by an electromagnet is not solely dependent upon the magnet current, but also on the permeability of the iron (which may vary with temperature) forming the yoke, it is desirable to control the field by sensing any changes in H_0 itself rather than by depending only on the stability of the magnet current power supply. This is done by utilizing the finite width of the proton magnetic resonance absorption line.

If the amplitude of the modulating signal is such that the variation in the main magnetic field or, equivalently, the variation in the rf frequency in the case of frequency modulation, is greater than the line

width, the audio signal resulting after rf rectification has a frequency of $2 \omega_m$, where ω_m is the modulation frequency. That is, there are two absorption processes for each modulation cycle. However, if the modulation amplitude is decreased so that only a very small part of the absorption curve is spanned, the resulting audio signal will have a frequency ω_m , and its amplitude will be proportional to the slope of the absorption curve at the point about which the field or frequency is varying. The maximum signal is obtained when this point is at the point of inflection, and the minimum, zero, when this point is at the maximum of the absorption curve. The phase of the audio signal corresponding to one side of the curve differs by 180° from that corresponding to the other side.

The nature of this signal suggests the use of a phase sensitive detector to convert the proton signals of frequency ω_m to dc error signals, positive or negative depending on the relative phase of the proton signal with respect to the detector driving signal, also of frequency ω_m . Such an error signal is injected into the magnet current power supply, thus establishing closed loop field regulation to within the line width of the proton sample being used.

III. A General Description of the System

A generalized block diagram of the system is given in figure 1. The rf oscillator and a preamplifier form the NMR head which is located at the magnet whose field is to be measured and/or controlled by this

device. Fifty foot coaxial cables (Telcon* AS-48) are provided to connect the head to the rest of the system. Remote tuning of the oscillator can be accomplished by means of a 0.7 rpm reversible Bodine** (Type KC1-22RC) motor mounted on the head and coupled to the tuning capacitor through a gearing system which reduces the revolution rate to approximately 0.02 rpm.

The head itself is constructed of 1/8" brass plate of overall dimensions of 3" x 4-3/8" x 6-1/2", with separate compartments for the oscillator, the preamplifier, the modulation input, and the power line filtering components (10 millihenry" weeductors"*** in the voltage lines).

The heart of the remote, controlling part of the system is the twin tee oscillator. This circuit supplies the modulation voltage (for the varicap), the compensating signal to the preamplifier, the chopper drive signal, the horizontal sweep for the indicator oscilloscope, and a test signal to the twin tee amplifier for initial lining up procedures.

The proton signal is fed directly into the Function switch, which then directs it to the circuits indicated in the following table,

Table I:

-
- * Telcex Works, Greenwich, S.E. 10, England
 - ** Bodine Electric Co., Chicago, Illinois, U.S.A.
 - *** Nytronics, Inc., Berkeley Heights, N.J., U.S.A.

Table 1

Function Switch Position	Function
1	The proton signal is fed directly into the vertical amplifier of the indicator oscilloscope.
2	The proton signal is directed to the twin tee amplifier, whose output is fed to the oscilloscope.
3	A 200 cps test signal from the twin tee oscillator is fed into the twin tee amplifier, the output of which is displayed on the oscilloscope. This position is used to test the operation of the twin tee amplifier, the chopper, and the filter circuit.
4	The proton signal is fed into the twin tee amplifier, and the output of the chopper (or phase sensitive detector) is fed to the oscilloscope.

When the rf frequency is sitting on the side of the absorption curve and the modulation amplitude is set at a small fraction of the line width, the proton signal has a frequency of 200 cps, that of the twin tee oscillator. The twin tee amplifier filters out the noise accompanying this proton signal and feeds it into the phase sensitive detector. The phase of the detector driving signal, obtained from the 200 cps oscillator, can be made exactly in or out of phase with the proton signal. The detector or chopper output is then in the form of a full wave rectified signal. This is fed into the filter or time constant network where it is converted into the dc error signal. Time

constants provided are 1, 5, 10, and 20 seconds. The 100-0-100 micro-ammeter provides a visual indication of the error signal.

IV. Circuits

A. The RF. Oscillator (Figure 2a)

The rf oscillator employs two high frequency, silicon transistors (2N920, $f_{\alpha} = 400 \text{ Mc/s}$) with the tank circuit in the collector circuit of Q_1 . The Varicap*, which provides the frequency modulation, is located in the tank circuit. It is a high Q, voltage-variable capacitor with a static capacitance of $10 \mu\text{f}$ at 4 volts bias. The use of the transistor, Q_3 , in the feedback loop reduces the loading of the collector of Q_1 by the feedback elements (the $220 \mu\text{f}$ capacitor and the 5K Trimpot) and, together with the 5K Trimpot, makes the oscillator practically independent of the emitter resistance of Q_1 , thus increasing its frequency stability and reducing the variation in the rf voltage level with frequency.

The oscillator is fed from a constant current source Q_2 , the current being determined by the voltage drop across the 5.62K resistor in the emitter circuit of Q_2 . By varying the voltage of the base of Q_2 from -30 to -20 volts, the level of oscillation can be varied from 0 to

* Varicap Type PC-115-10, obtained from Pacific Semiconductors, Inc., Hawthorne, California

10 volts peak-to peak over the frequency range of 4.8 to 55 Mc/s, the operating value being adjusted to give the optimum resonance signal. The peak value of the rf current (10 volts/5.62K) was chosen in accordance with the estimate of equation (17), allowing for a margin of safety.

The above frequency range is achieved by using four different rf coils in the tank circuit. These will be described later. One setting of the feedback resistor can be found which will provide smooth operation of the oscillator from 4.8 to 26 mc/s, a range covered by three of the probes. However, when using the high frequency coil, that is for 26 to 55 mc/s operation, the feedback must be reduced slightly to obtain smooth level control over the range of this probe.

The frequency is slightly dependent upon the value of the constant current driving the tank circuit so that the constant current source must be well stabilized and temperature effects must be reduced to a minimum. Hence the use of silicon transistors throughout the oscillator circuit.

The Varicap is operated at a bias greater than or equal to 16 volts where its capacitance vs. temperature characteristic is flat from -20°C to $+120^{\circ}\text{C}$. The bias is applied through the 5.6 megohm resistor and is derived from the +30 volt line through a 50K panel-mounted potentiometer. The 200 cps modulating voltage is fed through the 1.5 megohm resistor.

The choice of the low capacity varicap was made to keep to a

minimum the modulation of the tank circuit resonant impedance caused by the varying bias on this element. Such modulation produces audio signals which could be comparable in magnitude to the proton signal itself. A compensation circuit has been included in this system to cancel out this effect.

The figure of merit or the Q value for this varicap at a bias of 16 volts and 50 mc/s is approximately 200, and exceeds 1000 at 5 Mc/s.

The frequency stability of the oscillator was measured using a Hewlett Packard model 524C frequency meter. It was found that over an eight-hour period the oscillator was stable to one part in 10^5 with the ± 30 volts lines being supplied by transistorized power supplies. Owing to the sensitivity of the circuit, any disturbance on the -30 volt line adversely affected both the frequency stability and the signal to noise ratio of the proton signal. Therefore, it is highly desirable to use batteries for the -30 volt line of the rf oscillator circuit.

B. The Probes

Figure 3 shows a cross-sectional view of the probe in its container or shield which was designed especially for the Spectromagnetic Industries 50 centimeter combined broad range spectrograph and spectrometer. The probe itself consists of the coil wound on a lucite form (which also contains the proton sample), the 1/8" brass rod, and the Amphenol UG-568/U connector. One end of the coil is soldered to the brass rod just back of the lucite form and the other to the banana plug in the threaded teflon end piece. The coil wire passes through

the end pieces which serve to keep the coil centrally positioned in the container. Teflon is used for the end piece simply because it provides an excellent seal to the lucite form, thus keeping the proton sample well contained. The banana plug fits into a blind hole drilled in the end of the brass container which itself serves as the return path to ground and as a shield for the coil. The container is permanently mounted in the vacuum chamber between the pole faces of the magnet with an O-ring vacuum seal being made at the flange. Hence, probes can be quickly and conveniently changed without breaking the vacuum of the spectrometer. The NMR head couples directly to the amphenol connector of the probe, of which there are four to cover the frequency range from 4.8 to 55 mc/s as indicated in figure 3.

In keeping with optimum coil design, the coils have Q values between 150 and 200, and resonant impedances of the order of 10K. They are 7/8" long and have a filling factor (ζ of equation (14)) of 0.64 or, in other words, they contain 0.51 cc of the ferric nitrate solution mentioned earlier.

C. The Preamplifier (Figure 2b)

The proton resonance is detected by the 1N903 silicon diode and is fed through the 10K - .01 μ f RC filter to a ring-of-three preamplifier which, with the input filter, has its upper 3db point at 1000 cps. Such a narrow bandwidth is in keeping with the desire to achieve the optimum signal to noise ratio as indicated in equation (14). The maximum gain of the preamplifier, given approximately by the ratio of

the two resistors in the emitter circuit of Q_3 , is 800 but this is reduced to about 600 by the input filter and the 1K output resistor. The noise at the output is approximately 5 millivolts peak-to-peak. This low value is achieved by having a low standing current in the first transistor. Thus Q_1 must have a high gain at low currents, a requirement admirably satisfied by the 2N393 transistor.

A signal which compensates for that produced by the varying bias on the varicap is fed into the preamplifier through the 100K resistor to the emitter of Q_1 .

D. The Twin Tee Oscillator (Figure 4)

The twin tee oscillator consists basically of an operational (dc feedback-pair) amplifier, Q_1 and Q_2 . The use of such an amplifier ensures the dc stability of the oscillator. AC negative feedback is applied through the twin tee notch filter for all frequencies other than the notch or null frequency. Q_3 provides a low impedance driving source for the tee and Q_2 the high impedance load. This arrangement allows the values of the components in the twin tee network to be calculated using the standard formulas for such a filter. The loop gain of the circuit is essentially zero for all frequencies other than the notch frequency, and of course exceeds unity for that frequency. Slight frequency adjustments (195 - 213 cps) can be made by means of the 20K trimpot in the tee, and amplitude adjustments by means of the 50K trimpot. As operating in the present system, the oscillator runs at its maximum output of 4 volts peak-to-peak and at 200 cps. Q_4 is an

emitter follower stage which provides isolation of the oscillator from the other circuits and the appropriate current to drive the modulation amplifier, the compensation amplifier, the horizontal amplifier, the chopper drive, and the twin tee amplifier when using this oscillator to provide a test signal for lining up procedures.

This oscillator, unlike most other low frequency oscillators not employing special temperature compensating devices, is very stable. No detectable change in either its frequency or amplitude was observed when the circuit was heated to 55° C.

E. The Twin Tee Amplifier (Figure 5)

The twin tee amplifier is very similar to the oscillator in construction. In this case, however, degeneration is provided for all frequencies through the 100K resistor, and additional high frequency degeneration through the 1000 μ f capacitor from the collector of Q_1 to ground. The tee is adjusted so that the negative feedback is sufficient to make the loop gain less than unity for all frequencies. The bandwidth is determined primarily by the setting of the 50K trimpot, and the notch frequency by the settings of the 20K trimpots (which should be the same), although they are not completely independent. The bandwidth in the present system is adjusted to 16 cps at 200 cps, where the peak gain is 35. The maximum input before distortion of the output develops is 280 millivolts peak-to-peak. Again, this amplifier exhibits an extremely good stability over a wide temperature range.

F. Modulation Amplitude Control Amplifier (Figure 6)

This circuit is simply an operational (a dc feedback-pair) amplifier with a gain of 2.5. It provides a 10 volt peak-to-peak (200 cps) signal to the 2K helipot control on the front panel of the control unit. Hence, the modulation of the bias on the varicap can be varied from zero to ± 5 volts.

G. 200 cps Compensation Circuit (Figure 7)

This circuit supplies up to 2 volts peak-to-peak of 200 cps signal of completely variable phase to the 100K resistor in the emitter circuit of Q_1 of the NMR preamplifier. Hence, any 200 cps signal resulting from the variation of the rf oscillator tank circuit impedance which is due to the varying bias on the varicap can be cancelled out. The boot-strapped emitter follower, Q_1 , takes its input from the center tap of 20K control driven by the 4 volt peak-to-peak 200 cps signal from the twin tee oscillator. The output of Q_1 is fed into a phase shifting network consisting of the two 1K resistors dividing the input to Q_2 , the 0.5 μ f capacitor feeding Q_3 , and the panel mounted potentiometer (20K) P which provides a continuous phase adjustment of 180° . Q_2 and Q_3 form a difference amplifier whose gain is approximately unity (given approximately by the ratio of the emitter resistance to the collector resistance of each transistor). The 1K trimpot allows the amplifier to be balanced (i.e., equality of collector voltages) so that maximum temperature stability can be achieved. The

output from the difference amplifier is taken from either collector (of Q_2 or Q_3) by means of a panel mounted "phase" switch and fed into the boot-strapped emitter follower, Q_4 , which provides the very high load impedance required by the difference amplifier. The output of Q_4 is fed into the NMR preamplifier through fifty feet of co-axial cable.

H. Vertical Amplifier for Indicator Oscilloscope (Figure 8)

Q_1 and Q_2 comprise a difference amplifier whose input is obtained from the center tap of a 10K "vertical gain" panel mounted control. The input to this control comes from the "Function Switch" on the panel. The gain of this amplifier is 13. The output from each collector is fed to another boot-strapped emitter follower (Q_3 and Q_4), which in turn feeds a dc fed-back pair amplifier (Q_5 , Q_6 and Q_7 , Q_8) whose gain is 15. Each dc amplifier drives one vertical deflection plate of the oscilloscope and can supply an eighty volt peak-to-peak signal. Hence, an effective voltage swing of eighty volts on the vertical deflection plates can be obtained (vertical deflection sensitivity = 35 volts/inch). The 1K trimpot in the emitter circuit of the difference amplifier should be adjusted to equalize the collector voltages of Q_1 and Q_2 .

I. Horizontal Amplifier for Indicator Oscilloscope (Figure 9)

This circuit is basically the same as the Vertical amplifier, H. In this case, however, there is a phase shifting network identical to that in the compensating circuit, G. The input is taken as shown from

the 200 cps oscillator. The 10K Horizontal Gain control and the 20K phase control are panel mounted. The gain of the difference amplifier stage is 10, and that of the dc fed-back pair stage is 9. Each dc fed-back pair amplifier (Q_6, Q_7 and Q_8, Q_9) drives a horizontal plate of the indicator oscilloscope. The maximum effective voltage swing on the horizontal deflection system is approximately 90 volts (Horizontal deflection sensitivity = 40 volts/inch).

J. Phase Sensitive Detector (or Chopper) Driver (Figure 10)

This circuit consists mainly of the difference amplifier Q_2, Q_3 with its input taken from the type of phase shifting network already described. It provides two in-phase outputs of 25 volts peak-to-peak of completely variable phase. These outputs are used to drive the chopper or phase sensitive detector circuit. The input to this circuit is taken directly from the twin tee oscillator (4v peak-to-peak). Q_1 provides sufficient current to drive the phase shifting network. The output from the collector of either Q_2 or Q_3 is fed into the bootstrapped emitter followers Q_4 and Q_5 through the "phase reversal" switch mounted on the panel. Continuous phase adjustment over 180° is provided by the panel mounted 20K control, P.

K. Phase Sensitive Detector (Figure 11)

This circuit is essentially a full wave rectifier-amplifier circuit. Transistors Q_1 and Q_2 act as switches which are turned off and on by the Driving signal. The diodes CR1, CR2, and CR3, CR4 square off the

driving signal to Q_1 and Q_2 respectively. CR2 and 3 limit the emitter-base voltage to approximately 0.7 volts, limiting the base current during the "on" periods to 0.7 milliamps. The biases on CR1 and CR4 are provided by 1.3 volt mercury batteries. The 15K resistors preceding the diodes serve as the loads for Q_4 and Q_5 of the Driver circuit.

The output of the twin tee amplifier is coupled into the detector circuit by means of the transformer, UTC* 0-26. Thus the 200 cps proton signal appears at the emitters of Q_1 and Q_2 180° out of phase with each other. By proper adjustment of its phase, the driving signal can be made exactly in or out of phase with the proton signal. Under these conditions each transistor switch (Q_1 and Q_2) half-wave rectifies the proton signal. These signals are then added by the adder amplifier Q_5 and Q_6 (a dc-fed-back pair amplifier, gain = 15) to produce an amplified, full-wave rectified proton signal at the output. Q_3 and Q_4 are emitter follower isolating stages. Under no-signal conditions, the voltage of the bases of Q_3 and Q_4 must be adjusted for a minimum waveform at these points (at most two mv peak-to-peak). All the transistors in this circuit are dc-coupled to retain the ground reference for the rectified signal. The output is taken from between the 10K resistor and the 10K trimpot to facilitate the use of a dc-coupled, dc-fed-back pair amplifier in the following time constant circuit. The voltage at this point is adjusted to + 15 volts.

*United Transformer Company, 150 Varick Street, New York 13, N.Y.

L. Time Constant Circuit (Figure 12)

The dc fed-back pair amplifier in this circuit is used to provide the full-wave rectified proton signal at a reference level of zero volts. The emitter voltage of Q_1 is set by the 15 volt Zener diode, and the emitter voltage of Q_2 (zero volts) is set by the 20K trimpot. The maximum output of this circuit to the time constant network is ± 10 volts. The 10K resistor provides the loading of Q_2 , and isolates the filter network from the amplifier. It is important to have the dc level of Q_2 at zero volts so that a spurious error signal will not result. The filter network provides a maximum of ± 5 volts at time constants of 1, 5, 10, or 20 seconds.

M. The Power Input Circuit

Figure 13 shows the circuit which provides the various voltage lines for the system. The input voltages, + 30 volts and - 90 volts, are obtained from two 100 volt, 500 milliampere, Power Design, Inc.* transistorized power supplies (model 105TA). The - 30 volt line for the oscillator section of the NMR head is taken from the battery circuit shown in the figure. The battery consists of two 18 volt, rechargeable cadmium cells in series. Zener diodes are used throughout to establish the various voltages.

The indicator oscilloscope is a basic, general purpose James Millen** 3", rack mounted oscilloscope, model 90903, modified to allow

* Power Designs, Inc., 1700 Shames Drive, Westbury, N.Y.

** James Millen Mfg. Co. Inc., Malden, Mass.

signals to be applied to both plates of the vertical and the horizontal deflection systems, thus increasing its sensitivity by a factor of two.

Figure 14a shows a photograph of the control system, and figure 14b shows one of the back of the control system with its cover removed. Each modular circuit is lettered according to its lettering in the text.

Figure 15a shows the NMR head coupled to one of its probes, and figure 15b shows the rf oscillator and preamplifier modules.

V. Operation

A. Lining-up Procedures

1. Connect all the cables between the NMR head and the control system; that is, the power cable, the proton signal cable, the compensating signal cable, and the modulating signal cable.

2. Set the Time Constant switch to the SHORT position, the rf oscillator amplitude control to zero, the varicap bias to half maximum, the modulation amplitude control to zero, and the compensation switch to the 'out' position.

3. After having set the positive and negative power supplies to their respective values (+ 30 volts and - 90 volts), turn on the power to the system and make a fine adjustment of the + 30 volt line so that the positive and negative rails of the twin tee oscillator are the same.

4. Adjust to zero the potential difference between the collectors in the difference amplifiers of the following circuits (this adjustment can be made by means of the trimpots in the emitter circuits of the difference amplifiers):

- (a) the vertical amplifier (Q_1 and Q_2)
- (b) the horizontal amplifier (Q_2 and Q_3)
- (c) the detector driver circuit (Q_2 and Q_3)
- (d) the compensating circuit (Q_2 and Q_3)

5. Using an external oscilloscope, set the output of the twin tee oscillator to 4 volts peak-to-peak at 200 cps. The 20K trimpot provides slight frequency adjustment and the 50K trimpot amplitude adjustment.

6. In the phase sensitive detector circuit, adjust to zero the voltages at the bases of the transistors Q_3 and Q_4 by means of the 1K trimpots in the base circuits.

7. With the Time Constant switch in the Bal position and observing the panel meter and/or using a voltmeter connected to the emitter of Q_2 of the Time Constant circuit, set the emitter voltage of this transistor to zero by adjusting the 20K trimpot.

8. If the zero adjustment of step 7 cannot be obtained, adjust the 10K trimpot in the emitter circuit of Q_6 in the phase sensitive detector circuit and repeat steps 6 and 7.

9. Using a 50 millivolt, 200 cps signal from the twin tee oscillator (set the Function switch to the No. 3 position and connect a jumper lead from the oscillator to the twin tee amplifier) check that the gain of the twin tee amplifier is between 35 and 40.

10. Checking the operation of the phase sensitive detector: With the test signal connected as in step 9 and the time constant switch in the SHORT position, set the Function switch to the No. 4 position. This feeds the output of the chopper

into the indicator oscilloscope. Adjust the vertical and horizontal gain controls to give a display on the oscilloscope. Adjust the horizontal 'phase' and the chopper 'phase' to give the best V (or inverted) display. This indicates that the test signal (or the proton signal when the system is in use) is exactly in or out of phase with the chopper driving signal. This can also be checked by looking at the emitter of Q_2 of the Time Constant circuit where the waveform should be a full wave rectified signal (maximum peak value of ± 10 volts). With the Function switch reset to position 3, the meter can be switched on to check the dc output by setting the Time Constant switch to the Bal position. The dc output corresponding to a ± 10 volt rectified signal is ± 5 volts.

If the above steps check out, set the meter to the SHORT position, decrease the gain of the twin tee amplifier to zero, and remove the test signal jumper lead. The system is now ready for field measurement and control.

B. Magnetic Field Measurements

1. Set the Function switch to position 1. This directs the signal from the NMR head to the vertical amplifier.

2. If the approximate value of the field is known, choose the appropriate probe as indicated on figure 3. If probe No. 4 is required (i.e., for frequencies between 26 and 55 Mc/s) refer to the discussion of the rf oscillator in section III for a minor adjustment of the feedback in the oscillator circuit.

3. Turn up the rf amplitude until noise appears on the oscilloscope whose gain is set at about half maximum.

4. Set the modulation amplitude to half its maximum value. The trace on the oscilloscope will tilt because of the "spurious" 200 cps signal being detected (see discussion of compensation circuit). This tilt can be cancelled out by switching in the compensation and adjusting its amplitude and phase.

5. Slowly adjust the rf frequency until the proton signal is found. See figure 16 for the type of signal to expect. Center the pattern on the oscilloscope by adjusting the horizontal phase control. Decrease the modulation until the two dips are as close together as possible (any further decrease in the modulation will result in the disappearance of one of the dips). Recenter the crossover point of the two dips, and readjust the compensation amplitude so that the trace is horizontal. Under the above conditions the frequency modulation is sufficient to just span the absorption curve of the sample.

6. The amplitude of the proton signal can be increased, up to a point, by increasing the rf amplitude. Since the rf amplitude affects the frequency of the oscillator, the signal will have to be retuned, and the compensation readjusted if the rf amplitude is changed from the setting of step 3.

7. The frequency of the rf oscillator, and hence the value of the magnetic field, can be measured in the following way:

Connect the signal cable from the antenna connector of the NMR head to a suitable preamplifier, which is to be connected to the frequency meter (Hewlett Packard, model 524C). After noting the modulation setting, decrease it to zero and measure the rf frequency. The value of the magnetic field can be obtained from the following relation:

$$\nu = 4257.84 H_0$$

where ν_0 is measured in kilocycles and H_0 in gauss.

C. Magnetic Field Control

1. Connect a cable from the "Error Signal" output connector on the control panel to the magnet power supply, with the Time constant switch in the BAL position.

2. Obtain the proton signal as outlined in part B above, up to and including step 6.

3. Feed the proton signal into the twin tee amplifier by setting the function switch to position 2. The output of this amplifier is now displayed on the oscilloscope.

4. Switch out the compensation signal.

5. Decrease the modulation level and adjust the horizontal phase until a circular pattern appears on the screen. Adjust the rf frequency slightly to optimize the amplitude of the circular pattern. The modulation amplitude may also have to be further decreased to optimize this signal.

6. To compensate for any spurious 200 cps signal appearing because of the varying bias on the varicap detune the rf oscillator just off resonance. Increase the gain of the vertical amplifier, and switch in the compensation signal. Adjust its phase and amplitude to eliminate any circular trace on the screen of the oscilloscope.

7. Retune the oscillator to the setting of step 5. When the optimum 200 cps signal is obtained, as indicated by the optimum circular pattern, the rf oscillator is sitting at the inflection point of the proton resonance absorption curve.

8. To bring the detector drive signal in or out of phase with the proton signal adjust the detector phase control for

a maximum indication on the microammeter. The meter reads in volts and gives the magnitude of the error signal developed.

NOTE: The meter must be in the BAL position so that hunting will not occur while the error signal is being obtained.

9. With the error signal cable disconnected the phasing of step 8 can also be checked in the following way:

- (a) Set the meter to SHORT position.
- (b) Set Function switch to position 4. The chopped signal then feeds into the vertical amplifier of the oscilloscope.
- (c) Adjust the horizontal phase and detector phase until the optimum V (or inverted) is obtained.
- (d) Set the Function switch back to position 2, and Time Constant switch to BAL.
- (e) Readjust horizontal phase for the circular trace on oscilloscope.
- (f) Reconnect the error signal cable.

10. To start the controlling action, set the time constant to the appropriate time (to be determined by experiment). This applies the error signal to the magnet power supply. If the phasing between the detector drive and the proton signal is wrong, control will be impossible and the system will become regenerative. If such is the case, reverse the detector drive phase to establish control.

N. Bloembergen, E. M. Purcell, and R. V. Pound, Phys. Rev., 73, 697 (1948).

H. W. Knoebel and E. L. Hahn, Rev. Sci. Inst., 22, 904 (1951).

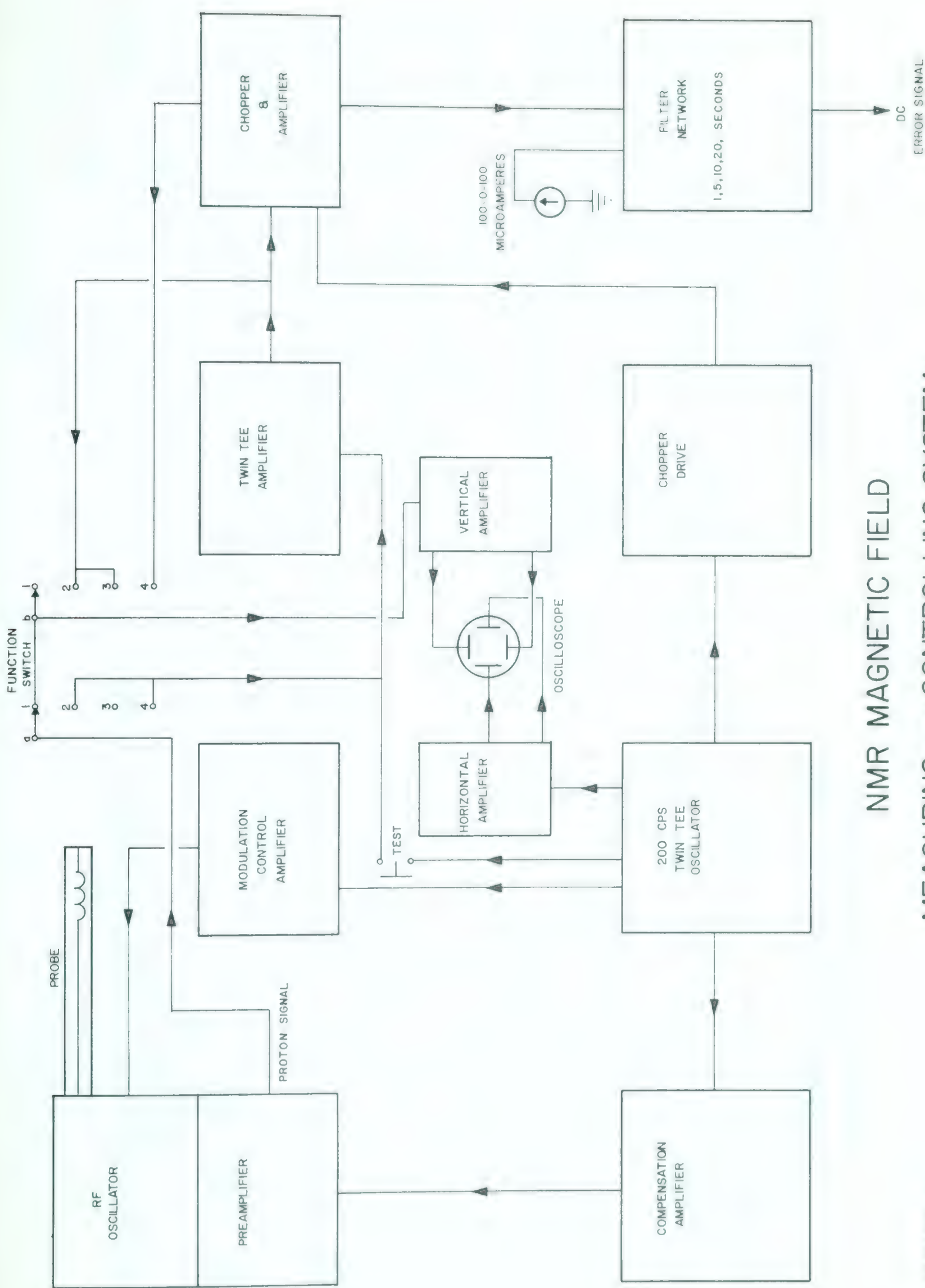
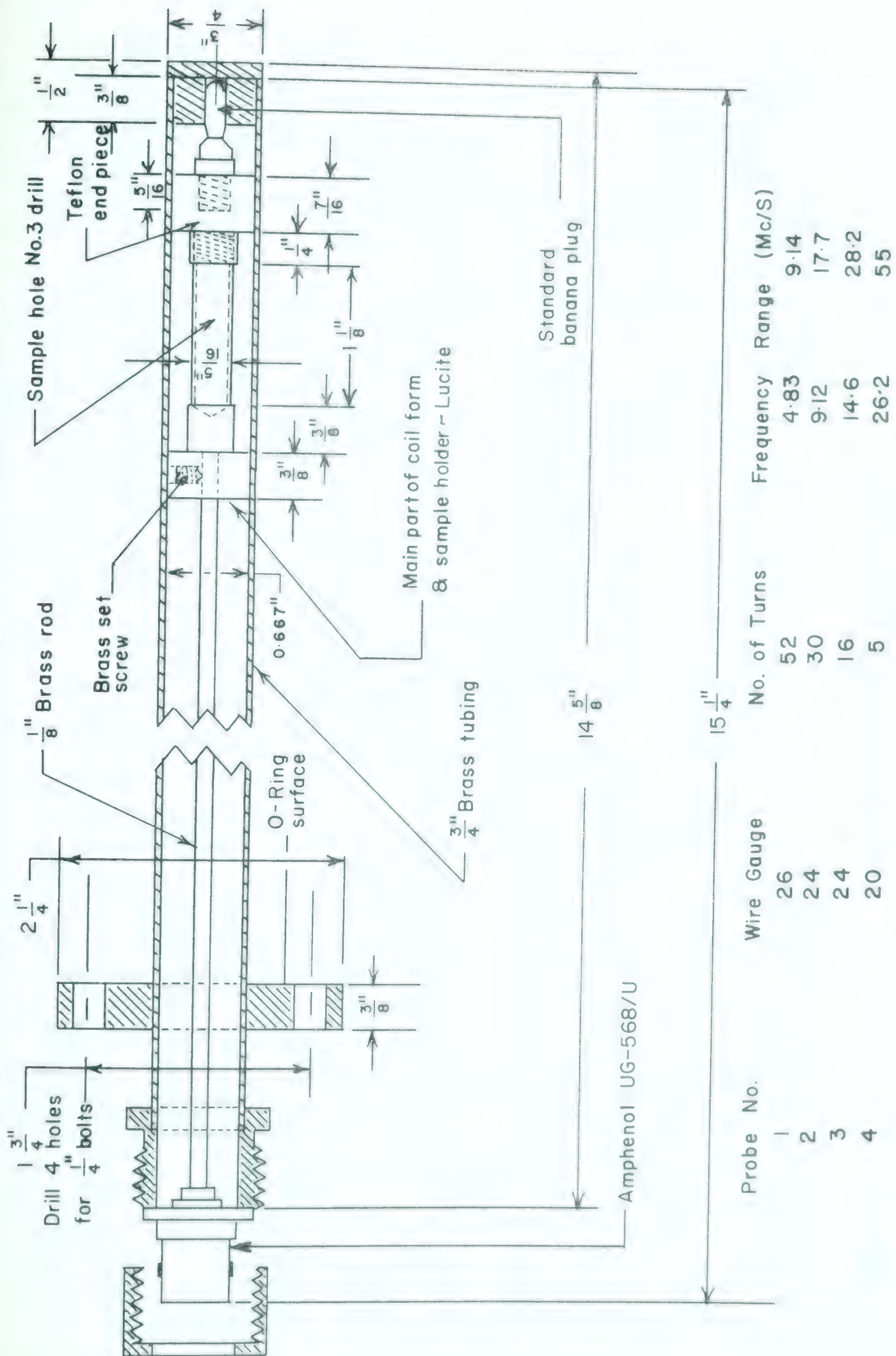


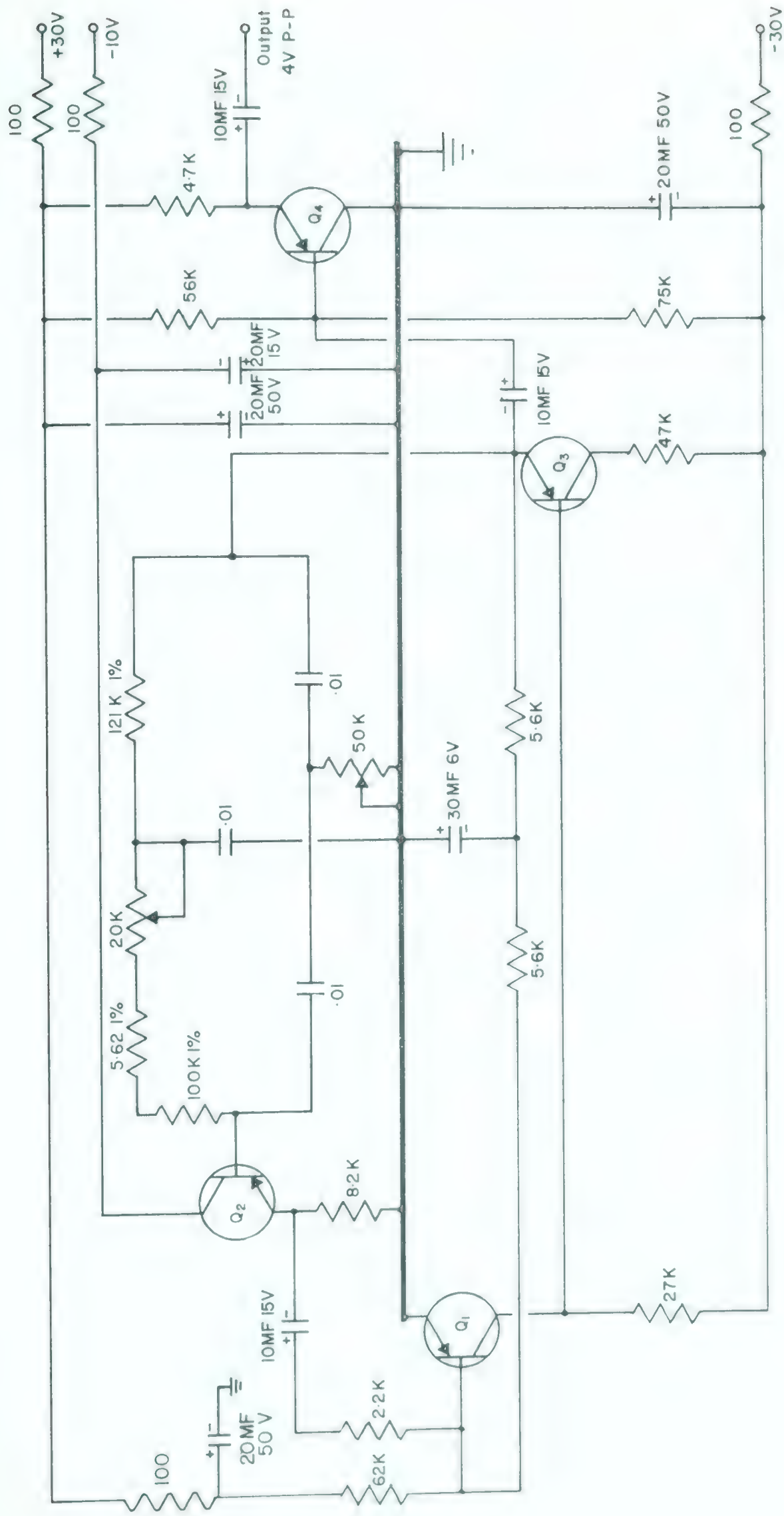
FIGURE 1

NMR MAGNETIC FIELD MEASURING and CONTROLLING SYSTEM



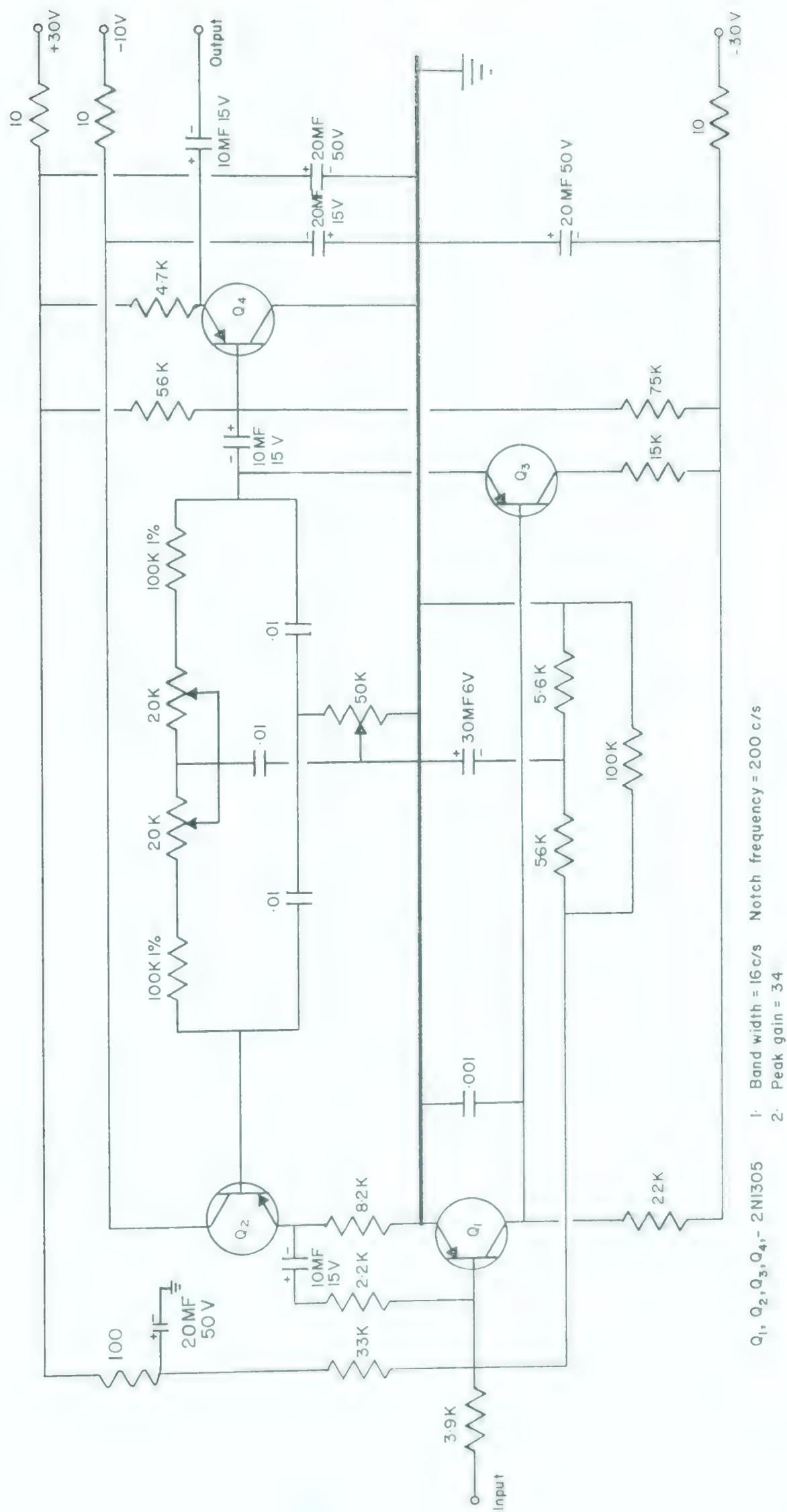
Probe No.	Wire Gauge	No. of Turns	Frequency	Range (Mc/S)
1	26	52	4.83	9.14
2	24	30	9.12	17.7
3	24	16	14.6	28.2
4	20	5	26.2	55

FIGURE 3 NMR PROBE



Q₁, Q₂, Q₃, Q₄, - 2N1305

FIGURE 4 TWIN TEE 200 C/S OSCILLATOR



TWIN TEE AMPLIFIER

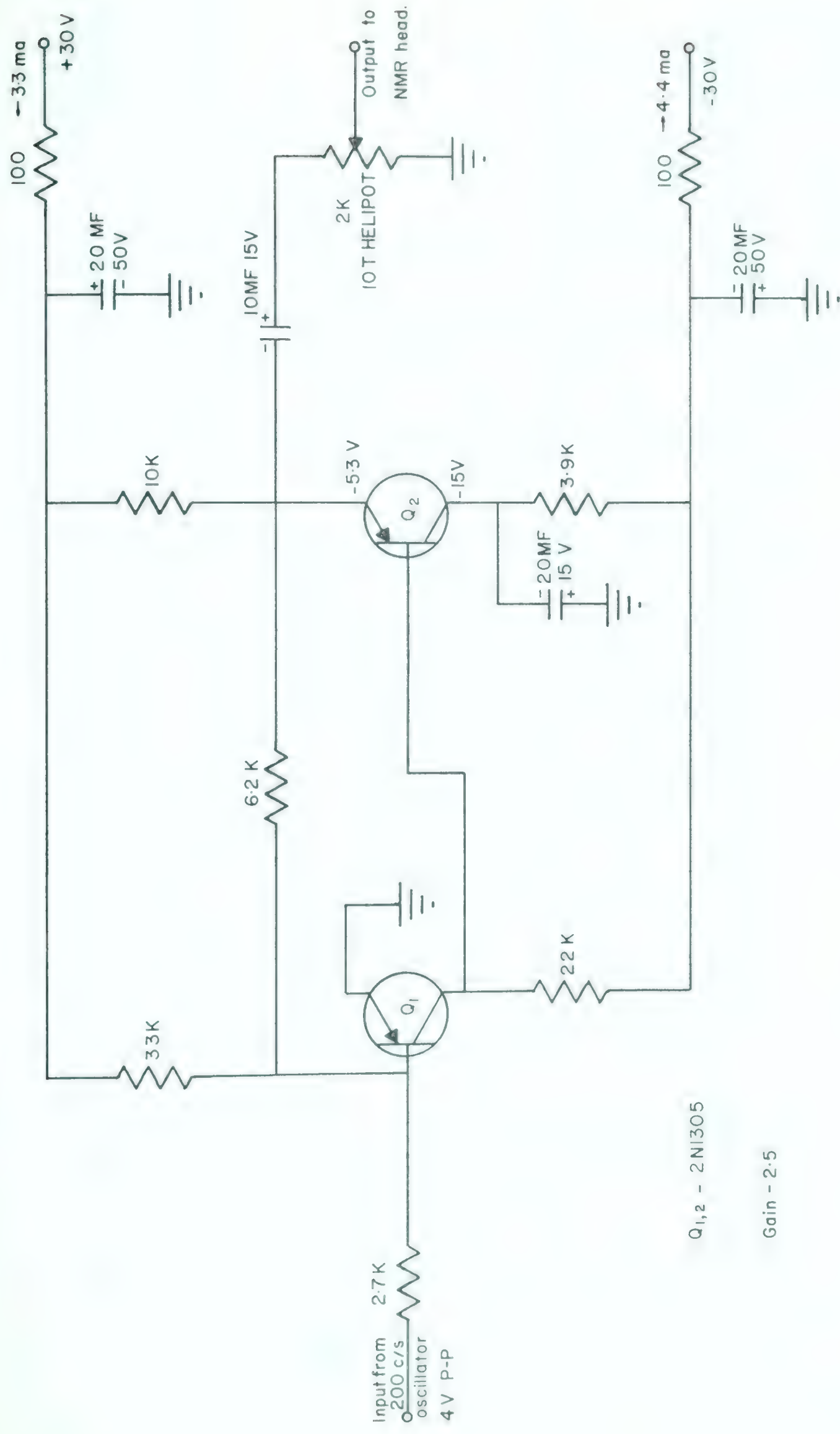


FIGURE 6 MODULATION CONTROL AMPLIFIER

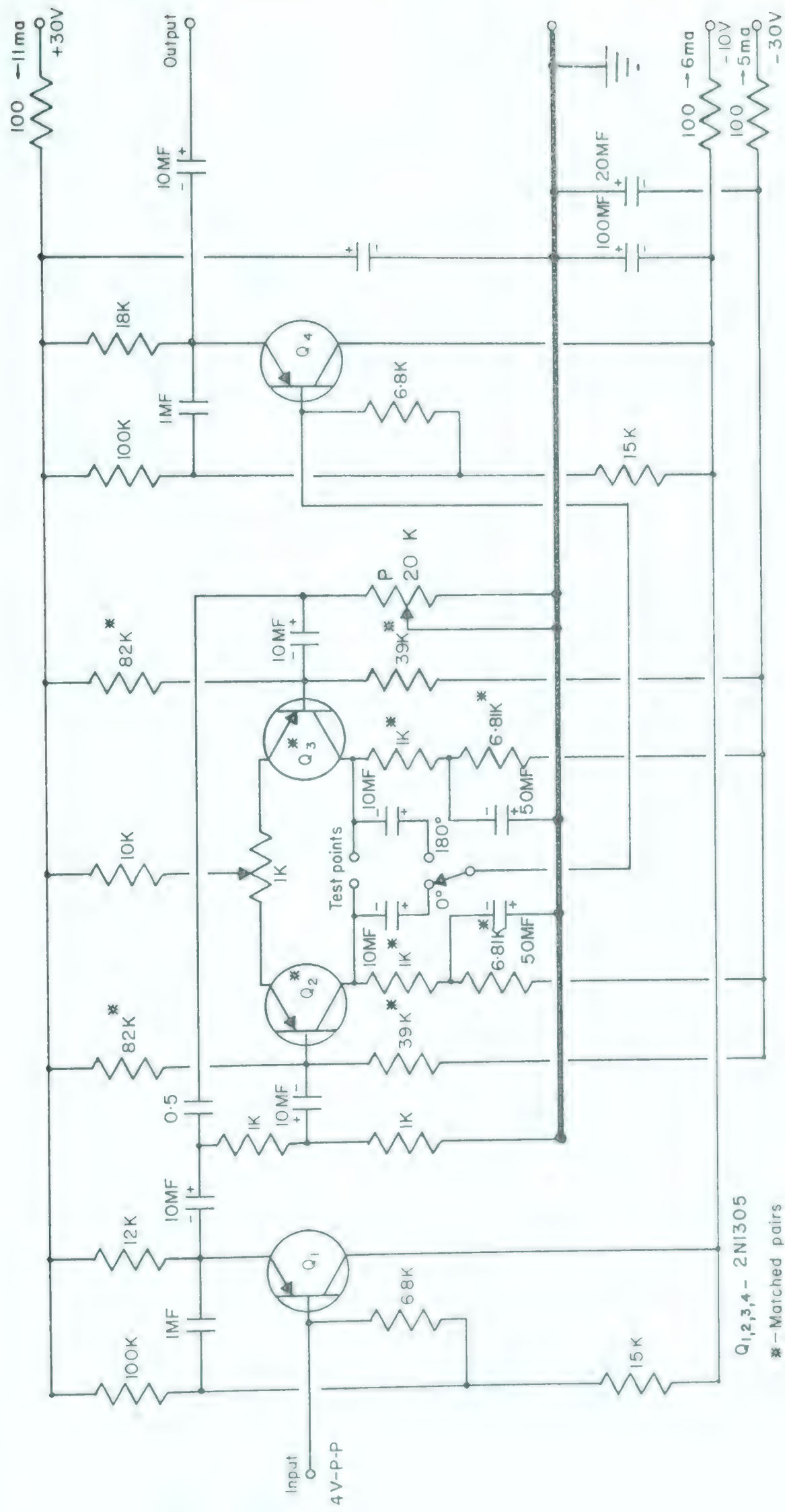
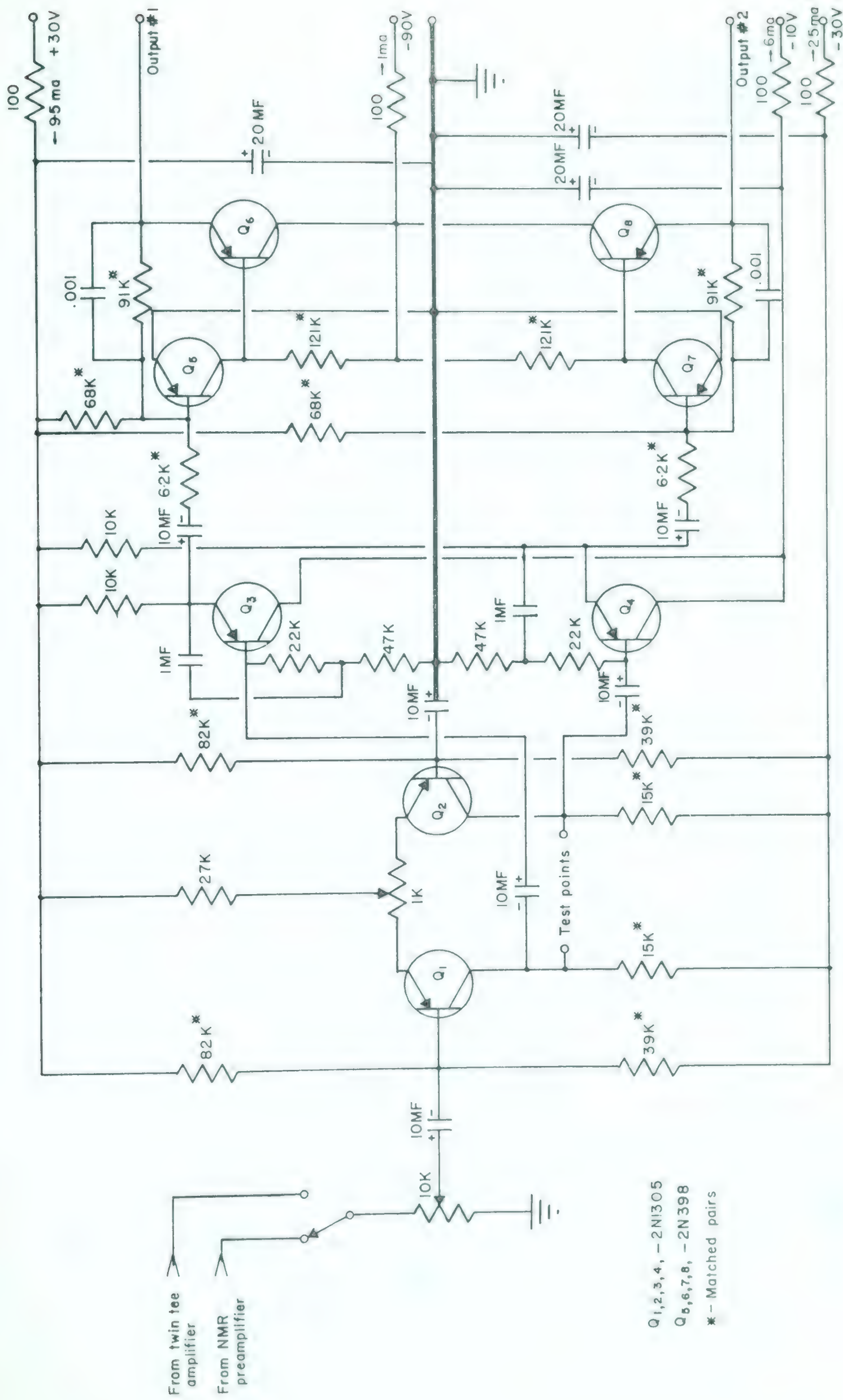
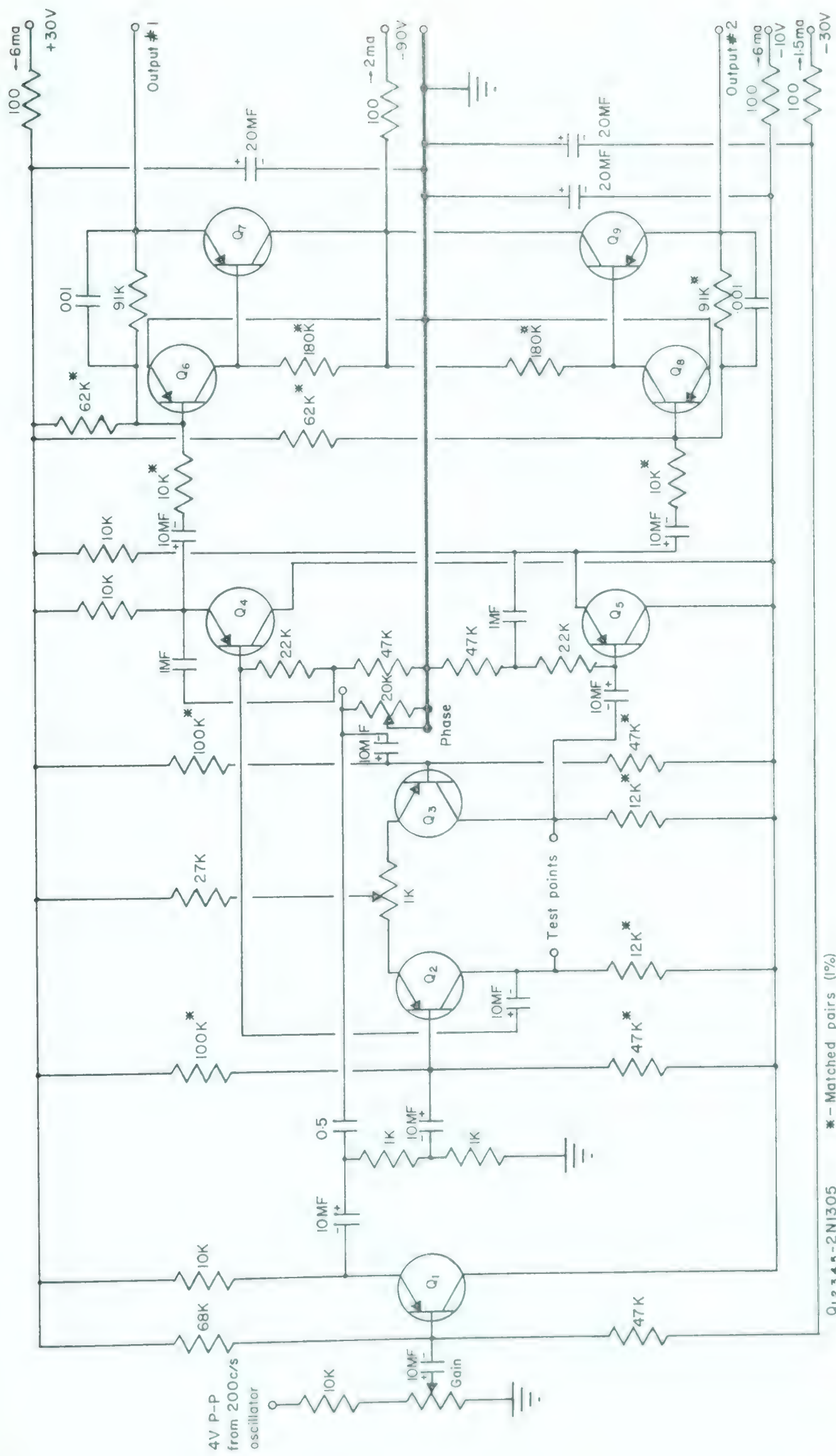


FIGURE 7 200 C/S COMPENSATING CIRCUIT



VERTICAL AMPLIFIER

FIGURE 8



HORIZONTAL AMPLIFIER

FIGURE 9

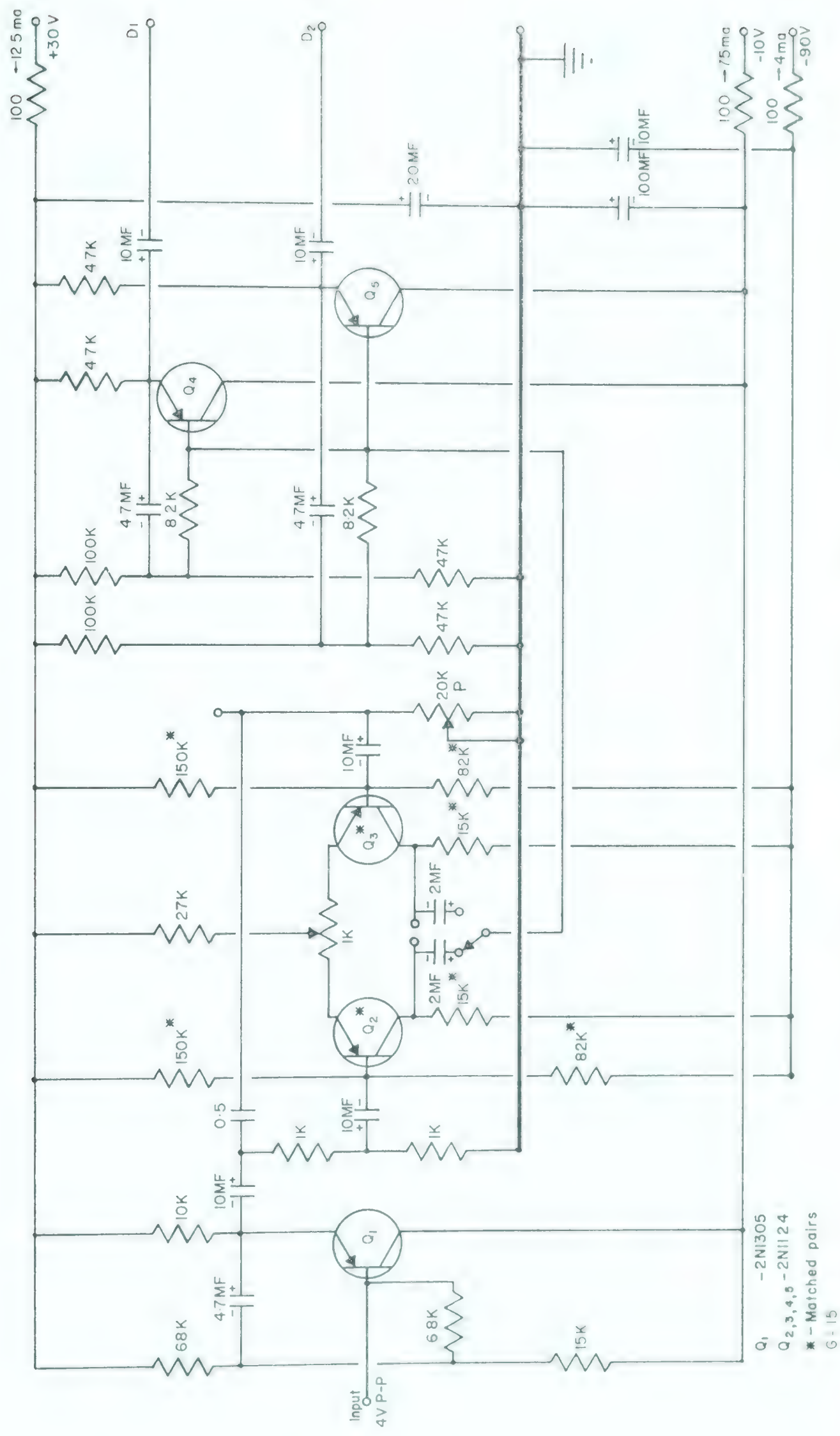


FIGURE 10 PHASE SENSITIVE DETECTOR DRIVER

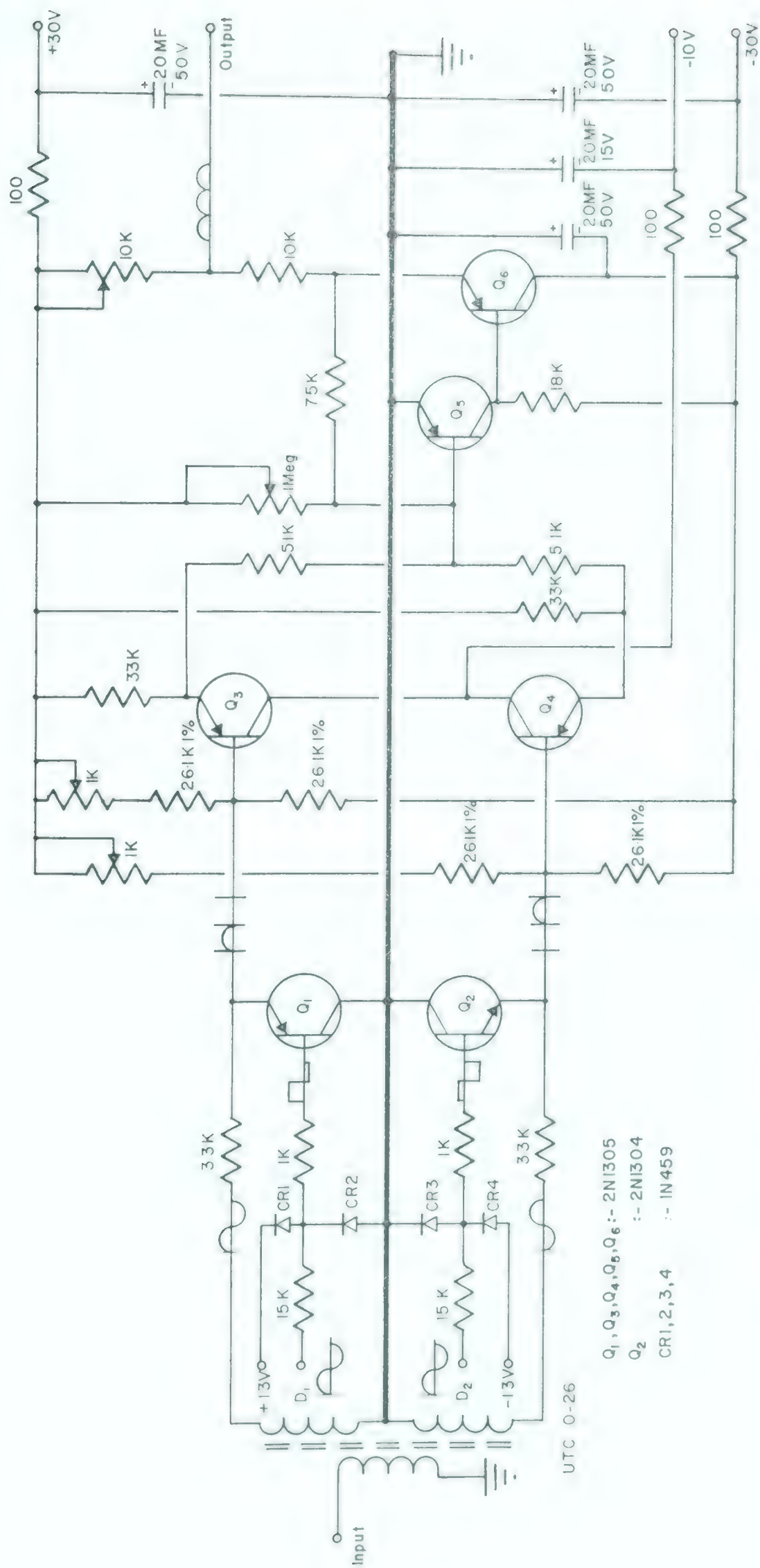


FIGURE 11

PHASE SENSITIVE DETECTOR

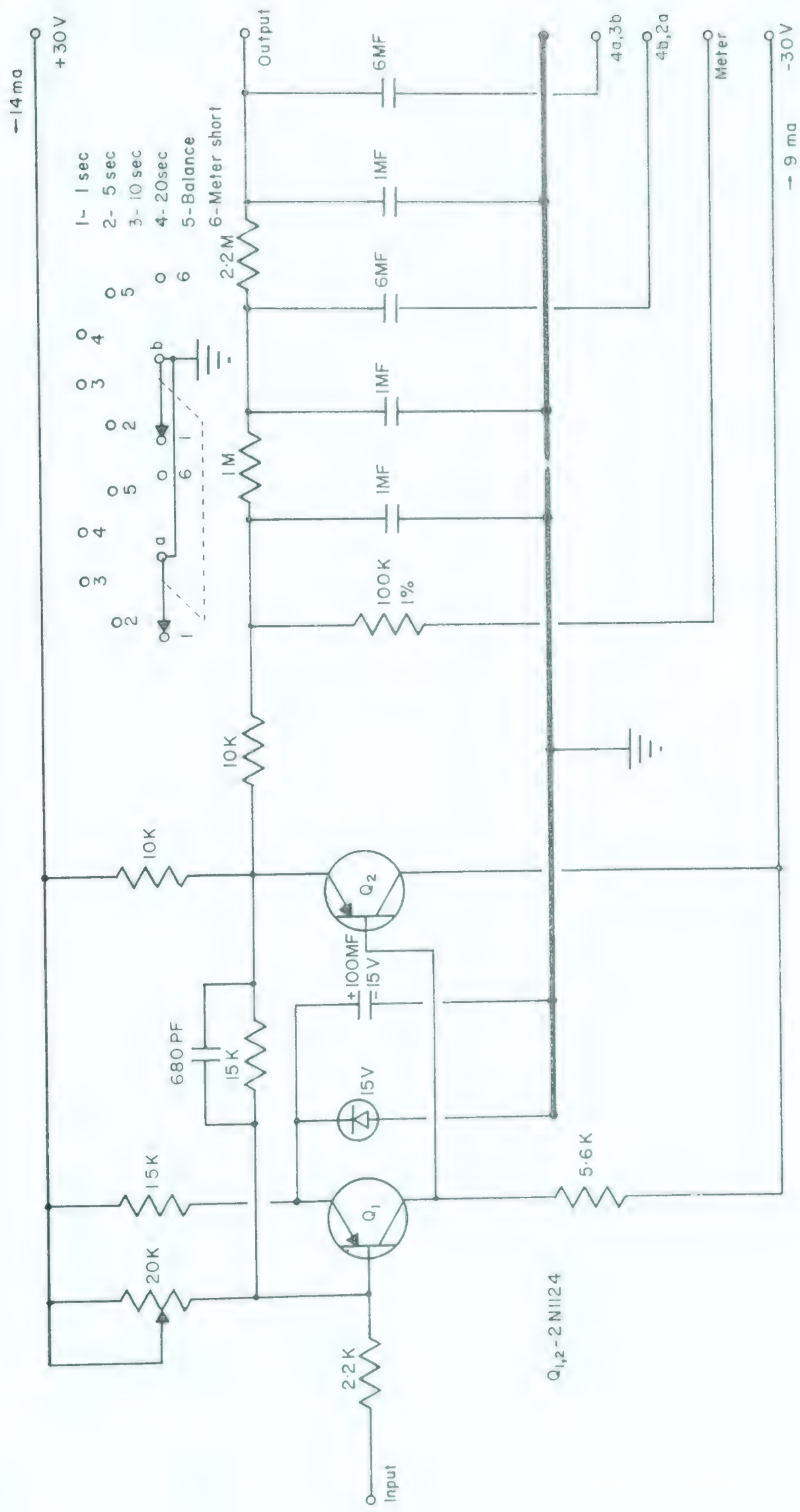


FIGURE 12

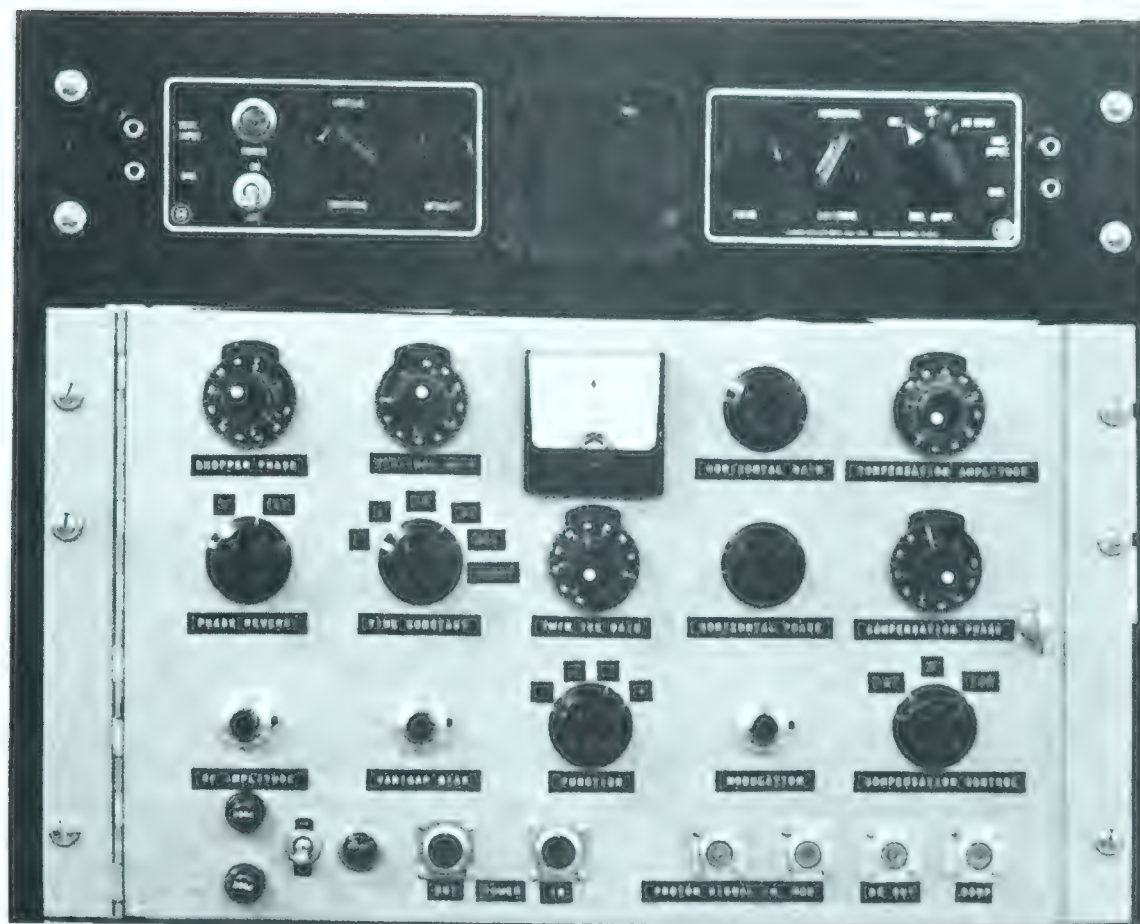
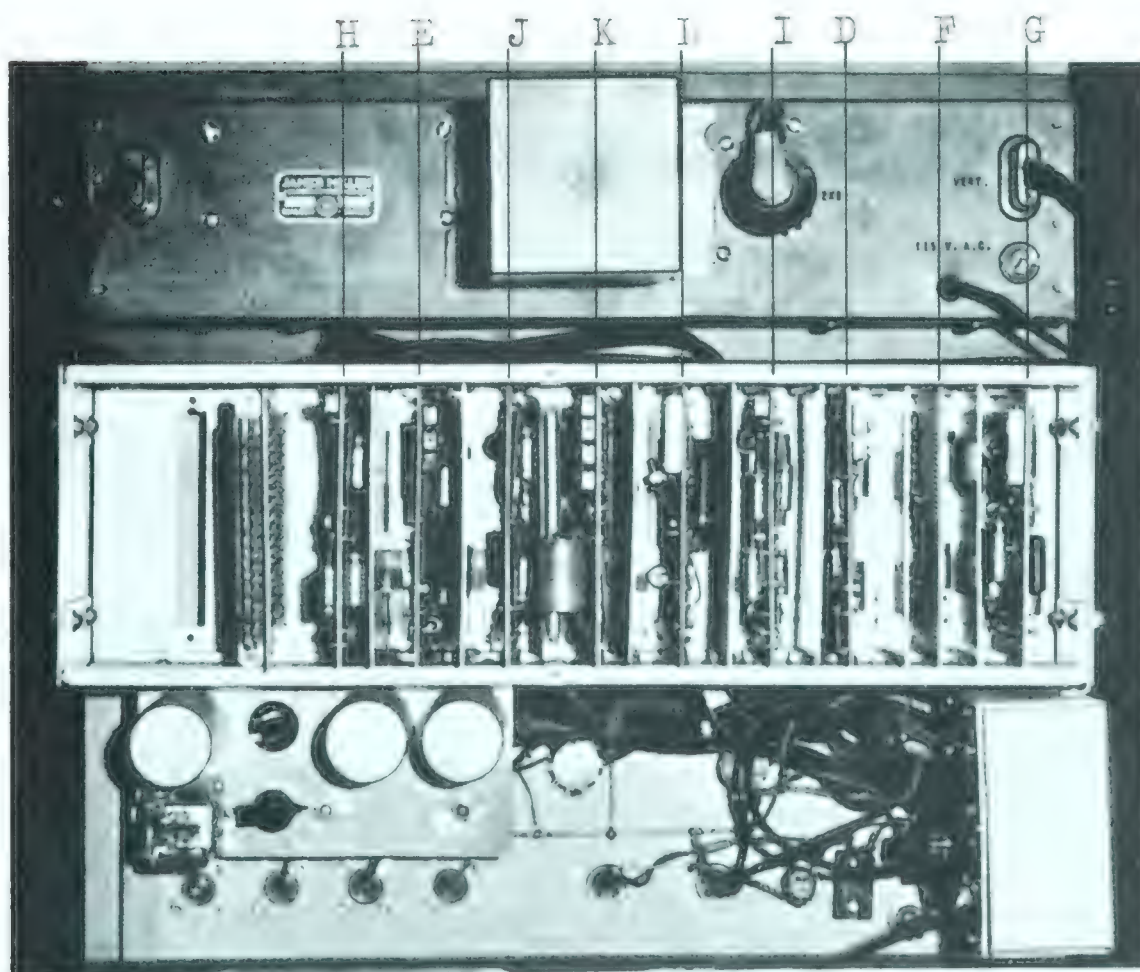


Figure 14. (a) Front view of NMR control panel



(b) Back view of NMR control system showing positions of the various circuits.

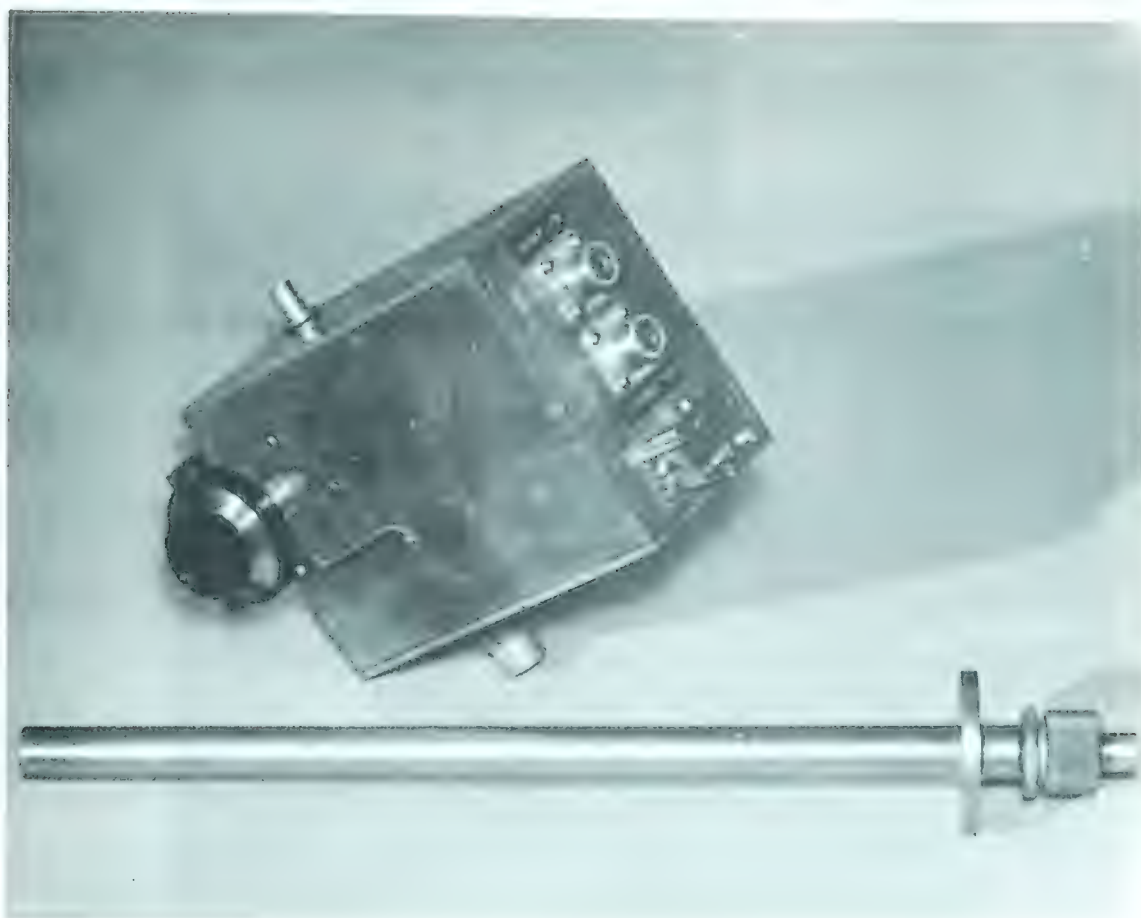
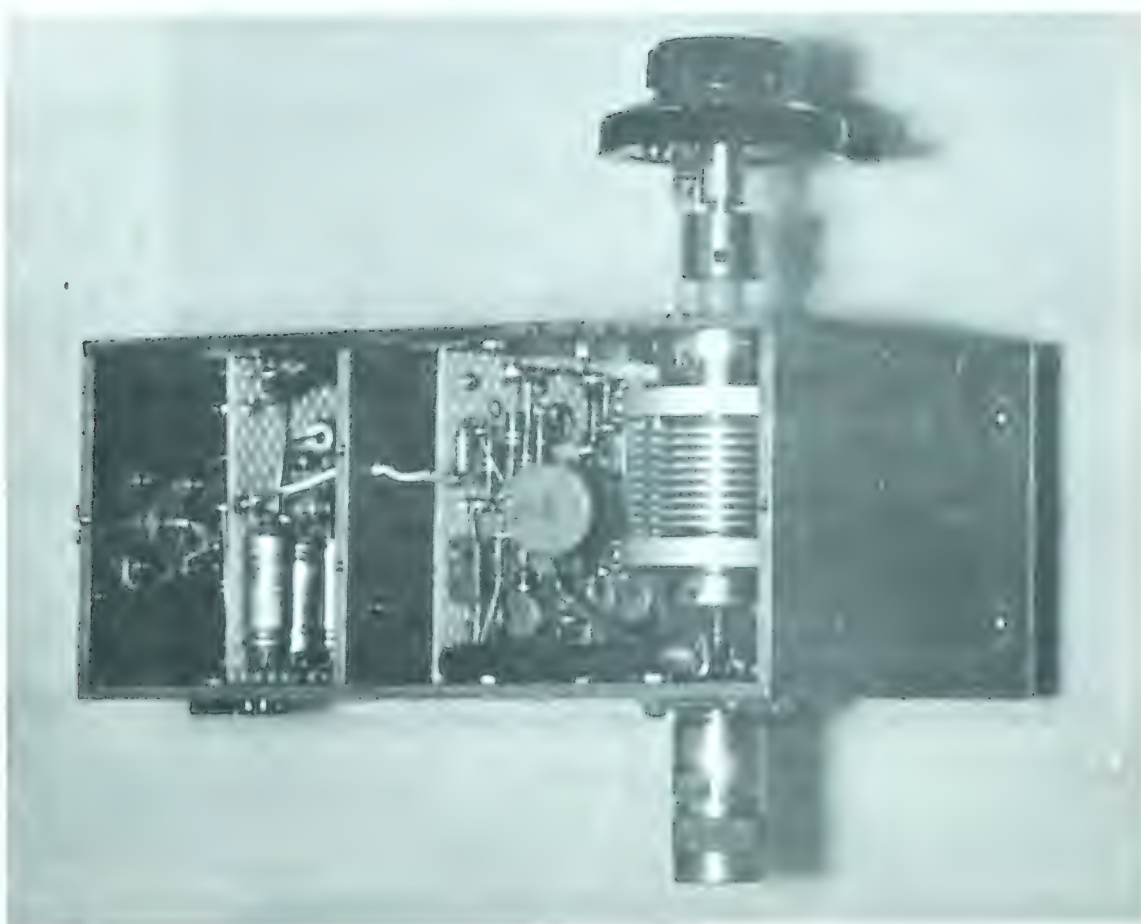
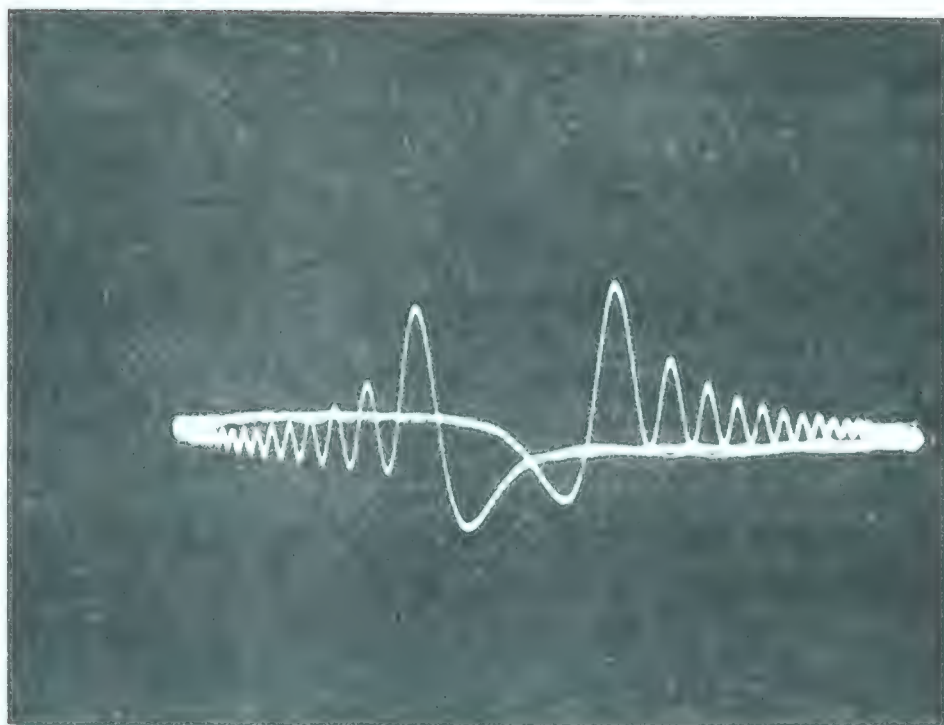


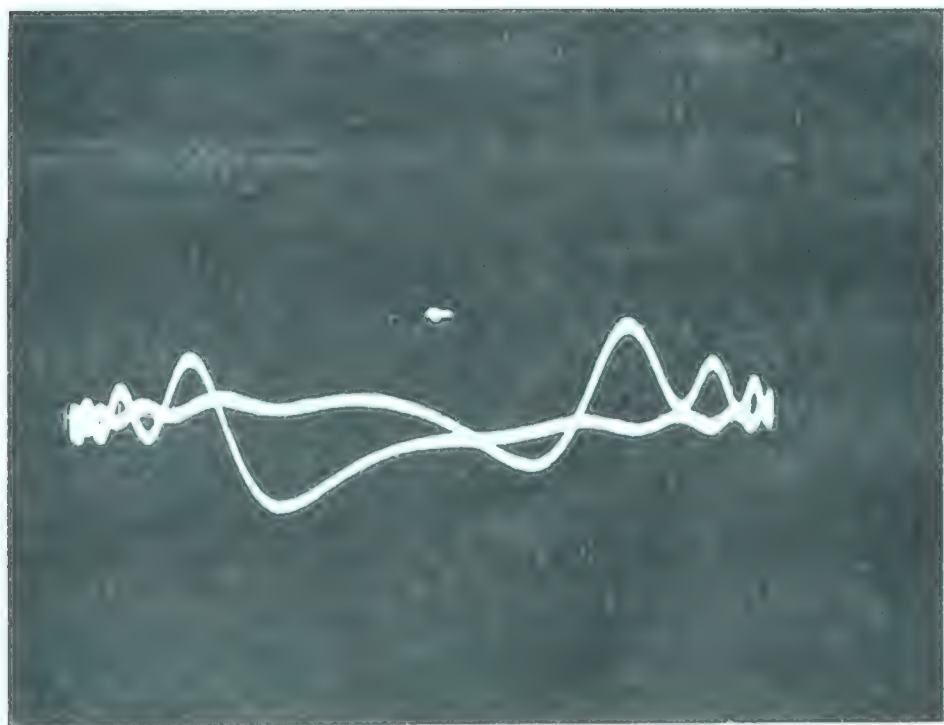
Figure 15. (a) NMR head and probe.



(b) RF oscillator and preamplifier modules in position.



(b)



(a)

Figure 16. Typical proton resonance signals obtained at one kilogauss for modulation frequencies of (a) 200 cps, (b) 30 cps.

REFERENCES

- Al 63 T.K. Alexander and G.C. Neilson, Proceedings of the Conference on Instrument Techniques in Nuclear Pulse Analysis, held at Monterey, California, April (1963), in press
- Al 63a T.K. Alexander, Private communication (1963)
- Aj 59 F. Ajzenberg-Selove and T. Lauritsen, Energy Levels of Light Nuclei, Nuclear Physics 11 (1959)
- Aj 62 F. Ajzenberg-Selove and T. Lauritsen, Energy Levels of Light Nuclei, Nuclear Data Sheets, Sets 5 and 6, USNRC (1962)
- Ba 62 J.B. Ball, A Nonrelativistic Kinematics Fortran Program to Aid Analysis of Nuclear Reaction Angular Distribution Data, ORNL-3251 (1962)
- Be 55 R.D. Bent, T.W. Bonner, J.N. McCrary, and W.A. Ranken, Phys. Rev. 100, 771 (1955)
- Be 61 E.H. Beckner, C.M. Jones, G.C. Phillips, Phys. Rev. 123, 255 (1961)
- Bo 63 V.I. Bogatin, Z. Novak, V.I. Ostroumov, Soviet Physics, JETP 16, 1116 (1963)
- Br 62 L.B. Brown and H.B. Knowles, Phys. Rev. 125, 1339 (1962)
- Br 63 J.D. Bronson, W.D. Simpson, and G.C. Phillips, Bul. Am. Phys. Soc. 8, 125 (1963)
- Ch 34 Chadwick, Feather, and Davies, Proc. Camb. Phil. Soc. 30, 357 (1934)
- Co 57 C.W. Cook, W.A. Fowler, C.C. Lauritsen and T. Lauritsen, Phys. Rev. 107, 508 (1957)
- Co 58 C.W. Cook, W.A. Fowler, C.C. Lauritsen and T. Lauritsen, Phys. Rev. 111, 567 (1958)
- Da 56 D.K. Dawson and D.L. Livesey, Can. J. Phys. 34, 241 (1956)

- De 36 P.J. Dee and C.W. Gilbert, Proc. Royal Soc. A, 154, 279 (1936)
- De 60 L.M. Delves, Nuclear Physics 20, 275 (1960)
- De 61 D. Dehnhard, D. Kamke and P. Kramer, Rutherford Jubilee Conference, Manchester (1961), Paper no. C3/19
- El 52 M. Elder and V.L. Telegdi, Helv. Phys. Acta 25, 55 (1952)
- Fr 55 G.M. Frye, Jr., L. Rosen and L. Stewart, Phys. Rev. 99, 1375 (1955)
- Ge 55 E.H. Geer, E.B. Nelson, and E.H. Wolicki, Phys. Rev. 100, 215 (1955)
- Go 50 L.K. Goward, V.L. Telegdi and J.J. Wilkins, Proc. Phys. Soc. (London) A63, 402 (1950)
- Go 53 L.K. Goward and J.J. Wilkins, Proc. Roy. Soc. (London) A217, 357 (1953)
- Go 60a F.S. Goulding, R.W. Nicholson and J.B. Waugh, Nuclear Insts. & Methods 8, 272 (1960)
- Go 60b F.S. Goulding and R.A. McNaught, Nuclear Insts. & Methods 9, 282 (1960)
- Gr 49 L.L. Green and W.M. Gibson, Proc. Phys. Soc. A62, 296 (1949)
- Ha 48 Hanni, Telegdi and Zünti, Helv. Phys. Acta 21, 203 (1948)
- Ha 55 F.J. Havlicek and B. Dobovisek, Phys. Rev. 100, no. 5 (1955)
- Ja 53 Jackson and Wanklyn, Phys. Rev. 90, 381 (1953)
- La 63 R.A. LaSalle, R.D. Bent and J.G. Cramer, Bul. Am. Phys. Soc. 8, 303 (1963)
- La 63a R.A. LaSalle, J.G. Cramer and W.W. Eidsen, Physics Letters 5, 170 (1963)
- Li 53 D.J. Livesey and C.L. Smith, Proc. Phys. Soc. (London) A66, 689 (1953)

- Ma 58 V.N. Maikov, Soviet Physics, JETP 7, 973 (1958)
- Ma 59 J.B. Marion, T.I. Arnette and H.C. Owens, Tables for the Transformation Between the Laboratory and Center-of-Mass Coordinate Systems and for the Calculation of the Energies of Reaction Products, ORNL-2574 (1959)
- Mi 53 C.H. Miller and A.G.W. Cameron, Can. J. Phys. 31, 723 (1953)
- Mi 55 Miller, Rasmussen and Sampson, Phys. Rev. 95, 649A (1954); Phys. Rev. 100, 181 (1955)
- Mu 61 Muggleton and Howe, Nuc. Insts. & Methods 13, 211 (1961)
- Ne 55 J.L. Need, Phys. Rev. 99, 1356 (1955)
- Ne 58 T.D. Newton, N-Body Nuclear Reactions, Atomic Energy of Canada Ltd., TPI-90 (1958)
- Ne 59 G.C. Neilson, W.K. Dawson and F.A. Johnson, Rev. Sci. Insts. 30, 963 (1959)
- Ne 60 G.C. Neilson, W.K. Dawson, F.A. Johnson and J.T. Sample, Suffield Technical Paper no. 176, Defence Research Board of Canada, Department of National Defence (1960)
- Ne 62 G.C. Neilson, J.T. Sample and J.B. Warren, Ch. V.Q, Fast Neutron Physics, (Ed. by J.B. Marion and J.L. Fowler) Interscience Publishers, Inc., London (1962)
- Ni 62 A. Nilsson and J. Kjellman, Nuc. Phys. 32, 177 (1962)
- Pe 51 J.L. Perkins, Phys. Rev. 81, 892 (1951)
- Ph 60 G.C. Phillips and T.A. Tombrello, Nuc. Phys. 19, 555 (1960)
- Ph 60a G.C. Phillips, T.A. Griffy and L.C. Biedenharn, Nuc. Phys. 21, 327 (1960)
- Ri 62 P.J. Riley, Ph.D. Thesis, University of Alberta (1962) unpublished
- Sa 62 J.T. Sample, W.K. Dawson and G.C. Neilson, Bul. Am. Phys. Soc. 7, 454 (1962)

- Sh 54 W. T. Sharp, J. M. Kennedy, B. J. Sears and M. G. Hoyle, Tables of Coefficients for Angular Distribution Analysis, Atomic Energy of Canada Ltd., CRT-556
- Sh 60 R. K. Sheline and K. Wildermuth, Nuc. Phys. 21, 196 (1960)
- Se 61 W. Sebaoun and H. Gauvin, J. Phys. Radium 22, 771 (1961)
- So 55 S. D. Softky, Phys. Rev. 98, 173 (1955)
- Te 50 V. L. Telegdi and W. Złnti, Helv. Phys. Acta 23, 745 (1950)
- Te 51 V. L. Telegdi, Phys. Rev. 84, 600 (1951)
- To 60a M. E. Toms, Bul. Am. Phys. Soc. 5, 346 (1960)
- To 60 T. A. Tombrello and G. C. Phillips, Nuc. Phys. 20, 648 (1960)
- To 61 W. Tobocman, Theory of Direct Nuclear Reactions, Oxford University Press (1961)
- Va 58 S. S. Vasil'ev, V. V. Komarov, and A. M. Popova, Soviet Physics, JETP 16, 521 (1963)
- Va 60 S. S. Vasil'ev, V. V. Komarov, G. V. Koshelyaev and A. M. Popova, Soviet Physics, JETP 10, 1034 (1960)
- Va 62 S. S. Vasil'ev, V. V. Komarov, and A. M. Popova, Soviet Physics, JETP 14, 1249 (1962)
- Va 63 S. S. Vasil'ev, V. V. Komarov, and A. M. Popova, Soviet Physics, JETP 16, 521 (1963)
- Wi 47 E. P. Wigner and L. Eisenbad, Phys. Rev. 72, 29 (1947)
- Wi 53 J. J. Wilkins and L. K. Goward, Proc. Phys. Soc. (London) A64, 661 (1953)
- Wi 58 K. Wildermuth and Th. Kanellopoulos, Nuc. Phys. 7, 150 (1958)
- Wi 63 D. H. Wilkinson, D. E. Alburger, A. Gallmann, and P. F. Donovan, Phys. Rev. 130, 1953 (1963)

B29820